



UNIVERSIDAD NACIONAL AUTÓNOMA DE MÉXICO
PROGRAMA DE POSGRADO EN ASTROFÍSICA

INSTITUTO DE RADIOASTRONOMÍA Y ASTROFÍSICA

**DUST DYNAMICS AND EMISSION IN PROTOPLANETARY
DISKS**

PARA OPTAR POR EL GRADO DE
DOCTOR EN CIENCIAS
(ASTROFÍSICA)

PRESENTA
ANIBAL ESTUARDO SIERRA MORALES

TUTORA
DRA. ESTELA SUSANA LIZANO SOBERÓN
INSTITUTO DE RADIOASTRONOMÍA Y ASTROFÍSICA

MORELIA, MICHOACÁN, ENERO 2020

Agradecimientos

Le estaré por siempre agradecido a cada una de las personas que me han hecho sentir como en casa durante estos 2 años de Maestría y 4 de Doctorado en México, especialmente en Morelia, en donde posiblemente he pasado los mejores años de mi vida compartiendo con mis amigos las alegrías, las frustraciones y el estrés del día a día. Sin todos ellos hubiese sido mucho más difícil lidiar con estar lejos de casa.

Agradecer a mi familia (especialmente mi mamá), los cuales pese a estar lejos físicamente, siempre me dieron ánimos para seguir adelante y apoyaron la decisión de irme de casa con el fin de cumplir mis metas. Ellos han sido, y serán siempre la mayor de las razones para seguir superándome día a día.

Mención especial también merece la Dra. Susana Lizano, quien fuese mi asesora durante la Maestría y Doctorado, y quien me guió con su experiencia y sabiduría a introducirme en el mundo de la investigación. Es imposible poder retribuir todo lo que hizo por mí en estos años, el tiempo que me dedicó y en todos los proyectos en los que me apoyó.

De entre mis amigos, agradecer especialmente a Alba Fernández, Alejandro López, Ana Merlo, Diana Jiménez, Emily García, Enrique Pérez, Jairo Alzate, Leidy González, Natalia Osorio, Rubén Guerrero y Vianey Camacho, de quienes siempre guardaré muy gratos recuerdos. Y al equipo de futbol Osos IRyA, con quienes pasé muy buenos y malos momentos, y que contra todo pronóstico ganamos el campeonato de futbol 2019-1 del campus.

Agradecer también al Instituto de Radioastronomía y Astrofísica de la UNAM por permitirme realizar mis estudios de posgrado en esta institución. A todos los profesores que compartieron su conocimiento y que siempre estuvieron abiertos a aclarar las dudas y a debatir sobre los diversos temas de la astrofísica, especialmente al Dr. Carlos Carrasco, con quien he emprendido colaboraciones científicas durante los últimos meses del doctorado. Al Programa de Apoyo a Proyectos de Investigación e Innovación Tecnológica (PAPIIT) con número de referencia a PAPIIT-UNAM IN101418, y al proyecto CONACyT 23863.

Finalmente y no menos importante, agradecer todos los héroes anónimos de Stack Overflow, quienes amable y desinteresadamente responden las preguntas de miles de usuarios sobre programación.

Contents

List of Figures	v
List of Symbols	vii
1 Protoplanetary disks	1
2 Dust opacity	11
2.1 Opacity coefficients	12
2.2 Mie Theory	20
3 Radiative Transfer	23
3.1 Emergent intensity	23
3.2 Spectral index	27
3.3 Dust settling and temperature effect	32
3.3.1 Vertical temperature	32
3.3.2 Dust settling	34
3.3.3 Spectral Energy Distribution	39
3.4 Apparent excess emission at 7 mm	39
3.5 The HL Tau disk	44
4 Gas and dust dynamics	51
4.1 Gas dynamics	52
4.2 Dust dynamics	54
4.2.1 Dust radial migration	56
4.3 Dust trapping	58
4.4 Radial dust trapping	59
4.4.1 Analytical model	60
4.4.2 Application of the model to a numerical simulation	63
4.4.3 Radial dust trapping in HD 169142	65
4.5 Azimuthal dust trapping	78
4.5.1 Gas disk model	80
4.5.2 Dust disk model	81
4.5.3 Synthetic observations	84
4.5.4 Effect of the Dust Concentration	85
4.5.5 Absorption and Scattering	88
4.5.6 Maximum grain size	88

5 Conclusions	91
A Opacity properties	95
B Gas and dust timescales	101
Bibliography	103

List of Figures

1.1	Disk mass as a function of the stellar mass	4
1.2	Radial drift and meter size barrier	7
1.3	Physical processes on protoplanetary disks	8
2.1	Scattering angle and random walk	14
2.2	Dust opacity as a function of grain size	15
2.3	Dust opacity as a function of frequency	17
2.4	Dust opacity properties	19
3.1	Radiative transport representation	25
3.2	Ratio between the emergent intensity with and without scattering	28
3.3	Spectral indices with and without scattering	30
3.4	Spectral indices slices with and without scattering	31
3.5	Vertical disk temperature structure	34
3.6	Temperature effects on the spectral indices	35
3.7	Vertical maximum grain size	37
3.8	Settling effects on the spectral indices	38
3.9	Spectral Energy Distribution as a function of the disk inclination	40
3.10	Ratio between the spectral indices with and without scattering	42
3.11	Apparent excess emission at 7 mm	43
3.12	Radial profiles of the HL Tau disk	45
3.13	Radial fits of the HL Tau disk (observed properties)	47
3.14	Radial fits of the HL Tau disk (physical properties)	48
3.15	Predicted vs observed brightness temperatures of HL Tau	49
3.16	Depth of the emission at different wavelengths	50
4.1	The radial and vertical gravitational force due to the star at a height z above the mid plane and at a radial distance ϖ	52
4.2	Drag force cartoon	55
4.3	Radial dust velocity	58
4.4	Radial dust trapping	62
4.5	Best fit model of the viscosity coefficient	64
4.6	Radial dust trapping comparison between model and simulation	65
4.7	Radial profiles of the HD 169142 disk	68
4.8	HD 169142 CO brightness temperature	69
4.9	HD 169142 disk properties	70
4.10	Maximum grain size in the HD 169142 disk	72

4.11	Best fit models of the HD 169142 disk	73
4.12	Error estimation of the best fit models	74
4.13	Maps of the best fit models of the HD 169142 disk	76
4.14	Dust properties of the best fit models of the HD 169142 disk	77
4.15	Degeneration of the particle size distribution	79
4.16	Gas disk vortex properties	80
4.17	Dust trapping within the vortex	84
4.18	Simulated ALMA and VLA images of the disk	86
4.19	Simulated ALMA and VLA images of the disk without dust concentration	87
4.20	Optical depth of the disk at several wavelengths	88
4.21	Simulated ALMA and VLA images of the disk without scattering . .	89
4.22	Dust trapping within the vortex for large grains	90
A.1	Opacity spectral indices	96
A.2	Opacity properties at $\lambda = 0.87$ mm	97
A.3	Opacity properties at $\lambda = 1.3$ mm	98
A.4	Opacity properties at $\lambda = 3.0$ mm	99
A.5	Opacity properties at $\lambda = 7.0$ mm	100
B.1	Diffusion and advection timescales	102

List of Symbols

a	dust grain radius
a_{\max}	maximum grain size
a_{\min}	minimum grain size
$a_{\max}^{\text{settling}}(z)$	limit of the maximum grain size at a height z
$a_{\max}(z)$	maximum grain size at a height z
$B_{\nu}(T)$	Planck function
c_s	sound speed
D	dust diffusion coefficient
D_g	gas diffusion coefficient
$E\%$	emission excess
\vec{F}_D	drag force
F_{ϖ}	stellar gravitational force along the axis ϖ
F_z	stellar gravitational force along the axis z
$g_{\nu}(a)$	asymmetry parameter for grains of radius a
G	gravitational constant
$h_d(a)$	dust scale height for grains of radius a
H_{ν}	second moment of the specific intensity
H_g	gas scale height
H_d	dust scale height
H_v	vortex scale length
I_{ν}	specific intensity
I_{ν}^{abs}	emergent intensity without scattering effects
I_{ν}^{ext}	extrapolated intensity at long wavelengths
I_{ν}^{sca}	emergent intensity with scattering effects
J_{ν}	first moment of the specific intensity
k_B	Boltzmann constant
K_{ν}	third moment of the specific intensity
L_*	star luminosity
m_H	proton mass
$M_{d,\text{back}}$	mass of the background dust disk
M_g	gas mass
$M_{g,\text{back}}$	mass of the background gas disk
$n(a)da$	particle size distribution
$n_2(a)$	particle size distribution after dust redistribution
$N^{13\text{CO}}$	^{13}CO column density
P	gas pressure
$P_{\nu}(\theta, a)$	scattering phase function
Q_T	Toomre parameter

R_*	star radius
RMS_λ	root mean square at wavelength λ
\mathcal{R}_ν	ratio between the emergent intensity with and without scattering
$S_\nu(T)$	source function
S_v	normalized Stokes number
St	Stokes number
$t_{\text{adv,d}}$	advection timescale of the dust grains
$t_{\text{diff,d}}$	diffusion timescale of the dust
$t_{\text{diff,g}}$	diffusion timescale of the gas
$T(z)$	vertical disk temperature
$T_{\text{acc}}(z)$	disk temperature due to accretion
T_d	dust temperature
T_{eff}	effective temperature
T_{ex}	excitation temperature
$T_{\text{irr}}(z)$	disk temperature due to the irradiation of the central star
T_*	star temperature
\vec{u}	gas velocity
\vec{v}	dust velocity
v_{th}	thermal speed
z	height above the mid plane (cylindrical coordinates)
z_1	height where the optical depth is 1
Z	coordinate along the line of sight
$\alpha_{\nu_1, \nu_2}^{\text{abs}}$	spectral index between the frequencies ν_1 and ν_2 without scattering
$\alpha_{\nu_1, \nu_2}^{\text{sca}}$	spectral index between the frequencies ν_1 and ν_2 with scattering
α_t	turbulence parameter
β_χ	extinction spectral index
β_κ	absorption spectral index
β_σ	scattering spectral index
γ_{ad}	adiabatic index
ϵ	dust-to-gas mass ratio
$\epsilon(a)$	dust-to-gas mass ratio for grains of radius a
ϵ_{global}	global dust-to-gas mass ratio
ϵ_l	local dust-to-gas mass ratio within the disk vortex
η	sub/super keplerian factor
κ_{ep}	epicyclic frequency
$\kappa_\nu(a)$	absorption coefficient for grains of radius a
κ_ν	mass weighted absorption coefficient
λ	wavelength
λ_{mfp}	mean free path of the gas
μ	cosine of the polar angle
μ_m	mean molecular weight
ν	frequency
ρ_d	dust density
$\rho_d(a)$	dust density for grains of radius a
$\rho_{d,0}$	dust density in the mid plane
ρ_m	material density

$\sigma_\nu(a)$	scattering coefficient for grains of radius a
σ_ν	mass weighted scattering coefficient
$\sigma_\nu^{\text{single}}(a)$	single scattering coefficient for grains of radius a
σ_B	Stefan-Boltzmann constant
$\Sigma_d^{\text{l.o.s}}$	dus surface density along the line of sight
Σ_g	gas surface density
$\Sigma_{\text{d,back}}(\varpi, a)$	background dust disk
$\Sigma_{\text{g,back}}(\varpi)$	background gas disk
$\Sigma_{\text{d,V}}(b, a)$	vortex dust surface density
$\Sigma_{\text{g,V}}(b)$	vortex gas surface density
τ_0^{13}	^{13}CO optical depth
$t_{\chi_\nu}^p$	optical depth coordinate along the disk axis
τ_ν	optical depth
τ_{χ_ν}	optical depth associated to the extinction coefficient
$\tau_{\chi_\nu}^p$	total optical depth along the disk axis
τ_{κ_ν}	optical depth associated to the absorption coefficient
τ_{av}	average optical depth at mm wavelengths
τ_{fric}	friction time
φ	angle between the stellar radiation and the disk surface
$\chi_\nu(a)$	extinction coefficient for grains of radius a
χ_ν	mass weighted extinction coefficient
ϖ	disk radius coordinate
$\omega_\nu(a)$	albedo for grains of radius a
$\omega_\nu(a)$	mass weighted albedo
Ω	angular velocity
Ω_d	dust angular velocity in the mid plane
Ω_g	gas angular velocity in the mid plane
Ω_K	keplerian angular velocity in the mid plane

Resumen

Hay muchos detalles aún por entender en la teoría de formación planetaria, principalmente durante las primeras etapas del crecimiento del polvo en los discos protoplanetarios. La rápida migración radial de los granos y su fragmentación, son los principales obstáculos que evitan un crecimiento efectivo del mismo. Por este motivo, el inferir las propiedades de los granos de polvo en los discos protoplanetarios (en particular, su tamaño) puede dar algunas ideas sobre cómo el proceso de formación planetaria se lleva a cabo alrededor de estrellas de baja masa como el Sol.

En este documento, se presentan resultados desde el punto de vista tanto observacional como teórico que permiten determinar las propiedades físicas del polvo, como por ejemplo: temperatura, profundidad óptica a distintas longitudes de onda, tamaño, albedo, concentración y migración.

Para ello, se utiliza la teoría del medio efectivo de Mie para determinar las propiedades de la opacidad de granos de polvo esféricos en función de su tamaño, y se realizan correcciones a los coeficientes de dispersión para poder considerar el caso de dispersión anisotrópica. Estas propiedades, además, permiten estudiar cómo se comportan el albedo, los coeficientes de absorción, dispersión y extinción para diferentes distribuciones de partículas y para distintos rangos de tamaños de granos de polvo. Entender el comportamiento de la opacidad del polvo resulta fundamental para interpretar las observaciones a través de modelos físicos.

Debido a la complejidad de considerar el proceso de dispersión de la luz en los discos protoplanetarios, muchos trabajos en la literatura han ignorado esta componente para intentar explicar las observaciones en longitudes de onda de radio. Sin embargo, algunos otros trabajos han demostrado que la dispersión es la principal fuente de opacidad en los discos. Esta tesis propone una solución analítica a la ecuación de transferencia radiativa que toma en cuenta la luz dispersada. Se comparan cuáles son las diferencias entre los parámetros físicos que se infieren de las observaciones cuando la componente de dispersión es o no despreciada y cómo cambia la intensidad emergente en ambos casos. Además, se explora cómo la dispersión puede cambiar los índices espectrales dependiendo de las propiedades del polvo en el disco, lo cual a su vez permite explicar valores de los índices espectrales por debajo del límite ópticamente grueso, los cuales han sido reportados como anómalos en la literatura.

Adicionalmente, se propone (utilizando las propiedades de la dispersión) un método alternativo a los ya conocidos para explicar el aparente exceso de emisión a $\lambda = 7$ mm reportada en varios discos alrededor de estrellas T Tauri y Herbig AeBe.

Los resultados obtenidos del modelo de transferencia radiativa son utilizados para inferir las propiedades radiales de los granos de polvo en el disco alrededor de *HL Tau* utilizando datos multifrecuencia a alta resolución de esta fuente. Los parámetros que se infieren como función del radio del disco son: el tamaño de los granos, la temperatura, la profundidad óptica, el albedo, la densidad superficial de masa y el índice espectral de las opacidades.

Debido a la importancia de relacionar las observaciones con la teoría, en la segunda parte de la tesis se estudia la dinámica del polvo en los discos protoplanetarios. Primeramente se estudia la concentración del polvo en anillos de gas axi-simétricos.

Dada la densidad superficial de gas, se propone una solución analítica a la densidad superficial de polvo tomando en cuenta la concentración diferencial de los granos de distintos tamaños. El modelo permite predecir el cociente de polvo a gas local y la distribución de tamaños de los granos como función del radio del disco. El modelo analítico es comparado con simulaciones magneto-hidrodinámicas de la evolución del polvo en discos de acreción, y posteriormente se aplica para explicar la emisión de continuo del disco alrededor de HD 169142. Mediante el ajuste simultáneo de las observaciones a longitudes de onda de $\lambda = 0.87$, 1.3, y 3 mm, se obtiene un cociente de polvo a gas global del disco y un coeficiente de viscosidad.

Posteriormente, se aborda el problema de concentración de granos de polvo en los vórtices de los discos protoplanetarios. Se extiende la solución de [Lyra & Lin \(2013\)](#) que considera la concentración de granos de polvo de un único tamaño, a la concentración de granos de polvo dada una distribución inicial. Asumiendo conservación de masa de polvo en el disco, se encuentra una solución analítica para la densidad superficial de polvo como función del tamaño del grano. Además, se calcula el cociente de polvo a gas y el cambio en la distribución de tamaño de partículas debido a la concentración de los granos dentro del vórtice. Este modelo es aplicado a una simulación numérica de un disco que contiene un vórtice. Debido a la acumulación de los granos grandes hacia el centro del vórtice, el cociente de polvo a gas aumenta por un factor de 10 con respecto al disco de fondo, mientras que la pendiente de la distribución de partículas disminuye de 3.5 a 3.0. Se encuentra además, la emisión de este disco a longitudes de onda milimétricas correspondientes a observaciones sintéticas con ALMA y el VLA. Los mapas simulados a 7 mm y 1 cm muestran una fuerte asimetría azimutal, la cual ocurre (a estas frecuencias) debido a que el disco de fondo se vuelve ópticamente delgado, mientras que el vórtice permanece en el límite ópticamente grueso.

La mayor parte de los resultados mostrados en esta tesis se encuentran basados en los siguientes artículos referenciados:

1. Dust Concentration and Emission in Protoplanetary Disks Vortices ([Sierra et al., 2017](#))
2. An analytical model of radial dust trapping in protoplanetary disks ([Sierra et al., 2019](#))
3. The Radial Distribution of Dust Particles in the HL Tau Disk from ALMA and VLA Observations ([Carrasco-González, Sierra, et al., 2019](#))
4. Effects of Scattering on the Derived Dust Properties of Observed Protoplanetary Disks and Their Apparent 7 mm Excess (Sierra & Lizano 2019, Submitted).

Además, algunos resultados han sido utilizados en las siguientes colaboraciones: Imaging a Central Ionized Component, a Narrow Ring, and the CO Snowline in the Multigapped Disk of HD 169142 ([Macías et al., 2017](#)); Cm-wavelength observations of MWC 758: resolved dust trapping in a vortex ([Casassus et al., 2019](#)); Exploring the Grain Properties in the Disk of HL Tau with an Evolutionary Model ([Tapia et al., 2019](#)).

Abstract

Planet formation theory is not yet fully understood. The fast radial migration and fragmentation are the main barriers that prevent the dust growth. Then, by inferring the dust properties in protoplanetary disks (in particular, their size), one can get ideas about the planet formation process around low mass stars.

In this thesis, observational and theoretical results are provided in order to understand the physical dust properties, for example: dust temperature, optical depth, grain size, albedo, concentration and migration. The Mie theory is used to determine the opacity properties for spherical compact dust grains as a function of their size. Corrections to the scattering coefficients are taken into account in order to consider anisotropic scattering. These properties also allow the study of the variation of the albedo, absorption, scattering, and extinction coefficients with different particle size distributions and maximum grain sizes. Understanding the dust opacity is crucial to interpret the observations with theoretical models.

Scattering is a complex process in protoplanetary disks, for this reason, it has been neglected in many previous works when analyzing observations at radio frequencies. However, some recent papers demonstrate that scattering is the main opacity source in protoplanetary disks. This thesis gives an analytical solution to the radiative transfer equation that takes into account the scattered light. It also studies the change in the emergent intensity and the physical parameters derived from observations when the scattering is taken into account or is neglected. Also, changes in the spectral indices as a function of the dust properties are explored. In the scattering case, one can obtain spectral indices below the typical optically thick value without scattering. These values have been previously reported in the literature as anomalous spectral indices.

Additionally, an alternative method to explain the apparent 7 mm excess reported in disks around T Tauri and Herbig AeBe stars is provided using the scattering properties.

The results obtained from the radiative transfer model are used to infer the radial dust properties around the *HL Tau* disk by using multifrequency high resolution data. The inferred parameters as a function of the radius are: the maximum grain size, dust temperature, optical depth, albedo, dust surface density, and opacity spectral index.

Because of the importance between theory and observations, the second part of this thesis focuses in the dust dynamics in protoplanetary disks. Firstly, dust concentration around axi-symmetric gas rings is studied. Given the gas surface density, an analytic solution for the dust surface density is given taking into account the differential grain size concentration. The model predicts the local dust-to-gas mass ratio and the particle size distribution as a function of the disk radius. The analytical model is compared with a 3D magnetohydrodynamical simulation of dust evolution in an accretion disk, and it is then applied to the disk around HD 169142. By fitting the disk continuum observations simultaneously at $\lambda = 0.87, 1.3$, and 3.0 mm, a global dust-to-gas mass ratio and a viscosity coefficient are obtained.

Then, dust concentration in disk vortices is studied. The Lyra-Lin solution for the dust concentration of a single grain size is extended to a power-law distribution

of grain sizes. Assuming dust conservation in the disk, an analytic dust surface density as a function of the grain radius is found. Also, the dust-to-gas mass ratio and the slope of the particle size distribution are computed taking into account the grain segregation within the vortex. This model is applied to a numerical simulation of a disk containing a persistent vortex. Due to the accumulation of the large grains toward the vortex center, the dust to gas mass ratio increases by a factor of 10 from the background disk value, and the slope of the particle size distribution decreases from 3.5 to 3.0. The disk emission at millimeter wavelengths corresponding to synthetic observations with ALMA and VLA are computed. The simulated maps at 7 mm and 1 cm show a strong azimuthal asymmetry. This occurs because, at these wavelengths, the disk becomes optically thin while the vortex remains optically thick.

Most of the results shown in this thesis are based on the following refereed papers:

1. Dust Concentration and Emission in Protoplanetary Disks Vortices ([Sierra et al., 2017](#)).
2. An analytical model of radial dust trapping in protoplanetary disks ([Sierra et al., 2019](#)).
3. The Radial Distribution of Dust Particles in the HL Tau Disk from ALMA and VLA Observations ([Carrasco-González, Sierra, et al., 2019](#)).
4. Effects of Scattering on the Derived Dust Properties of Observed Protoplanetary Disks and Their Apparent 7 mm Excess (Sierra & Lizano 2019, Submitted).

Also, these results have been used in the following collaborations: Imaging a Central Ionized Component, a Narrow Ring, and the CO Snowline in the Multi-gapped Disk of HD 169142 ([Macías et al., 2017](#)); Cm-wavelength observations of MWC 758: resolved dust trapping in a vortex ([Casassus et al., 2019](#)); Exploring the Grain Properties in the Disk of HL Tau with an Evolutionary Model ([Tapia et al., 2019](#)).

Chapter 1

Protoplanetary disks

The formation of protoplanetary disks is linked to the star formation process. During the gravitational collapse of the molecular cloud that forms new stars, the angular momentum conservation increases the angular velocity and forms a circumstellar disk around the protostar. This disk does not have a significant increment of its mass due to its fast mass transport onto the star. At this stage, the protostar also ejects powerful winds at high velocities.

After some million of years, the envelope is almost completely dispersed and the your star is now only surrounded by a vertically thin protoplanetary disk which rotates at almost Keplerian angular velocity around the star. The viscosity of the gas inside the protoplanetary disk is responsible of the angular momentum redistribution along the radial direction: while the mass is accreted to the star, the angular momentum is transported outwards via viscous torques. The main processes acting over the protoplanetary disk are: accretion, photo evaporation of the gas due to the irradiation of the central star (and in some cases due to an external star), the growth of the grains and gravitational interactions of the disk with massive objects (for example, planets).

Some millions of years later, when the gaseous disk has dissipated, the system consists of a pre main sequence star and a debri disk around it with very little emission of thermal radiation compared with that of the star.

All these stages were classified by [Adams et al. \(1987\)](#) (Class I, II, III) and [Andre et al. \(1993\)](#) (Class 0) based in the slope (α_{IR}) of the Spectral Energy Distribution (SED) between the near-infrared (2 μm) and the mid-infrared (10-24 μm).

This parameter classifies the evolutionary path of the Young Stellar Objects (YSOs) in four categories:

- Class 0: Most of the emission comes out in sub-millimeter wavelengths, with-

out significant emission in the infrared wavelengths because the protostar is surrounded by a massive envelope which absorbs all the infrared radiation.

- Class I: The emission at infrared wavelengths becomes important because the mass (and thus, the absorption) of the envelope has decreased. The mass of the disk is now comparable with that of the envelope and the outflows and jets are already present. The slope of the SED is: $\alpha_{\text{IR}} > 0.3$. The disk evolves viscously.
- Class II: The envelope has been accreted, the mass of the disk is around 10^{-2} of the mass of the star. The disk evolves viscously, by photo-evaporation and gravitational perturbations. The spectral index is $-1.6 < \alpha_{\text{IR}} < -0.3$.
- Class III: The disk has been dissipated and the protostar is now a pre-main sequence star. A debri disk can be present and the spectral index is $\alpha_{\text{IR}} < -1.6$.

The disk properties at Class 0 and I stars are difficult to study due to the optically thick envelope, which makes it difficult to study the internal disks properties. At these stages, the protostellar disks have large mass accretion rates that feed the protostars. Disks around Class II and III stars have a less massive envelopes that allow the observation and study of the disk properties, which are now called protoplanetary disks because they are expected to form planets.

The disks around Class II stars are composed of gas and dust. The main gas specie in the disk is molecular hydrogen H₂, but the atomic hydrogen is also present due to the dissociation of the H₂ molecules because of the radiation field. The CO molecules are also present and are fundamental to infer the gas properties, since their rotational transitions emit at radio wavelengths. Usually, the ¹³CO is used to infer the gas column density because it tends to be optically thin, while the ¹²CO is used to trace the temperature profile. They also give us information about the velocity profile via the Doppler effect (e.g. Koerner et al. 1993), from where the mass of the central star can be inferred (e.g. Dutrey et al. 1994).

The dust is mainly compose of silicates, graphite, organics, ice, carbonaceous, and polycyclic aromatic hydrocarbons (Draine, 2003). The size and composition of the dust grains are of important interest because they determine the dust opacity properties, which are then used to infer disk properties as the mass, optical depth, temperature, albedo, etc. The dust opacity properties are studied in Chapter 2 of this thesis.

One important concept in the field of protoplanetary disks is the minimum mass solar nebula (MMSN) (Weidenschilling 1977, Hayashi 1981), which determines the

minimum dust mass required to build the planets and asteroids of the Solar System. The MMSN has a gas surface density $\Sigma_g = 1700(r/\text{AU})^{-3/2} \text{ g cm}^{-2}$, while the dust (rock) surface density is $\Sigma_d = 7.1(r/\text{AU})^{-3/2} \text{ g cm}^{-2}$. The total mass of the disk within 0.35 and 36 AU is $0.013M_\odot$, which means that the ratio between the mass of the star (sun) and the disk is around 100. This value is consistent with the average disk mass around many young stars.

The disk mass is usually inferred by the optically thin dust continuum emission. In the isothermal case, the dust mass is given by

$$M_{\text{dust}} = \frac{F_\nu d^2}{\kappa_\nu B_\nu(T)}, \quad (1.1)$$

where F_ν is the observed flux, d is the distance to the source, κ_ν is the opacity coefficient and $B_\nu(T)$ is the Planck function. The disk mass (gas + dust) is $M_{\text{disk}} = 100M_{\text{dust}}$ due to the gas mass is assumed to be 100 times larger than that of the dust, as in the interstellar medium (ISM). Figure (1.1) shows the disk mass as a function of the mass of the host star (Figure credit: [Williams & Cieza \(2011\)](#)). The dash line is the region where the disk mass is 1% of that of the star, and the dashed gray area represent the region within a deviation of $\pm 1\text{dex}$ from the dashed line. As shown in this Figure, the estimations of the disk masses approximately lies within this region.

The mass derived from this method (equation 1.1) is actually a lower limit to the disk mass. The mass in very large objects (those with a size very large to the observed wavelength, e.g. meter sized objects) will not contribute to the dust continuum emission at mm-wavelengths. Also, the above equation does not take into account more complex models of the radiative transfer equation, where the inclusion of the scattering effects can increase the total opacity by one order of magnitude if the grain sizes are in the millimeter range. Then, the dust mass (and the gas mass) could be one order of magnitude larger than that expected from equation (1.1).

The radius of the disks are typically some hundred of au, but it clearly depends on the adopted definition of the disk radius. The size of the disks obtained from the continuum emission seems to be smaller than that obtained from some line emission (e.g. [Piétu et al. 2005](#), [Isella et al. 2007](#)). This disagreement could have two answers: the first one is related to the sensitivity of the radio telescopes, which cannot observe the faint dust continuum emission of the disks beyond ~ 100 au, but are capable of detecting the line emission at these radii. The second one is related to the radial migration of the dust grains within the disks, which is responsible of the depletion of the dust grains at the outer part of the disks, where the gas molecules are not

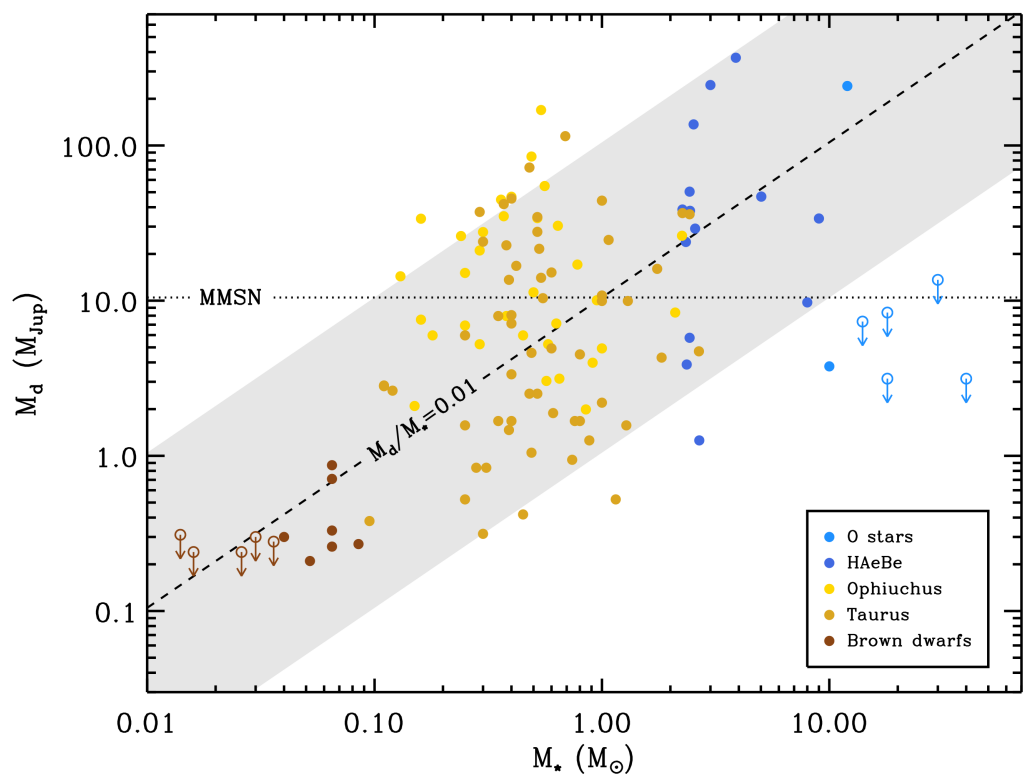


Figure 1.1: Disk mass (in Jupiter masses) as a function of the stellar mass (in Solar masses). The dashed line. Credits: [Williams & Cieza \(2011\)](#)

depleted and emit at specific lines.

In any case, the intensity of the observed disks softly decreases until it is indistinguishable from the background sky or noise. Then, the disk radius can be defined, for example, using some intensity threshold, e.g., the radius where the integrated intensity is 90% of the total one. A less arbitrary radius can be given by the fitting the disk surface density ($\Sigma(R)$) using the evolutionary disk model of [Lynden-Bell & Pringle \(1974\)](#)

$$\Sigma(R) = (2 - \gamma) \frac{M_d}{2\pi R_c^2} \left(\frac{R}{R_c} \right)^{-\gamma} \exp \left[- \left(\frac{R}{R_c} \right)^{2-\gamma} \right], \quad (1.2)$$

where γ is the power-law, M_d is the actual disk mass, R is the radial disk coordinate¹, and R_c is the radius where exponential term starts to dominate. Then, the magnitude of R_c can be used to characterize the disk radius. For example, [Pinte et al. \(2016\)](#) found that the dust surface density in the HL Tau disk can be roughly described by a disk with characteristic radius of $R_c = 80$ AU and $\gamma = -0.2$.

The vertical height of the disks is determined by the balance between the stellar gravitational force and the pressure gradient of the gas disk, the gravitational force due to the disk mass is neglected compared with that of the star. Analytical and numerical solutions of the vertical structure of the disks expected a flared disk with a gas scale height H_g increasing with the disk radius², and finally the Hubble telescope obtained an image of the jet and disk of HH 30 ([Burrows et al., 1996](#)) HH30 that confirmed the flared disk geometry.

The vertical distribution of the dust is expected to be narrower around the mid plane than that of the gas. This occurs because the dust grains, contrary to the gas molecules, can be described as a pressure-less fluid, and only the turbulent motions of the gas (which drag the dust grains) prevent a perfect settling of the dust particles in the mid plane of the disk ([Dubrulle et al., 1995](#)). It is expected than the dust grains settle around the mid plane in some thousand of years ([Armitage, 2010](#)), which is a very fast mechanism compared with the typical lifetime of the disks (some Myrs, [Wyatt \(2008\)](#)). In this thin dust layer, the dust density increases and the mean separation between dust grains decreases, favoring the collisions between the dust particles and their growth.

Dust grains also move in the radial direction. The accretion of the gas drags the

¹The radial coordinate (cylindrical coordinates) in this section is denoted as R in order to keep the notation in the references, however, in the next chapters it is used the symbol ϖ for the same variable.

²Not only the scale height is expected to increase with the radius, but also the aspect ratio H_g/R .

dust grains (specially the small particles, e.g. [Takeuchi & Lin \(2002\)](#)), but the main effect is the angular momentum interchange between both components. The gas rotates around the star at sub-Keplerian or super-Keplerian velocities depending on the local pressure gradients, while the dust grains rotates at Keplerian speeds. The collisions due to this shear produce an angular momentum interchange that move the dust grains radially inward (if the gas disk is sub-Keplerian) or outward (if the gas disk is super-Keplerian). The magnitude of the radial velocity depends on the grain size: the small grains couple to the gas and the shear velocity is very small, then there is no angular momentum interchange. The large grains have a large shear velocity but also a large inertia, then the radial velocity decreases with their mass (or size). The intermediate grains are those that have a non-negligible shear velocity and not too much inertia, so their radial velocity and migration is large.

For typical disk parameters, the dust radial velocity is high enough such that all the dust grains would be depleted from the disk in 10^4 years ([Dullemond, & Dominik, 2005](#)). This fast radial migration was a problem known as the radial drift barrier during years, however, radial and/or azimuthal pressure maxima of the disks could prevent or retard the dust accretion toward the central star.

Another famous problem in the planet formation theory is known as the “meter-size barrier”. The dust sizes in protoplanetary disks are expected to be larger than the dust found in the interstellar medium due to the high densities reached in these objects, which favor the dust growth by collisions. However, collisions do not always favor growth, if the impact velocity is large enough, the dust grains fragment or bounce. The velocity threshold where these regimes occur is an important input of the dust grain growth simulations (e.g. [Brauer et al. 2008](#), [Birnstiel et al. 2011](#)). These works found that the typical impact velocities in the disks are high enough such that the dust grains cannot grow by collisions to sizes beyond 1 meter.

A solution to this problem and the radial drift barrier was proposed by [Kataoka et al. \(2013\)](#) by changing the porosity (density) of the dust grains as they grow. He pointed out that the dust grains do not grow as constant density compact spheres but as amorphous grains, such that their global density decreases with size. Figure (1.2) shows the main processes of this mechanism. First, the dust grains grow from some μm to centimeter sizes by coagulation (black line), at this point the material density decreases around 5 orders of magnitude. Then, the dust grain grows from 1 cm to 100 m (blue line) by gas compression, which again increases the material density. Finally, the dust grows by self-gravity from 100 m to 10 km (red line), which can be now considered as a planetesimal. This path avoids the radial drift barrier (red area) where the inward infall time scale is smaller than the dust growth

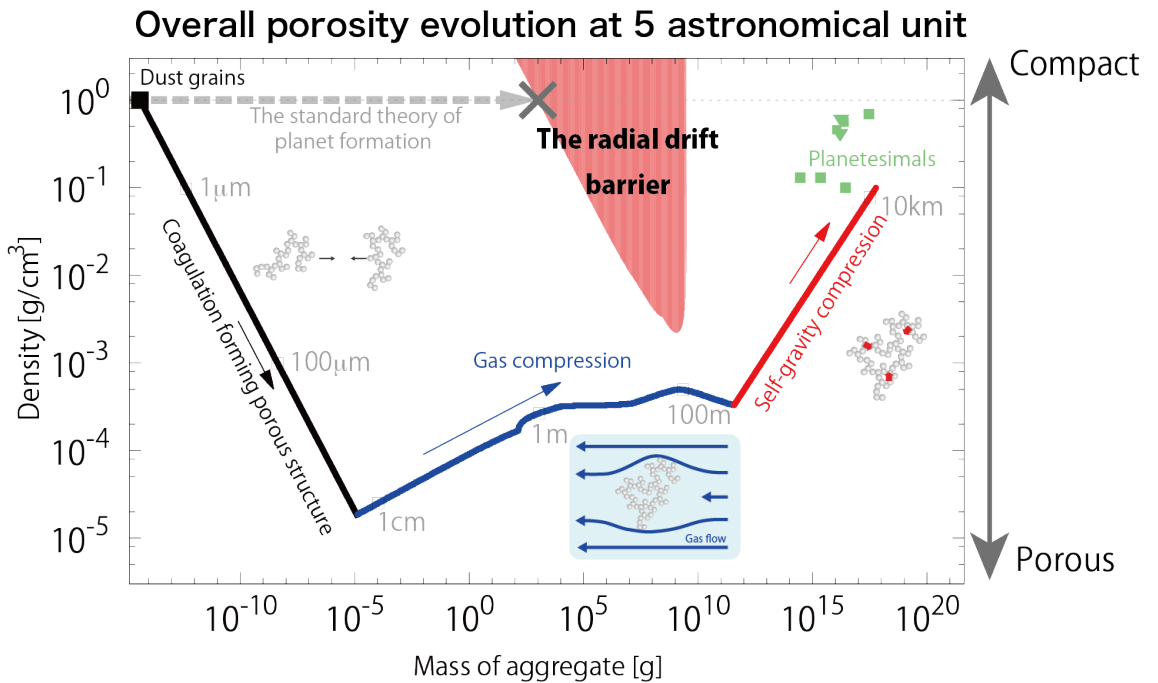


Figure 1.2: Porosity evolution proposed to avoid the radial drift and the meter size barrier. Credits: [Kataoka et al. \(2013\)](#).

time scale. Note that the constant density growth (gray dashed line) falls into the radial drift barrier.

All these processes acting on the dust grains are summarized in Figure (1.3) taken from [Testi et al. \(2014\)](#). The bottom left legend summarizes the physical processes acting on the dust grains. The length of the arrows in the image represent the magnitude of the velocity of the dust grains relative to the gas as a function of their size. The bottom right legend shows the observational data that can be obtained using different telescopes. Note that the small wavelength observations (green, yellow) can only observe the most inner part of the disk or the disk surface; however, the ALMA telescope is capable of observing the most extended region of the disk (some hundred of AU) and penetrate to regions close of the mid plane.

In the last years, with the improvement of the interferometric radio telescopes, dust asymmetries due to gaps, vortices, and spiral arms have been found in almost all the disks (DSHARP project: [Andrews et al. 2018](#)). These observations, with high angular resolution and sensitivity, have opened a new window to study the small structures in the protoplanetary disks and test the models of the dust and gas dynamics and planet formation. Surprisingly, the morphologies observed at almost all the disks are far from being smooth disks, but they have spiral arms (e.g. [Muto et al. 2012](#), [Akiyama et al. 2016](#), [Grady et al. 2013](#), [Wagner et al. 2015](#), [Mouillet et al. 2001](#)), vortices (e.g. [Isella et al. 2010](#), [Brown et al. 2009](#), [Andrews et al. 2009](#),

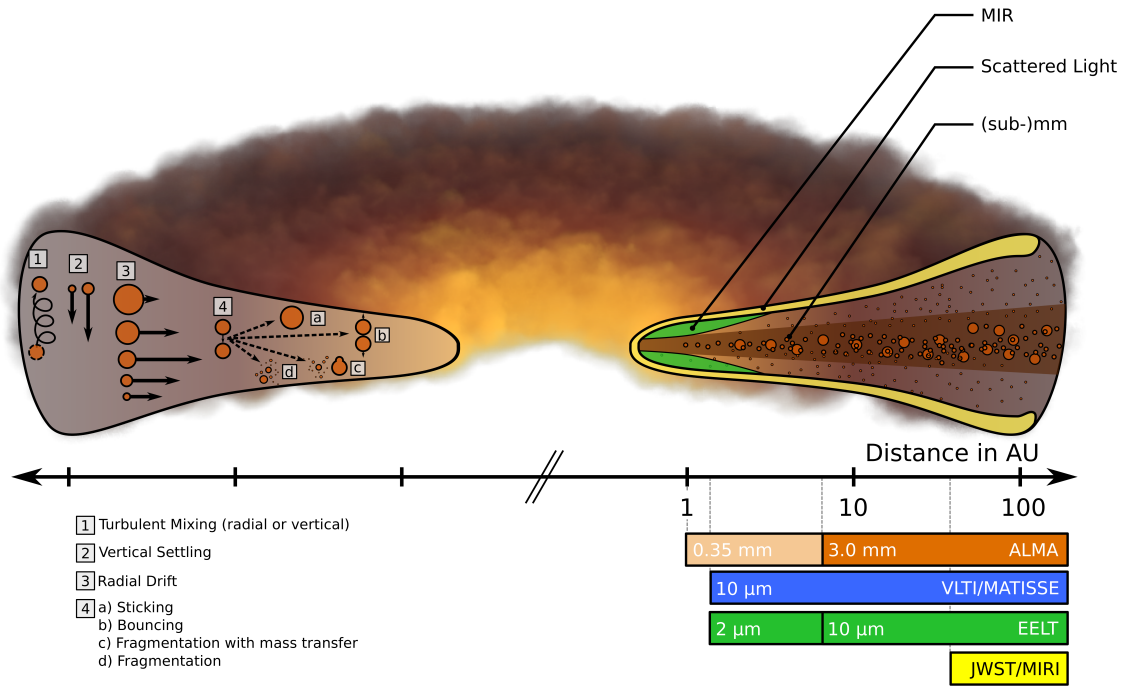


Figure 1.3: Physical processes taking place in protoplanetary disks. Credits: [Testi et al. \(2014\)](#).

[Casassus et al. 2013](#), [van der Marel et al. 2013](#)), or rings and gaps (e.g. [Andrews et al. 2016](#), [Isella et al. 2016](#), [Fedele et al. 2017](#), [Loomis et al. 2017](#), [Dipierro et al. 2018](#)). The rings and gaps seems to be present in the disks regardless of their age, and no correlation was found between the position of the rings and gaps with the age, then it seems to be a non-evolutionary effect ([van der Marel et al., 2019](#)). It is not clear yet what is the origin of these asymmetries and substructures, but there are many possibilities, which are described below.

One possible origin of the substructures in the disks is the gravitational instability of massive disks. This instability could produce disk fragmentation. In particular, [Toomre \(1964\)](#) studied the rotation of gaseous accretion disks, where the disk pressure and the gravitational force try to expand and collapse a disk parcel, respectively. He found that disks with a surface density Σ larger than $\pi G / (c_s \kappa_{\text{ep}})$ are gravitationally unstable, where κ_{ep} is the epicyclic frequency. The Toomre criterium for stable disks is written as

$$Q_T = \frac{c_s \kappa_{\text{ep}}}{\pi G \Sigma} > 1. \quad (1.3)$$

Another possible origin of the gaps and rings is the magneto-rotational instability (MRI) ([Balbus, & Hawley, 1991](#)) close to the dead zone, where a transition between the high and low-ionization zones rises the accretion stresses ([Varnière, & Tagger, 2006](#)). [Flock et al. \(2015\)](#) studied this problem and found that the disk becomes

turbulent, generating a large gap and an increase of the surface density close to the dead zone. A vortex is then generated by the Rossy wave instability, which could act as a trap of large dust grains (e.g. [Barge & Sommeria 1995](#)). In these vortices, the dust-to-gas mass ratio can reach values of unity ([Surville et al., 2016](#)). If the gas vortex is rapidly destroyed, the trapped dust is redistributed in a concentric ring that can have dust material with masses similar to that of Earth. On the other hand, if the gas vortex is long-lived, the trapped dust remains after gas dissipation, and could become gravitationally unstable ([Surville et al., 2016](#)).

The main source of instability of the MRI is the coupling of ionized gas with the magnetic field, which causes attractive forces between consecutive layers of the rotating disk and destabilize it. The requisites for a magnetized disk to be linearly unstable ([Balbus, & Hawley, 1991](#)) is that the degree of ionization be larger than 10^{-12} (neutral gas is not affected by the magnetic field), the magnetic pressure be larger than the gas pressure, and the square of the orbital velocity decreases with radius

$$\frac{d\Omega^2}{dR} < 0, \quad (1.4)$$

which is satisfied by Keplerian disks.

The presence of planets can also generate rings and gaps (which carve the disk material at their orbiting radius) (e.g. [Dipierro, & Laibe 2017](#)) or induce spiral arms (e.g. [Bae, & Zhu 2018](#)). However, in these models, it is not clear what is the origin of the planet, they are only introduced to explain the ring structures.

In all these models, the asymmetries generates pressure bumps that prevent the dust radial migration. Moreover, they can promote the planet formation via the gravitational instability if the dust mass capture is large enough and satisfies the Toomre criterium (equation 1.3).

An alternative explanation to the rings observed in many disk was proposed by [Ros, & Johansen \(2013\)](#), where the large grains accumulate close to the snow lines due to the freeze out or sublimation of gas volatiles on the surface of dust grains that significantly change their sticking properties ([Güttler et al., 2010](#)). Recently, evidence of the position of the gaps/rings with the ice lines has been found around the HL Tau disk (e.g [Zhang et al. 2015](#), [Carrasco-González, Sierra, et al. 2019](#)). The changes in the sticking properties was also used by [Okuzumi et al. \(2016\)](#) to propose a method to explain the multiple ring structure based on the aggregate sintering. This mechanism, which pile ups dust grains slightly outside the snow lines of the volatiles, is used in addition to the coagulation, fragmentation, and radial drift of the dust grains in order to explain the rings observed in the HL Tau disk.

Whatever the case about the origin of the asymmetries, infer the properties of the dust grains is fundamental to understand which physical mechanisms are relevant in the disks. For this reason, in this thesis we first study in Chapter 2 how the dust opacity at different wavelengths depends on the dust properties, in particular: on the grain size. These properties, in addition to the radiative transfer equation (Chapter 3), allow to create synthetic maps of the dust continuum emission at mm wavelengths given some disk model and taking into account the scattered light. The latter has been neglected in previous works, and in this thesis we propose a simple analytic equation to explain their effects on the emergent intensity. An application of this solution is presented at the end of the Chapter 3 to explain the multi-wavelength dust emission of the disk around HL Tau. Finally, in Chapter 4, the gas and dust dynamics are studied and analytical solutions to the radial dust trapping in rings and vortices are given.

Chapter 2

Dust opacity

The main source of opacity in protoplanetary disks is dust. These particles, which are expected to have sizes from $0.05 \mu\text{m}$ to some millimeter or centimeter, are the responsible of absorbing and emitting radiation at almost all the disk spectrum. During decades, the opacity properties have been studied in order to understand and infer the dust properties from the observations, in particular, the maximum grain size. For example, many studies have explored the effect of the dust abundances (Pollack et al. 1994), the particle size distribution (e.g. Mathis et al. 1977; Miyake & Nakagawa 1993; Draine 2006), polarization (Kataoka et al., 2015), porosity and fluffiness (e.g. Kataoka et al. 2014).

The importance of the dust grain size is fundamental for the planet formation theory, where the dust grains are expected to grow, migrate, and concentrate during the first stages of the disk lifetime (Brauer et al., 2008). Millimeter and centimeter dust grains have been inferred based on the spectral index of sub-millimeter and millimeter dust continuum observations (e.g. Pérez et al. 2015; Carrasco-González, Sierra, et al. 2019). However, dust grains with sizes of only some hundred micrometers have been inferred from millimeter polarization observations (Kataoka et al., 2015). It is not clear at the date what causes the disagreement between both methods. One possible solution can be the following: If polarization observations are optically thick (this is probably true at the small wavelengths where the polarization pattern has been observed), they could be tracing the disk atmosphere, where only small dust grains are expected due to dust settling (Dubrulle et al., 1995). However, the disk observations at long wavelengths (e.g. those with VLA) could reach the disk midplane, and trace large grains. Thus, both methods may disagree because they are tracing different disk layers. This thesis does not deal with the disagreement between the polarization and spectral index disagreement, it only focuses on the expected observation properties based on the spectral index.

Recently, [Yang, & Li \(2019\)](#) found that both the polarization pattern and the small spectral index can be simultaneously explained by a population of dust grains with a maximum grain size of 3 mm and with a dust composition that is a pure absorptive carbonaceous. This work shows that the typical dust compositions that include organics cannot reproduce small spectral indices and the polarization pattern simultaneously, however, if the organics are not included in the dust chemical composition, the small spectral index and the polarization pattern agree. This occurs because the refractive index of the dust organics grains has a small imaginary part (the larger the imaginary part, the larger the absorptive dust model) compared with other grains (e.g. graphites, troilite, Figure 4 of [Yang, & Li \(2019\)](#)). Then, organics could be the main responsible of the disagreement of the inferred maximum grain size between the spectral index and polarization method. Thus, the dust composition could play an important role when interpreting and inferring properties from observations.

2.1 Opacity coefficients

The dust opacity has two contributions: absorption and scattering. The latter have been neglected in many works because it is more complex and time consuming in Monte Carlo simulations; however, when the dust grains grow to sizes similar to the observed wavelength, the scattering has been proved to be the main opacity source ([Miyake & Nakagawa, 1993](#)). The parameter that describes the scattering regime is given by $x = 2\pi a/\lambda$, where λ is the observed wavelength and a is the size of the dust grain. The scattering process has two limits: the Rayleigh scattering regime $x \ll 1$, and the geometric scattering regime $x \gg 1$. Nevertheless, in protoplanetary disks, where the dust grains are expected to grow to sizes $a \sim 1$ mm, $x \sim 1$ at sub-millimeter and millimeter wavelengths. In this regime, the scattering is described by the Mie theory, and the emergent intensity in protoplanetary disks can be dominated by the scattered light from millimeter and/or centimeter dust grains.

In addition, the scattering can be divided in three types: elastic scattering, inelastic scattering, and quasi-elastic scattering. The difference between them is the wavelength of the scattered photon compared with the incident photon. In the first one, the wavelength remains the same (the photon is only redirected); in the second one, the wavelength of the scattered photon changes (e.g. fluorescence); and in the third one, only the phase of the photon is shifted, but the wavelength remains unchanged (e.g. by Doppler effect). During all this work, elastic scattering is assumed.

The extinction coefficient $\chi_\nu(a)$ (cm^2/g in cgs units) for grains with radius a at the frequency ν is the sum of the absorption coefficient $\kappa_\nu(a)$, and the scattering coefficient $\sigma_\nu(a)$,

$$\chi_\nu(a) = \kappa_\nu(a) + \sigma_\nu(a), \quad (2.1)$$

while the albedo $\omega_\nu(a)$ is defined as the ratio between the scattering coefficient and the extinction coefficient

$$\omega_\nu(a) = \frac{\sigma_\nu(a)}{\chi_\nu(a)}. \quad (2.2)$$

The scattering coefficient $\sigma_\nu(a)$ in these equations is the effective scattering coefficient, which is defined as

$$\sigma_\nu(a) = (1 - g_\nu(a))\sigma_\nu^{\text{single}}(a), \quad (2.3)$$

where $\sigma_\nu^{\text{single}}(a)$ is the single scattering coefficient and $g_\nu(a)$ is the asymmetry parameter defined as the expectation value of the cosine of the scattering angle given by

$$g_\nu(a) = \int_{4\pi} \cos(\theta) P_\nu(\theta, a) \frac{d\Omega}{4\pi} \quad (2.4)$$

where θ is the scattered angle defined in the left image of Figure (2.1), $d\Omega$ is an element of solid angle, and $P_\nu(\theta, a)$ is the scattering phase function that gives the angular distribution of photons with wavelength λ scattered by a dust grain with size a .

The correction $g_\nu(a)$ is included to take into account the non-isotropic scattering (Henyey, & Greenstein, 1941). For example, if a photon is scattered in the forward direction, then the problem is equivalent to a non-scattering medium (the photon is not redirected and its wavelength is the same). If the photons are preferentially forward scattered, the value of $g_\nu(a)$ tends to 1 because the scattering process can be equivalently described as a less effective scattering medium. Thus, $\sigma_\nu(a)$ decreases according to equation (2.3). For pure isotropic scattering $g_\nu(a) = 0$. The value of $\sigma_\nu^{\text{single}}(a)$ is relevant for random walk Monte Carlo simulations, where the angle probability distribution is taken into account and a scatter angle is randomly chosen given some angular distribution probability. Figure (2.1) shows a cartoon of the single angle scattering process. In a 3D simulation, an azimuthal angle should also be randomly chosen in addition to the polar angle θ . The azimuthal angle is not relevant and is usually assumed to be equiprobable between 0 and 2π . The right image follows the path of 10 representative photons in a disk assuming isotropic scattering. In this method, the position of the last scattering can be saved in order

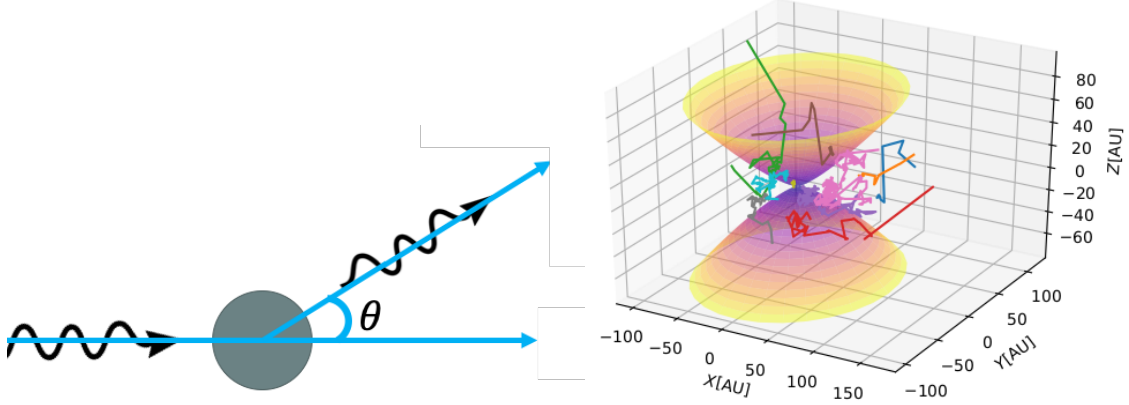


Figure 2.1: Left: Single scattered angle. Right: Monte Carlo random walk simulation of the scattering.

to compute an image of the scattered light of the disk.

The coefficients $\kappa_\nu(a)$, $\sigma_\nu^{\text{single}}(a)$, and $g_\nu(a)$ depend on the grain size and the observed frequency and can be written in terms of the dust dielectric constants (equations 2.55-2.57 of Kruegel 2003). In this work, the coefficients are computed using the Mie theory for spherical dust grains of a given composition. We adopt the Pollack et al. (1994) dust abundances (26% silicates, 31% organics, 43% ice) and use the D'Alessio et al. (2001) code to compute these coefficients as a function of the grain radius. These coefficients are in units of cm^2 per gram of dust. To obtain the coefficients in terms of the gas mass, they should be multiplied by the dust-to-gas mass ratio.

Figure (2.2) shows the dust opacity coefficients, the asymmetry parameter, and albedo as a function of the grain size at four different millimeter wavelengths: $\lambda = 0.87 \text{ mm}$ (blue), 1.3 mm (yellow), 3.0 mm (green), and 7.0 mm (red). The grain size where the scattering coefficient is maximum increases with the wavelength. For these curves the maxima lie at $a \sim \lambda/2\pi$. In the interstellar medium (ISM) the dust grains follow a particle size distribution (Mathis et al., 1977) $n(a)da \propto a^{-p}da$, which gives the number density of dust grains with radius between a and $a + da$. The ISM is characterized by a slope $p = 3.5$, which is also typically assumed in protoplanetary disks. However, if the coagulation process is dominant and dust growth occurs, a smaller value for the slope is expected (Miyake & Nakagawa, 1993).

The mass weighted monochromatic coefficients (Figure 2.2) are integrated be-

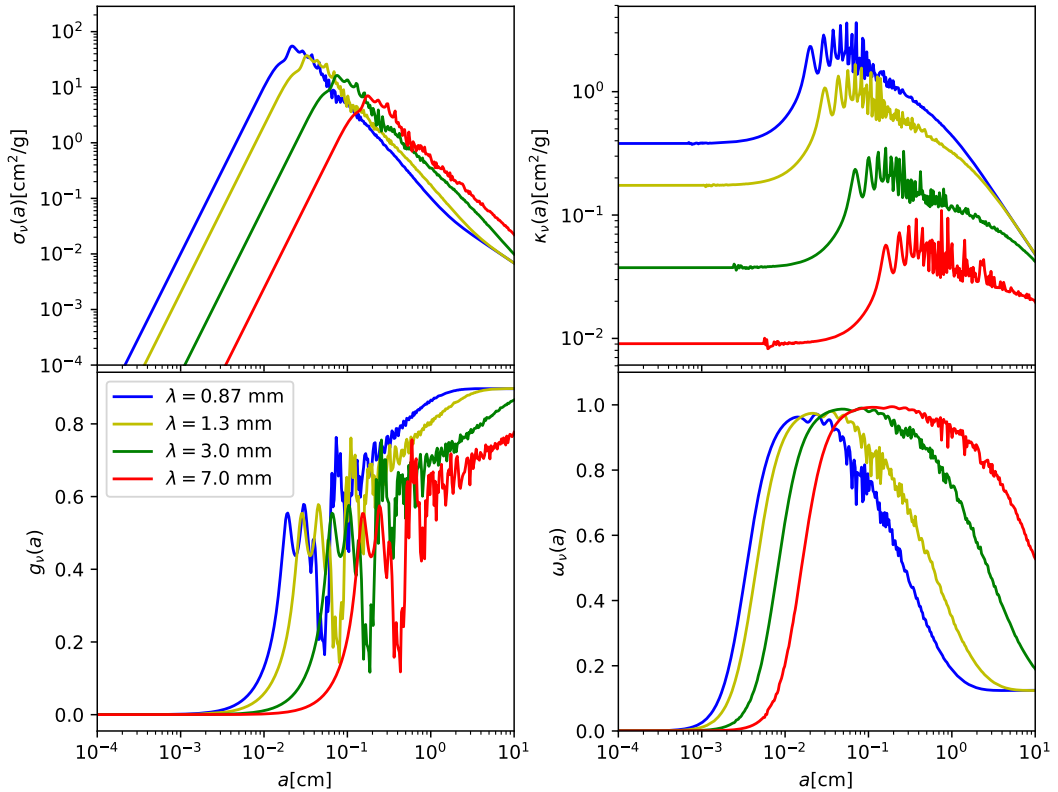


Figure 2.2: Dust opacity properties as a function of grain size. Top left: scattering coefficient; top right: absorption coefficient; bottom left: asymmetry parameter; bottom right: albedo. The blue, yellow, green and red lines represent the properties at a wavelength $\lambda = 0.87, 1.3, 3.0$ and 7.0 mm respectively.

tween the minimum grain size a_{\min} and the maximum grain size a_{\max} as

$$\kappa_\nu = \frac{\int_{a_{\min}}^{a_{\max}} \kappa_\nu(a) a^3 n(a) da}{\int_{a_{\min}}^{a_{\max}} a^3 n(a) da}, \quad (2.5)$$

$$\sigma_\nu = \frac{\int_{a_{\min}}^{a_{\max}} \sigma_\nu(a) a^3 n(a) da}{\int_{a_{\min}}^{a_{\max}} a^3 n(a) da}, \quad (2.6)$$

$$\chi_\nu = \frac{\int_{a_{\min}}^{a_{\max}} (\kappa_\nu(a) + \sigma_\nu(a)) a^3 n(a) da}{\int_{a_{\min}}^{a_{\max}} a^3 n(a) da} = \kappa_\nu + \sigma_\nu. \quad (2.7)$$

These three coefficients are also called opacity coefficients, because they absorb and/or scatter the radiation from the line of sight. The albedo is then defined as

$$\omega_\nu = \frac{\sigma_\nu}{\chi_\nu}. \quad (2.8)$$

Figure (2.3) shows the absorption (top left panel), scattering (top right panel), extinction (bottom left panel), and the albedo (bottom right panel) as a function of the frequency for different maximum grain sizes (indicated at the bottom right corner of the top right panel). The gray area are the radio frequencies where several protoplanetary disks have been observed during the last years, from $\lambda = 870 \mu\text{m}$ (ALMA band 7) to 7 mm (VLA band Ka). In all the cases, the slope of the particle size distribution is set to $p = 3.5$ and the minimum grain size is set to $a_{\min} = 0.05 \mu\text{m}$. The latter value does not affect the opacity properties when $a_{\max} \gg a_{\min}$ (Draine, 2006). The dependence of the coefficients as a function of a_{\max} and p is explored in Appendix A.

During the rest of this chapter, we focus in the dust properties at millimeter wavelengths, specifically between $\lambda = 0.87$ and 7 mm, where the absorption, scattering, and extinction coefficients can be fitted by a power law of the frequency as

$$\kappa_\nu = \kappa_0 \left(\frac{\nu}{\nu_0} \right)^{\beta_\kappa}, \quad (2.9)$$

$$\sigma_\nu = \sigma_0 \left(\frac{\nu}{\nu_0} \right)^{\beta_\sigma}, \quad (2.10)$$

$$\chi_\nu = \chi_0 \left(\frac{\nu}{\nu_0} \right)^{\beta_\chi}, \quad (2.11)$$

where β_κ , β_σ , and β_χ are the opacity spectral indices, and κ_0 , σ_0 , and χ_0 are the absorption, scattering, and extinction coefficients at the reference frequency ν_0 . These fits are shown in Figure (2.3) as thick solid lines, and Table (2.1) shows the results

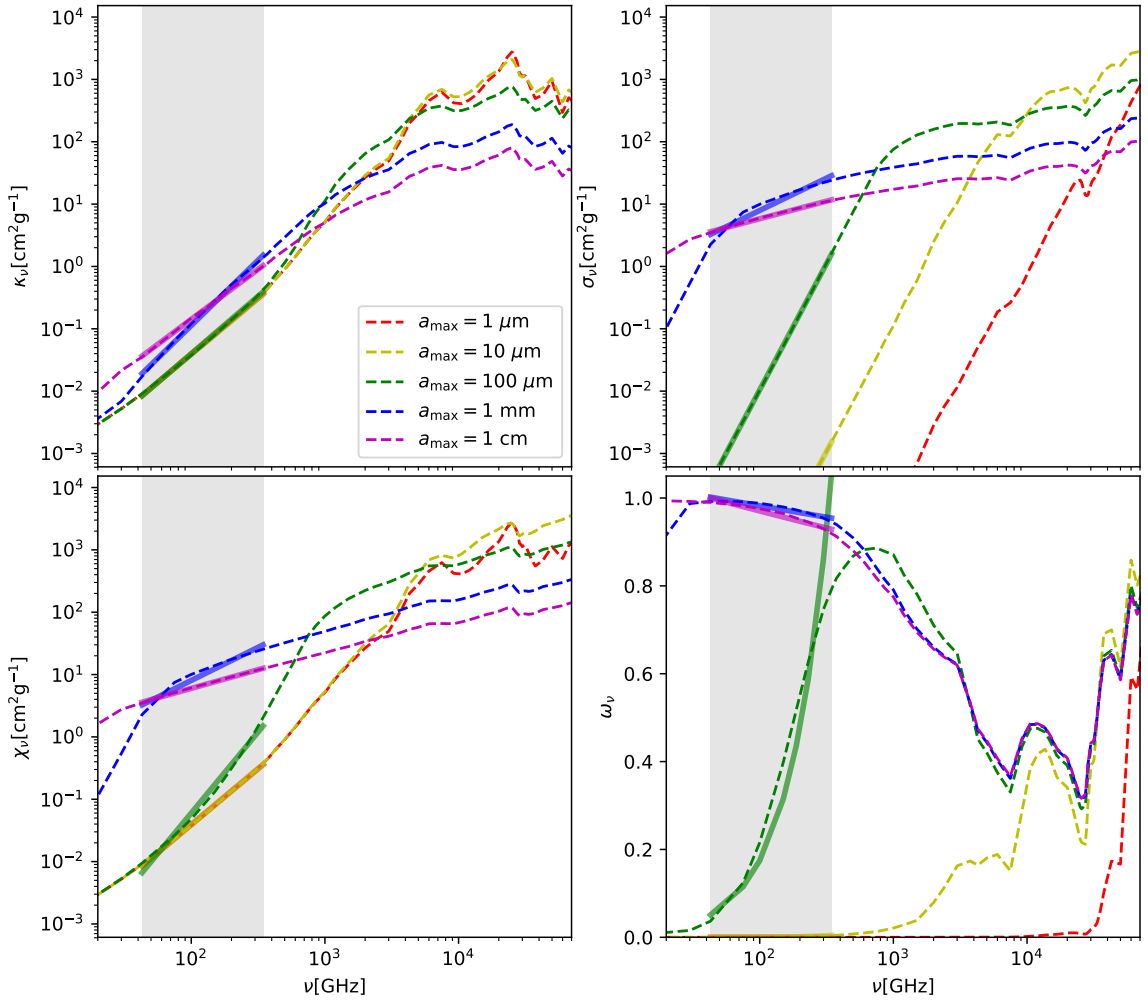


Figure 2.3: Dust opacity properties as a function of frequency. Top left panel: absorption coefficient. Top right panel: scattering coefficient. Bottom left panel: extinction coefficient. Bottom right panel: albedo. The red, yellow, green, blue and magenta curves are the cases where the maximum grain size is 1, 10, 100 μm , 1 mm, and 1 cm respectively. The slope of the particle size distribution in all cases is set to $p = 3.5$ and $a_{\min} = 0.05 \mu\text{m}$. The gray area is the region between $\lambda = 870 \mu\text{m}$ and 7 mm, and the solid lines within this region are the fits to each curve using a power-law function of the frequency.

from the fits for different maximum grain sizes.

Note that β_χ depends on the relative magnitudes of the absorption and scattering coefficients. $\beta_\chi \rightarrow \beta_\sigma$ if $\sigma_\nu >> \kappa_\nu$, and $\beta_\chi \rightarrow \beta_\kappa$ if $\kappa_\nu >> \sigma_\nu$. By definition,

$$\omega_\nu = \omega_0 \left(\frac{\nu}{\nu_0} \right)^{\beta_\omega}. \quad (2.12)$$

where $\beta_\omega = \beta_\sigma - \beta_\chi$.

The top left panel of Figure (2.4) shows the magnitude at $\nu_0 = 230$ GHz ($\lambda_0 = 1.3$ mm) of the extinction (solid line), absorption (dashed line), and scattering coefficients (dotted line) as a function of the maximum grain size. Their spectral indices are shown in the top right panel. The albedo and its spectral index are shown in the bottom left and right panels, respectively.

The opacity coefficients (extinction, absorption, and scattering) of Figure 2.4 have their maxima approximately at the same maximum grain size. Actually, the value of a_{\max} where the opacity coefficients have a maximum can be approximated by $a_{\max} \sim \lambda/\pi$. Note that this differs from the $a \sim \lambda/2\pi$ when comparing opacities of dust grains of a single size.

The albedo (bottom left panel) rapidly increases when $a_{\max} \sim 100$ μm , and it reaches a large ($0.8 \lesssim \omega_\nu \lesssim 0.9$) and constant ($\beta_{\omega_\nu} \sim 0$) value in the range $200 \mu\text{m} \lesssim a_{\max} \lesssim 1 \text{ cm}$. Therefore, the dust opacity is dominated by the scattering coefficient at mm wavelengths if a_{\max} is in the order of mm or cm.

The opacity spectral indices (top right panel) are fundamental to interpret the dust continuum millimeter observations. A common practice is to neglect the scattering opacity in the solution of the emergent intensity I_ν in the radiative transport equation, such that $I_\nu = B_\nu(T)(1 - e^{-\tau_\nu})$. In addition, if the emission is within the Rayleigh-Jeans regime ($B_\nu(T) \propto \nu^2$) and in the optically thin limit ($1 - e^{-\tau_\nu} \approx \tau_\nu \propto \nu^{\beta_\kappa}$), the emergent intensity can be written as $I_\nu \propto \nu^{2+\beta_\kappa}$. Then, fitting a power law to the observed $I_\nu \propto \nu^\alpha$, one obtains the opacity spectral index from $\beta_\kappa = \alpha - 2$, and the size of the dust grains can be inferred from the upper right panel of Figure (2.4). Many authors have questioned the Rayleigh-Jeans and optically thin assumptions; nevertheless, the main problem is that the scattering effects are not negligible at mm wavelengths for mm-cm dust grains.

So, for a given observed value of β_{obs} , the interpretation of the maximum grain size varies if it is compared with β_χ or β_κ . For example, for an observed value of $\beta_{\text{obs}} = 1.0$, the value of a_{\max} is around 1 mm if β_χ is used, but $a_{\max} > 10\text{cm}$ if β_κ is used to interpret β_{obs} . When scattering is not taken into account, the curve of β_κ is used. When scattering effects are included, the curve of β_χ should be used taking

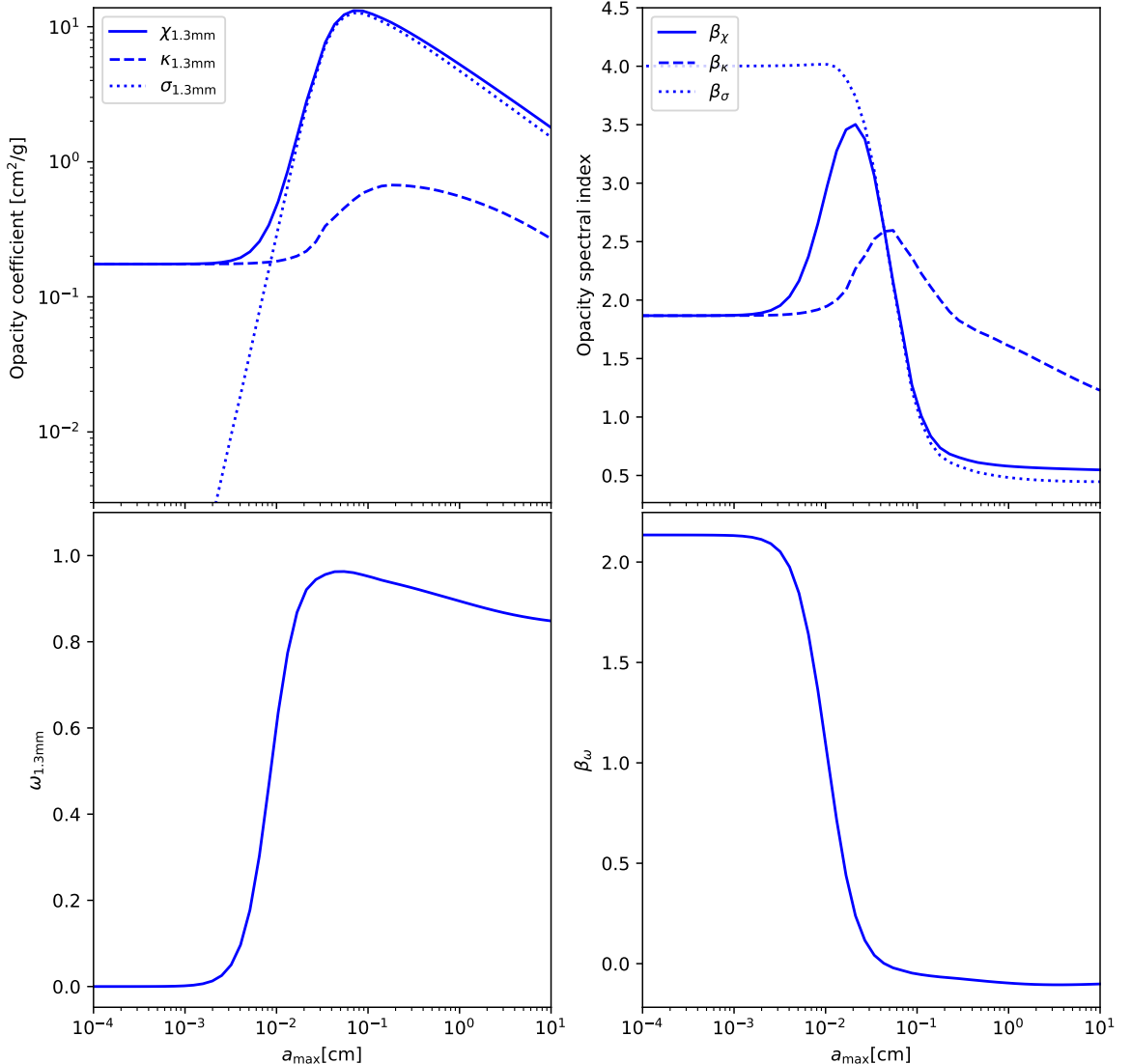


Figure 2.4: Dust opacity properties. Top left panel: opacity coefficients as a function of the maximum grain size at $\lambda = 1.3$ mm. The extinction, absorption, and scattering coefficients are represented by the solid, dashed and dotted line respectively. Top right panel: opacity spectral index of the extinction, absorption, and scattering coefficients. Bottom left panel: albedo as a function of the maximum grain size. Bottom right panel: albedo spectral index. In all panels, the slope of the particle size distribution is $p = 3.5$ and $a_{\min} = 0.05 \mu\text{m}$. The spectral indices are computed in the range between $\lambda = 0.87$ mm and 7 mm.

a_{\max}	$\kappa_{230\text{GHz}}$	β_κ	$\sigma_{230\text{GHz}}$	β_σ	$\chi_{230\text{GHz}}$	β_χ	$\omega_{230\text{GHz}}$	β_ω
1 μm	0.174	1.79	0	-	0.174	1.79	0	-
10 μm	0.174	1.79	0	-	0.174	1.80	0	-
100 μm	0.185	1.84	0.306	4.05	0.522	2.60	0.586	1.45
1 mm	0.646	2.09	18.8	1.04	19.5	1.06	0.963	-0.0234
1 cm	0.539	1.60	9.32	0.565	9.89	0.600	0.942	-0.0354

Table 2.1: Results from the fit to the dust opacity properties in Figure (2.4). The magnitude of the scattering and albedo for $a_{\max} = 1, 10 \mu\text{m}$ tends to 0.

also into account the modification of the source function from the typical Planck function (see next chapter).

Note also that β_κ only varies between ~ 1.3 ($a_{\max} \sim 10 \text{ cm}$) and ~ 2.5 ($a_{\max} \sim 400 \mu\text{m}$); however, β_χ varies from ~ 0.5 ($a_{\max} \sim \text{mm, cm}$) to ~ 3.5 ($a_{\max} \sim 200 \mu\text{m}$). Nevertheless, when the maximum grain size is very small ($a_{\max} \ll 100 \mu\text{m}$), the albedo is close to 0, and both β_χ , β_κ converge to 1.7, which is the typical value of the ISM (Draine, 2006).

2.2 Mie Theory

Mie theory is a general solution for the scattering of an electromagnetic wave from a spherical grain with uniform complex index of refraction. Mie theory has been longly used in the literature (even with the spherical grain assumption) because it provides a practical numerical implementation to compute the absorption and scattering coefficients and because it gives a complete and analytical solution to the interaction of the electric and magnetic field with a homogenous sphere based on the Maxwell's equations.

The opacity properties derived in this chapter were computed using the Mie Theory for spherical dust grains with sizes similar or smaller than the wavelength. This extension for small grains is valid as it can be mathematically prove that the Mie Theory reduces to the Rayleigh scattering for $x \ll 1$ (Bohren, & Huffman, 1983).

However, the dust growth in protoplanetary disks could generate dust particles with non-spherical geometries. This has been proven to occur using laboratory experiments (e.g. Blum et al. 2000) and numerical simulations (e.g Wada et al. 2007, Wada et al. 2008), then, can the Mie theory be extended to explain the opacity properties in protoplanetary disks for non-spherical grains?. This question has been addressed in many works, where the Mie theory is modified or partially used to compute the properties of non-spherical grains. For example, Semenov et al. (2003)

considers dust grains composed of small $0.01 \mu\text{m}$ grains, this inhomogeneity is very small compared with the shortest wavelength used ($0.1 \mu\text{m}$), such that the Mie theory is valid. A similar approach was also used in [Voshchinnikov et al. \(2005\)](#) to study the effect of the porosity on the opacity coefficients and albedo considering multilayered particles of different composition.

Whatever the case, there is not to date a scattering theory for non-spherical grains as powerful as the Mie theory for spherical grains, and this is the reason why the Mie theory has been extended as long as possible. [Bohren, & Huffman \(1983\)](#) summarizes at the end of chapter 13 the applicability of the Mie theory to non-spherical grains. One of the main differences is that the scattering of non-spherical grains could be highly azimuthally dependent. However, the spherical grains results from the Mie theory can be used to approximate the scattering of large non-spherical grains in the forward direction if they are replaced by spherical grains with an equivalent cross section area.

Chapter 3

Radiative Transfer

The interaction between light and matter is fundamental to interpret and infer properties of astronomical objects. The light captured by telescopes on Earth coming from distant objects interacts with all the material between the source and the observer, then, corrections are necessary to correctly understand the observed light. These corrections also carry information about the matter with which the light interacts and can be used to estimate its properties (as discussed in the previous chapter, dust grains are usually the main opacity source in the ISM).

This chapter describes the main properties of the radiative transfer equation, and provides an analytical solution to the scattered light in the disks (Section 3.1). The changes in the spectral index due to scattering are shown in Section (3.2), while an alternative solution (using the scattering effects) to the excess emission reported in many disks at $\lambda = 7$ mm is described in Section (3.4). The solution to the emergent intensity with scattering is simple but powerful, such that can be used to infer the dust properties using multi-wavelength observations. In Section (3.5), the model is applied to the disk around *HL Tau* to infer the dust temperature, albedo, size, optical depth and dust surface density.

3.1 Emergent intensity

The specific intensity I_ν is defined as the energy crossing an area dA in a time dt in the frequency range $d\nu$ within a solid angle $d\Omega$. In the cgs units, $[I_\nu] = \text{erg s}^{-1}$

$\text{cm}^{-2} \text{ sr}^{-1} \text{ Hz}^{-1}$. The first three moments of the specific intensity are

$$J_\nu = \frac{1}{2} \int_{-1}^1 I_\nu d\mu, \quad (3.1)$$

$$H_\nu = \frac{1}{2} \int_{-1}^1 \mu I_\nu d\mu, \quad (3.2)$$

$$K_\nu = \frac{1}{2} \int_{-1}^1 \mu^2 I_\nu d\mu, \quad (3.3)$$

where $\mu = \cos(\theta)$ is cosine of the polar angle between the direction of light and some reference plane, J_ν is the mean intensity, and H_ν , K_ν are proportional to the flux and radiation pressure, respectively.

When photons travel through matter, they can be absorbed or scattered and then, the specific intensity changes. The change of the specific intensity follows the radiative transfer equation

$$\mu \frac{dI_\nu}{d\tau_{\chi_\nu}} = -I_\nu + S_\nu(T), \quad (3.4)$$

where S_ν is the source function and τ_ν is the optical depth defined as

$$\frac{d\tau_{\chi_\nu}}{dZ} = \chi_\nu \rho_d, \quad (3.5)$$

where Z is the distance in the line of sight though the matter density ρ_d . Throughout this work, the extinction is assumed to occur due to the interaction of light with dust grains, then, the matter density refers to the dust density and the extinction coefficient is given in terms of cm^2 per gram of dust.

The right side of equation (3.4) has two terms, the first one is the decrease of the specific intensity, and the second one (source function) increases the specific intensity given the local emission of the source. In a medium with local temperature T , where the light is absorbed and/or scattered, the source function is given by

$$S_\nu(T) = (1 - \omega_\nu)B_\nu(T) + \omega_\nu J_\nu, \quad (3.6)$$

where $B_\nu(T)$ is the Planck function. If the properties of the medium in which the light travels are known (source function, absorption, and scattering coefficients), equations (3.4) and (3.5) can be integrated along some line of sight. The solution to the radiative transfer equation is called the emergent intensity. Figure (3.1) shows a schematic representation of this process.

In the case of protoplanetary disks, an analytic solution for the mean intensity

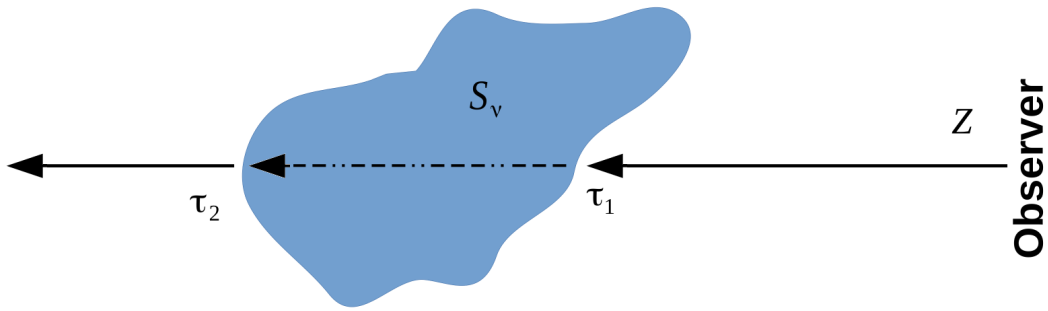


Figure 3.1: Representation of the radiative transport through a medium with source function $S_\nu(T)$. The light coming from the left side travels through the medium, which also emits and absorb radiation, and the output light (emergent intensity) is captured by the observer at the right side.

J_ν was found by Miyake & Nakagawa (1993) by assuming a plane parallel isothermal slab and the Eddington approximation ($K_\nu = \frac{1}{3}J_\nu$). Their solution is given by

$$J_\nu(t_{\chi_\nu}^p, \omega_\nu) = B_\nu(T) \left\{ 1 + \frac{\exp\left(-\sqrt{3(1-\omega_\nu)}t_{\chi_\nu}^p\right) + \exp\left(\sqrt{3(1-\omega_\nu)}(t_{\chi_\nu}^p - \tau_{\chi_\nu}^p)\right)}{(\sqrt{1-\omega_\nu} - 1) \exp\left(-\sqrt{3(1-\omega_\nu)}\tau_{\chi_\nu}^p\right) - (\sqrt{1-\omega_\nu} + 1)} \right\}, \quad (3.7)$$

where $\tau_{\chi_\nu}^p$ is total optical depth and $t_{\chi_\nu}^p$ is the optical depth coordinate (it indicates the depth into the disk), both measured perpendicular to the disk mid plane.

An analytical solution to the emergent intensity can be found assuming constant dust properties along the line of sight and a vertical isothermal disk. If the extinction coefficient (χ_ν) does not change along the line of sight (e.g. for face on disks with constant vertical properties above the mid plane or very settled disks with moderate inclinations), the optical depth (equation 3.5) is given by

$$\tau_{\chi_\nu} = \chi_\nu \Sigma_d^{\text{l.o.s.}}, \quad (3.8)$$

where $\Sigma_d^{\text{l.o.s.}}$ is the dust surface density along the line of sight.

Note that there is also an optical depth τ_{κ_ν} associated to the absorption coefficient κ_ν . Its definition is equivalent to the optical depth associated to the extinction (equation 3.8) but with the absorption coefficient instead of the extinction coefficient. If the absorption coefficient does not change along the line of sight, the solution of the optical depth associated to the absorption coefficient is given by

$$\tau_{\kappa_\nu} = \kappa_\nu \Sigma_d^{\text{l.o.s.}}. \quad (3.9)$$

Due to the relation between both coefficients (equation 2.8), the optical depths are related by the albedo as

$$\tau_{\chi_\nu} = \frac{\tau_{\kappa_\nu}}{1 - \omega_\nu}. \quad (3.10)$$

For example, if $\omega_\nu = 0.9$ (expected for mm grains at mm wavelengths), then, the optical depth associated to the extinction coefficient is one order of magnitude larger than that associated to the absorption coefficient. For such large albedo, the term associated to the direct emission of the source function (first term of equation 3.6) is only 10% of the black body emission, while the rest is scattered light. The increase of the optical depth and the decrease of the contribution of the black body emission approximately cancel each other in the radiative transfer equation, in such a way that the emergent intensity with scattering is within a factor of 2 of the case without scattering, as it will be shown below.

Substituting equations (3.6, 3.7, 3.10) into equation (3.4), and integrating the radiative transfer equation, the emergent intensity for a vertically isothermal disk is given by

$$I_\nu^{\text{sca}} = B_\nu(T) \left[1 - \exp \left(-\frac{\tau_{\kappa_\nu}}{\mu \epsilon_\nu^2} \right) + (1 - \epsilon_\nu^2) \mathcal{F}(\tau_{\kappa_\nu}, \epsilon_\nu) \right], \quad (3.11)$$

where

$$\begin{aligned} \mathcal{F}(\tau_{\kappa_\nu}, \epsilon_\nu) &= \frac{1}{(\epsilon_\nu - 1) \exp \left(-\sqrt{3} \frac{\tau_{\kappa_\nu}}{\epsilon_\nu} \right) - (\epsilon_\nu + 1)} \times \\ &\quad \left\{ \frac{1 - \exp \left[-(\sqrt{3} \epsilon_\nu + \mu^{-1}) \frac{\tau_{\kappa_\nu}}{\epsilon_\nu^2} \right]}{\sqrt{3} \epsilon_\nu \mu + 1} + \frac{\exp \left[-\frac{\tau_{\kappa_\nu}}{\mu \epsilon_\nu^2} \right] - \exp \left[-\sqrt{3} \frac{\tau_{\kappa_\nu}}{\epsilon_\nu} \right]}{\sqrt{3} \epsilon_\nu \mu - 1} \right\}, \end{aligned} \quad (3.12)$$

and $\epsilon_\nu = +\sqrt{1 - \omega_\nu}$. In this solution, τ_{κ_ν} and ω_ν are chosen to describe the emergent intensity because they are independent variables. These analytical equations were first derived at [Sierra et al. \(2019\)](#). Previously, [D'Alessio et al. \(2001\)](#) used equations (3.6-3.7) and numerically integrate the radiative transfer equation (equation 3.4) in order to find the emergent intensity.

Equations (3.11-3.12) gives the solution of the emergent intensity in the scattering case, when both the absorption and scattering effects are taken into account. Note that the scattering does not emit by itself, but only redirects the emission from the pure absorption case, then, if the absorption component is not included, the emergent intensity is zero. If scattering is neglected ($\omega_\nu = 0$), then, equation (3.11) reduces to the well known pure absorption emergent intensity

$$I_\nu^{\text{abs}} = B_\nu(T) [1 - \exp(-\tau_{\kappa_\nu}/\mu)]. \quad (3.13)$$

Both solutions (equations 3.11, 3.13) are valid when the dust temperature along the line of sight does not change, e.g. for vertically isothermal disk with a face-on orientation (or moderate inclinations) as discussed above. The effect of the change of temperature could also modify the emergent intensity depending on what is the temperature profile before the disk becomes optically thick. These effects will be explored in a future work.

The ratio between the emergent intensities for the case when scattering is included and the pure absorption case is defined as

$$\mathcal{R}_\nu = \frac{I_\nu^{\text{sca}}}{I_\nu^{\text{abs}}}. \quad (3.14)$$

From now on, the optical depth regime (as thin or thick) refers to absorption optical depth τ_{κ_ν} . Note that, even if $\tau_{\kappa_\nu} \ll 1$, τ_{χ_ν} can be large if $\omega_\nu \sim 1$. The ratio \mathcal{R}_ν in the optically thin and optically thick limits is given by

$$\mathcal{R}_\nu = \begin{cases} 1 & , \tau_{\kappa_\nu} \ll 1 \\ 1 - \frac{\omega_\nu}{(\sqrt{1-\omega_\nu}+1)(\sqrt{3(1-\omega_\nu)}\mu+1)} & , \tau_{\kappa_\nu} \gg 1. \end{cases} \quad (3.15)$$

Figure (3.2) shows the ratio \mathcal{R}_ν as a function of τ_{κ_ν} and ω_ν for a face-on disk ($\mu = 1$). The isocontours where $\mathcal{R}_\nu = 0.9$, 1, and 1.1 are plotted as dashed lines as reference. Note that the values $0.9 < \mathcal{R}_\nu < 1.1$ dominate most of the area of the parameter space. The area where $\mathcal{R}_\nu > 1.1$ only occurs where the disk is optically thin and the albedo is large. This increase occurs due to the change of the optical depths regimes in the absorption and scattering cases. In this region $\tau_{\kappa_\nu} < 1$ but $\tau_{\chi_\nu} > 1$; then, the emergent intensities can be approximated as $I_\nu^{\text{abs}} \approx B_\nu(T)\tau_{\kappa_\nu}$, and $I_\nu^{\text{sca}} \approx B_\nu(T)$, respectively, and $R_\nu \sim 1/\tau_{\kappa_\nu} > 1$. The region where $\mathcal{R}_\nu < 0.9$ occurs in the optically thick regime and high albedo. The latter increases the total optical depth of the disk and the mean free path of the photons decreases. In consequence, a small fraction of photons can escape from the disk and the emergent intensity I_ν^{sca} decreases. For example, for $\omega_\nu = 0.95$, the ratio $\mathcal{R}_\nu = 0.44$.

3.2 Spectral index

Even if the albedo is constant for mm and cm dust grains (Figure 2.4), the variation of the optical depth at different wavelengths modifies the emergent intensity I_ν^{sca} compared with the absorption case I_ν^{abs} , as shown in Figure (3.2). If the albedo is $\omega_\nu \gtrsim 0.6$, the emergent intensity in the scattering case decreases at optically thick

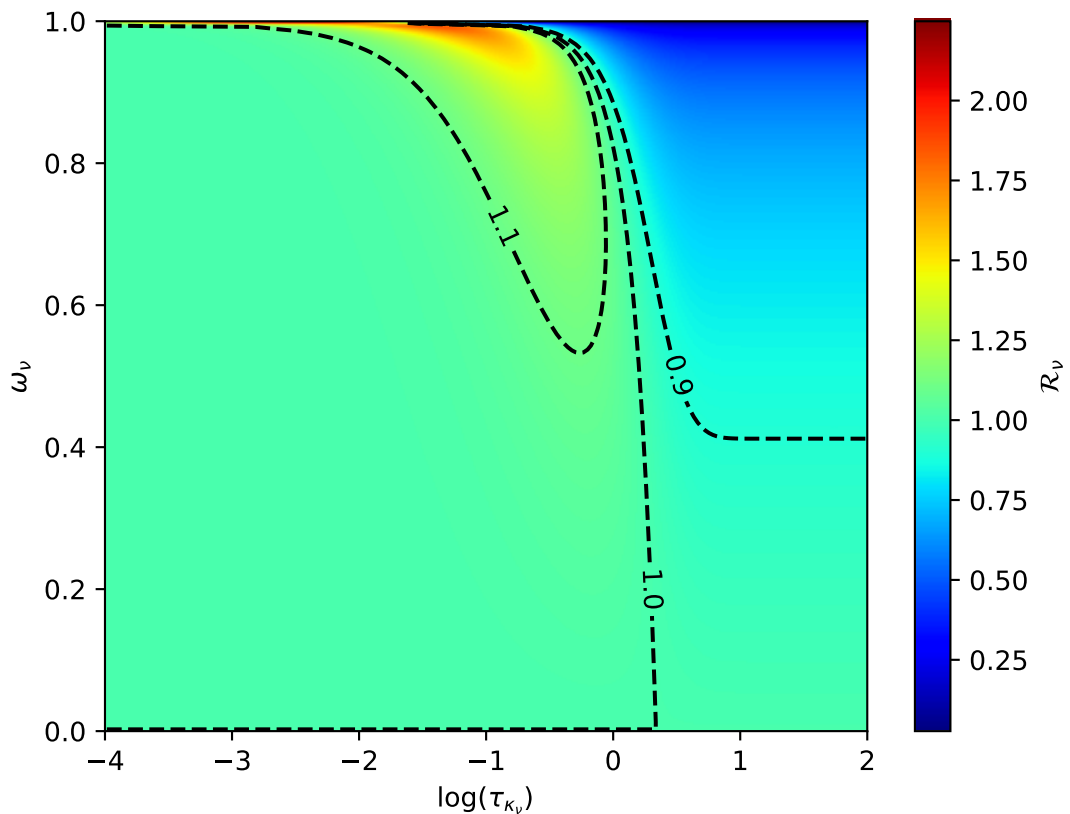


Figure 3.2: Ratio between the emergent intensity with scattering effects and without scattering effects as a function of the optical depth associated to the absorption and the albedo. The isocontours show the region where \mathcal{R}_ν is 0.9, 1.0, and 1.1.

wavelengths, and increases for $-2 \lesssim \log(\tau_{\kappa_\nu}) \lesssim -1$. Therefore, one expects changes of the spectral indices in the scattering case with respect to the pure absorption case.

The spectral index between the frequencies ν_1 and ν_2 in the pure absorption case is defined as

$$\alpha_{\nu_1, \nu_2}^{\text{abs}} = \frac{\log(I_{\nu_1}^{\text{abs}} / I_{\nu_2}^{\text{abs}})}{\log(\nu_1 / \nu_2)}, \quad (3.16)$$

while in the scattering case the spectral index is

$$\alpha_{\nu_1, \nu_2}^{\text{sca}} = \frac{\log(I_{\nu_1}^{\text{sca}} / I_{\nu_2}^{\text{sca}})}{\log(\nu_1 / \nu_2)}. \quad (3.17)$$

From the definition of \mathcal{R}_ν (equation 3.14) the spectral indices are related by

$$\alpha_{\nu_1, \nu_2}^{\text{sca}} = \frac{\log(\mathcal{R}_{\nu_1} / \mathcal{R}_{\nu_2})}{\log(\nu_1 / \nu_2)} + \alpha_{\nu_1, \nu_2}^{\text{abs}}. \quad (3.18)$$

The top panels of Figure (3.3) show the spectral indices $\alpha_{\lambda_1, \lambda_2}^{\text{sca}}$ ¹ between consecutive wavelengths for $\lambda = 0.87, 1.3, 3.0, 7.0$ mm and 1 cm, from left to right as a function of the optical depth at $\lambda = 1.3$ mm, and the maximum grain size. The slope of the particle size distribution is set to $p = 3.5$ and the temperature is set to $T = 100$ K². The dust properties used are the same as those in Figure (2.4). The bottom panels of the same Figure show the spectral indices in the pure absorption case $\alpha_{\lambda_1, \lambda_2}^{\text{abs}}$. The color bar is the same for all panels. Isocontours where the spectral index is 2.0 (typical of optically thick emission in the Rayleigh-Jeans limit), 3.0, and 3.7 (the ISM value), are shown in all the panels as black dashed lines.

In the absorption case (bottom panels) one can see that for very optically thick disks ($\log(\tau_{\kappa_{1.3\text{mm}}}) \gg 0$), the value of $\alpha_{\lambda_1, \lambda_2}^{\text{abs}}$ tends to 2. Usually, values of $\alpha < 3.7$ are interpreted as grain growth for disks in the optically thin regime (e.g. Beckwith, & Sargent 1991, Natta, & Testi 2004). For example, the spectral index $\alpha_{7.0-10.0\text{mm}}^{\text{abs}}$ is between 3.0 and 3.7 for optically thin disks ($\log(\tau_{\kappa_{1.3\text{mm}}}) < 0$) and large dust grains ($\log(a_{\max}[\text{cm}]) \gtrsim -0.5$). However, these spectral indices can also be explained by disks in the optically thick regime ($0.5 \lesssim \log(\tau_{\kappa_{1.3\text{mm}}}) \lesssim 1.5$) and very small grains ($\log(a_{\max}[\text{cm}]) \lesssim -2$).

The scattering case (top panels) in the optically thin region has the same spec-

¹For simplicity, the notation is changed from $\alpha_{\nu_1, \nu_2}^{\text{sca}}$ to $\alpha_{\lambda_1, \lambda_2}^{\text{sca}}$, where $\lambda\nu = c$ and c is the speed of light.

²The indices would change with respect to those shown in Figure (3.3) only in the case of very cold disks ($T \lesssim 10$ K), where the peak of the black body radiation is displaced to the sub-mm range according to Wien's law, $\lambda_{\text{peak}}T = 0.29$ cm K

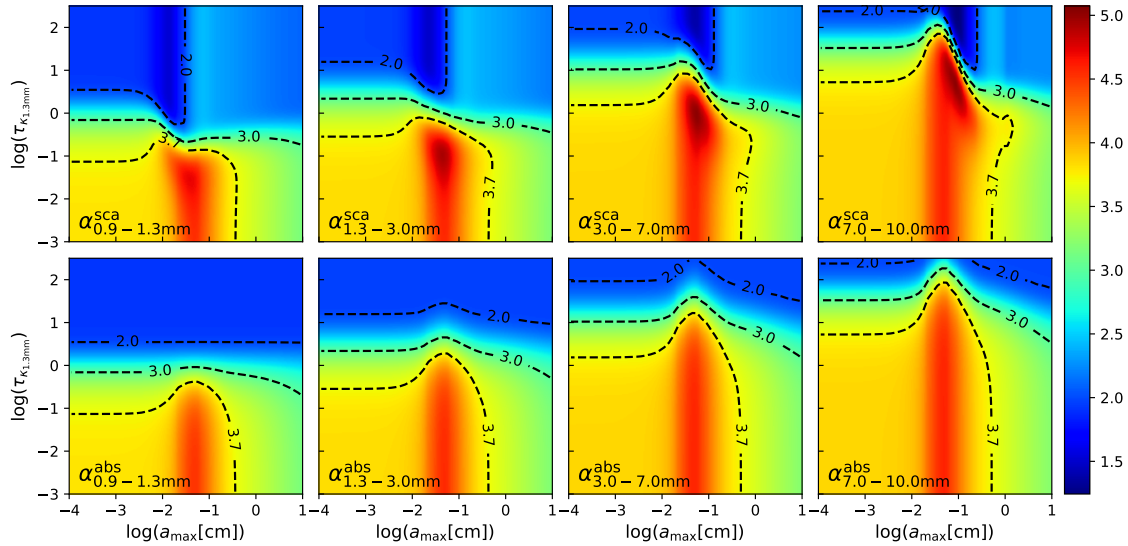


Figure 3.3: Spectral indices in the mm range as a function of the optical depth at 1.3 mm and the maximum grain size. The slope of the particle size distribution is fixed to $p = 3.5$ and the temperature is $T = 100$ K. In the top panels the scattering effects are taken into account, while in the bottom panels they are ignored. The color bar is the same in all panels.

tral indices than in the pure absorption case. This occurs because the emergent intensities with or without scattering coincides at this optical depth regime, $\mathcal{R}_\nu \sim 1$ (equation 3.15). This behaviour is evident in Figure (3.3) for $\log(\tau_{\kappa_{1.3\text{mm}}}) < -2$.

In the optically thick regime ($\log(\tau_{\kappa_{1.3\text{mm}}}) \gg 0$), there are two regions in the parameter space: the first region has $\log(a_{\max}[\text{cm}]) < -2$, which has an albedo around 0 at all wavelengths (see Figure 2.2), therefore $\mathcal{R}_\nu \sim 1$ (see Figure 3.2), and the spectral indices are the same as in the pure absorption case. The second region has $\log(a_{\max}[\text{cm}]) > -2$, which has a significant albedo and where the emergent intensities (compared with the pure absorption case) change according to the albedo and optical depth (Figure 3.2). Changes of the albedo or the optical depth with frequency modifies \mathcal{R}_ν and, thus, the spectral index in the scattering case changes with respect to the true absorption case according to equation (3.18).

For example, if a disk is optically thick at 3 mm but optically thin at 7 mm, the emergent intensity decreases and increases respectively compared with the true absorption case. Therefore, the spectral indices between these wavelengths in the scattering and true absorption cases differ.

Figure (3.4) shows the spectral indices $\alpha_{0.9-1.3\text{mm}}$ (red curves), $\alpha_{1.3-3.0\text{mm}}$ (green curves), $\alpha_{3.0-7.0\text{mm}}$ (blue curves), and $\alpha_{7.0-10\text{mm}}$ (magenta curves) for the scattering (solid lines) and absorption (dotted lines) cases and different optical depth regimes: $\log(\tau_{\kappa_{1\text{mm}}}) = -3, -1, 0$, and 2.5 indicated on the top right corner of each panel.

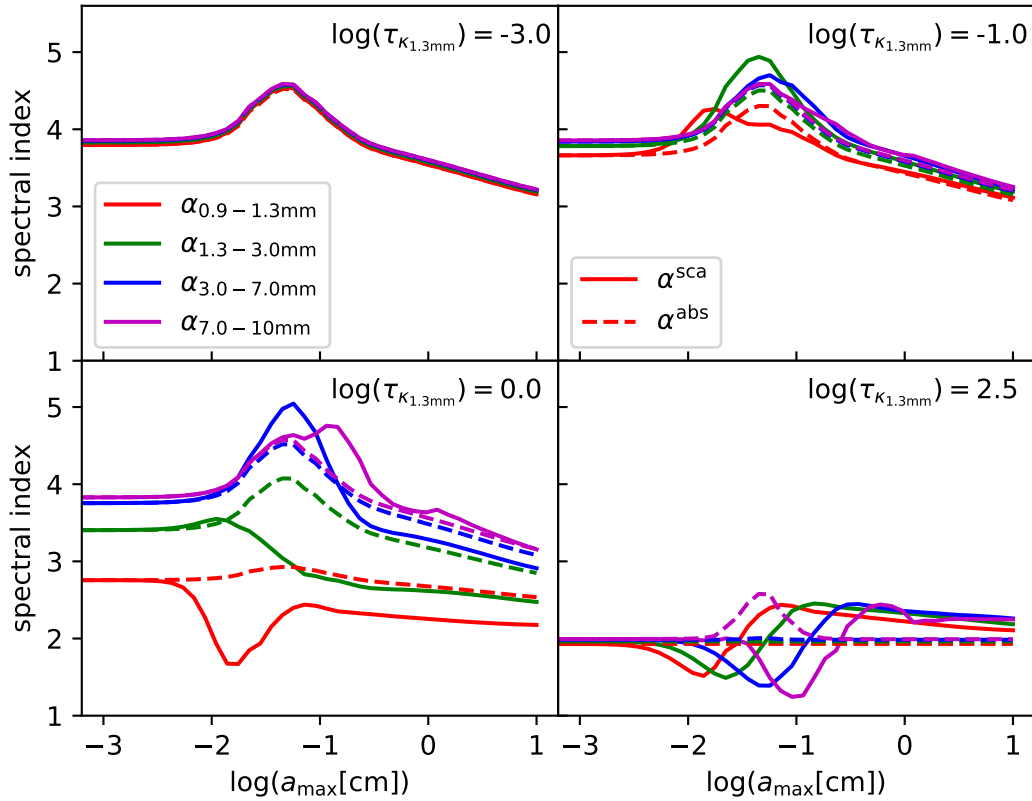


Figure 3.4: Spectral indices as a function of a_{\max} for $\log(\tau_{\kappa_{1.3\text{mm}}}) = -3, -1, 0$ and 2.5 from left to right and from top to bottom respectively. The solid and dotted curves are the scattering and the pure absorption models respectively, while each color represent the spectral index shown in the top left panel.

Note that in all the cases, the spectral index in the scattering and pure absorption cases coincide for $\log(a_{\max}) < -2.5 \mu\text{m}$, where $\omega_{\nu} \sim 0$. Also, they are the same for all the grain sizes in the optically thin regime at all frequencies (top right panel). Furthermore, in this limit, the value of the spectral index coincides with the usual assumption $\alpha^{\text{abs}} = \alpha^{\text{sca}} = \beta_{\kappa_{\nu}} + 2$ (see top right panel of Figure 2.4).

The properties of the spectral indices can be used to constrain physical parameters in observational disks as follows: If an observational spectral index is measured with its respective error bar, one can use the panels shown in Figure (3.3) to constrain the parameter space within the error of α_{obs} . If more than one spectral index is measured, one looks for the intersection of the parameter space ($\tau_{\kappa_{1.3\text{mm}}}, a_{\max}$) that reproduces the observed indices.

The bottom right panel of Figure (3.4), which is the most optically thick case, the spectral indices can be lower than 2 in the scattering case. For example, it shows that the values of the maximum grain size where $\alpha_{0.9-1.3\text{mm}} < 2$ vary from $10^{-2.5} \lesssim a_{\max}/\text{cm} \lesssim 10^{-1.5}$, consistent with the discussion in Liu (2019). Note

that larger grains are required to produce spectral indices smaller than 2 at longer wavelengths. Alternative explanations of this anomalously low spectral indices have been proposed , e.g. they can be produced in the case of the pure absorption by an optically thick disk with a radially decreasing temperature and self-obscuration ([Galván-Madrid et al., 2018](#)). The effect of the temperature gradient on the spectral indices is explored in the following subsection.

3.3 Dust settling and temperature effect

The previous results assume a vertically isothermal disk and constant maximum grain size above the disk mid plane, however, it is known that the disk temperature varies as a function of the height above the mid plane because the stellar irradiation (which heats the disk surface) does not penetrate to the most optically thick region of the disk³, while accretion increases the temperature at the disk mid plane [D'Alessio et al. \(1998\)](#). Also, dust settling has been inferred in protoplanetary disks (e.g. [Pinte et al. 2016](#)), which decreases the maximum grain size in the disk surface (e.g. [Dubrulle et al. 1995](#)), so one can expect that the maximum grain size decreases with the height above the mid plane.

This section explores the effects of the vertical temperature and the dust settling on the emergent emission and the spectral indices. In subsection [3.3.1](#) the maximum grain size is fixed and the vertical temperature is taken into account, in subsection [3.3.2](#) the maximum grain size above the mid plane is changed using an analytical model derived from the model of [Dubrulle et al. \(1995\)](#).

3.3.1 Vertical temperature

We consider that the disk is heated by viscous dissipation (accretion) and stellar irradiation. The first one heats the disk mid plane and the second one heats the disk surface. The structure of the vertical temperature can be computed following the results from [Chiang, & Goldreich \(1997\)](#) and [D'Alessio et al. \(1998\)](#). In that works, the accretion and the irradiation by the central star set a vertical disk temperature $T(z)$ given by

$$T^4(z) = T_{\text{acc}}^4(z) + T_{\text{irr}}^4(z), \quad (3.19)$$

where

$$T_{\text{acc}}^4(z) = \frac{3}{4}\tau_{\text{av}}T_{\text{eff}}^4 \quad (3.20)$$

³Measured from the star perspective.

is the disk temperature due to accretion (it is maxima at the disk mid plane), τ_{av} is the average optical depth at wavelengths of dust thermal emission (here we choose $\tau_{\text{av}} = \tau_{\chi 1.3\text{mm}}$),

$$T_{\text{irr}}^4(z) = e^{-\tau_{\text{av}}} \frac{L_*}{16\pi\varpi^2\sigma_B} = e^{-\tau_{\text{av}}} \frac{T_*^4}{4} \left(\frac{R_*}{\varpi} \right)^2 \quad (3.21)$$

is the temperature due to the irradiation of the central star, L_* is the star luminosity, σ_B is the Stefan-Boltzmann constant, R_* is the star radius, ϖ is the distance from the star, and the effective temperature at the disk surface is given by

$$T_{\text{eff}}^4 = \varphi \frac{L_*}{4\pi\sigma_B\varpi^2} = \varphi T_*^4 \left(\frac{R_*}{\varpi} \right)^2, \quad (3.22)$$

where φ is the angle between the stellar radiation and the disk surface, with a typical value of $\varphi = 0.05$.

Then, the vertical disk temperature can be written as

$$T^4(z) = \left[\frac{3}{4}\tau_{\text{av}}\varphi + \frac{e^{-\tau_{\text{av}}}}{4} \right] \left(\frac{R_*}{\varpi} \right)^2 T_*^4. \quad (3.23)$$

The first term within the brackets increases the temperature toward the mid plane due to accretion and the second one increases the temperature toward the disk surface due to the stellar irradiation. Figure (3.5) shows the vertical disk temperature as a function of the optical depth. In this figure, the mid plane is at $\tau_{\text{av}} = 10$, where the mid plane disk temperature increases due to the accretion heating. However, in a less massive disk, the mid plane could be located for example at $\tau_{\text{av}} = 1$, and the temperature profile would decrease from the disk surface to the mid plane because the optical depth is not high enough to heat the disk mid plane. This temperature profile is the same to that shown in Figure 4 of [D'Alessio et al. \(1998\)](#).

Figure (3.6) shows the effects of the vertical temperature on the ratio \mathcal{R}_ν (first row), the spectral index in the scattering case (second row) and in the absorption case (third row). The wavelength is indicated in the top right corner of each panel. In all the panels, the green and magenta lines represent the properties with and without vertical temperature gradient, respectively; and the dashed and solid lines are the solution for the optically thin and thick regimes, respectively.

Note that when the vertical temperature structure is taken into account, the ratio \mathcal{R}_ν decreases compared with the vertically isothermal model in the optically thick regime, while it does not change in the optically thin regime.

The spectral indices in the scattering case and constant temperature coincide with the results recently shown in [Zhu et al. \(2019\)](#). The inferred spectral indices in

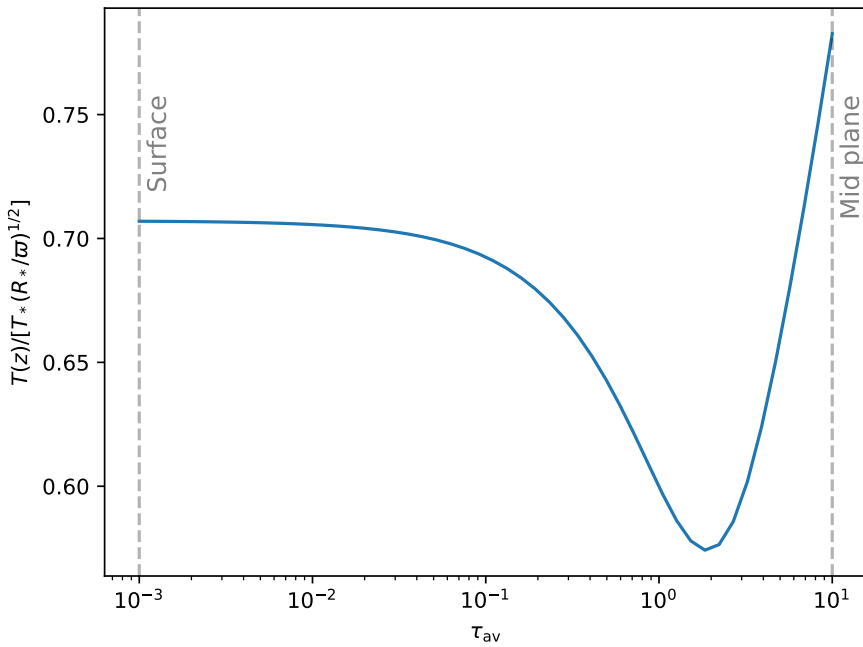


Figure 3.5: Vertical temperature structure as a function of the disk optical depth due to stellar irradiation on the disk surface and accretion heating in the mid plane.

the optically thick regime when the temperature structure is taken into account are smaller than those inferred with a vertically isothermal model. This occurs because the larger wavelengths can penetrate to regions closer of the mid plane, where the temperature rapidly increases due to accretion, so one expects that the spectral indices show a larger effect than in the vertically isothermal model. For example, the spectral index between 7 mm and 10 mm could reach a value close to 0 in the optically thick case if the maximum grain size is ~ 1 mm.

The spectral indices in the absorption case show the well known properties, they are $\alpha^{\text{abs}} = \beta_{\kappa\nu} + 2$ in the optically thin regime, $\alpha^{\text{abs}} = 2$ in the optically thick regime with constant temperature, and $\alpha^{\text{abs}} < 2$ in the optically thick regime with a gradient temperature (e.g. [Galván-Madrid et al. 2018](#)).

3.3.2 Dust settling

According to the results from [Dubrulle et al. \(1995\)](#), the scale height of dust grains with a Stokes number St is

$$h_d(a) = H_g \left[1 + (\gamma + 1)^{1/2} \frac{St}{\alpha_t} \right]^{-1/2}, \quad (3.24)$$

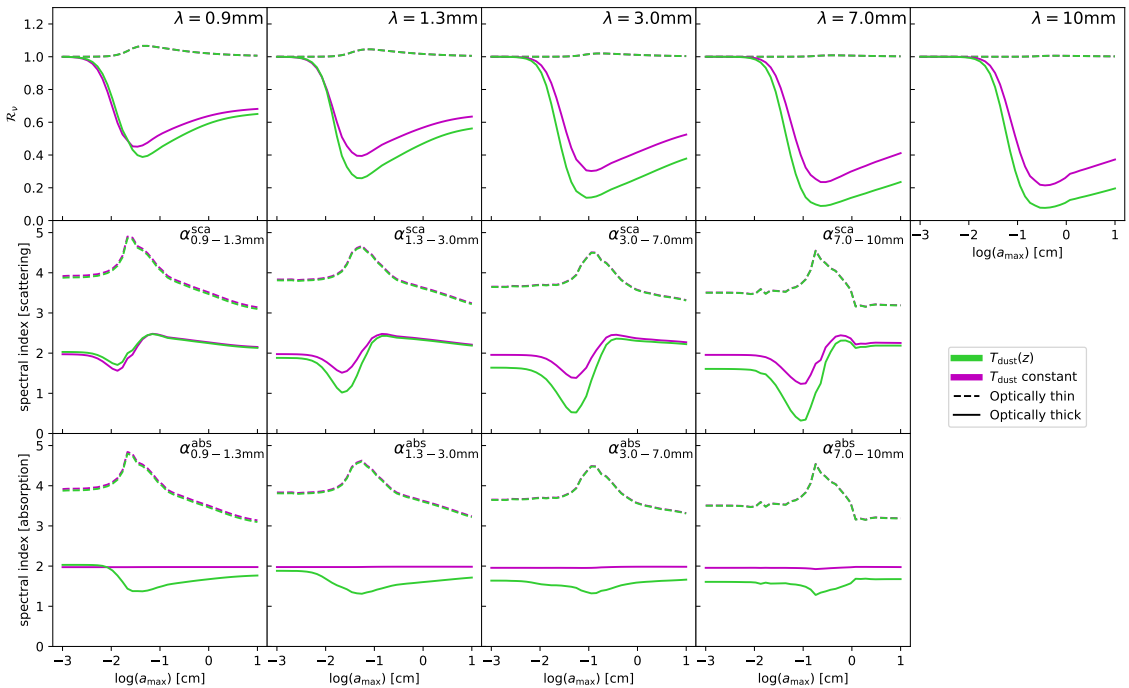


Figure 3.6: Effect of the temperature gradient in the ratio \mathcal{R}_ν (first row), the spectral index in the scattering and absorption case (second and third row, respectively) as a function of the maximum grain size. The observed wavelength increases from left (0.9 mm) to right (1 cm). In all the panels, the green lines are the properties with a temperature model that varies with the height above the mid plane and the magenta lines with constant temperature. The dashed and solid lines are the optically thin and optically thick regimes, respectively.

where H_g is the gas scale height, γ is an exponent related to at what scale the energy is injected into the turbulence (we assume compressible turbulence with $\gamma = 2$), α_t is the turbulence parameter given by the [Shakura, & Sunyaev \(1973\)](#) relation, and $St = \pi\rho_m a/(2\Sigma_g)$ is the Stokes number for a grain with material density ρ_m and within a gas surface density Σ_g . Then, the dust density for grains of size a is given by

$$\rho_d(a) = \rho_{d,0} \exp\left[-\frac{1}{2}\frac{z^2}{h_d(a)^2}\right]. \quad (3.25)$$

If one considers that the dust grains with size a are completely depleted at a height $z = 3h_d(a)$ (where their density decreases by a factor of 99.7% with respect with the mid plane density), then, from equation (3.24) one can derive the maximum grain size as a function of the height above the mid plane as

$$a_{\max}^{\text{settling}}(z) = \frac{2\Sigma_g \alpha_t}{\pi \rho_m} (\gamma + 1)^{-1/2} \left[\frac{9H_g^2}{z^2} - 1 \right]. \quad (3.26)$$

This equation gives the limit of the maximum grain size at a height z , but it cannot be larger than the true maximum grain size of the disk. Then, if the largest grain size in the disk is 1 cm, the maximum grain size model is given by

$$a_{\max}(z) = \min(a_{\max}^{\text{settling}}(z), 1 \text{ cm}). \quad (3.27)$$

The dust settling also changes the particle size distribution as a function of the height above the mid plane. The particle size distribution after dust settling $n_2(a)$ can be found (see detailed derivation on section [4.4.3.5](#)) as

$$n_2(a) \propto n(a) \frac{\rho_d(a)}{h_d(a)}, \quad (3.28)$$

where $n(a)$ is the original particle size distribution. Note that if $\alpha_t \rightarrow \infty$ (large turbulence), then $h_d(a)$ and $\rho_d(a)$ are independent of the grain size and the particle size distribution does not change. The right side of equation (3.28) is fitted using a single power law $n_2(a) \propto a^{-p_2}$ between a minimum grain size $a_{\min} = 0.05 \mu\text{m}$ and the maximum grain size $a_{\max}(z)$ in order to compute the local opacity properties.

Figure (3.7) shows the maximum grain size (left panel) and the slope of the particle size distribution (right panel) as a function of the height above the mid plane for different α_t values (see legend at the bottom left corner of the right panel). The value of $\log(\alpha_t) = 0.0$ (high turbulence) recovers the same maximum grain grain size at all height above the mid plane and the slope of $p \approx 3.5$, however, typical

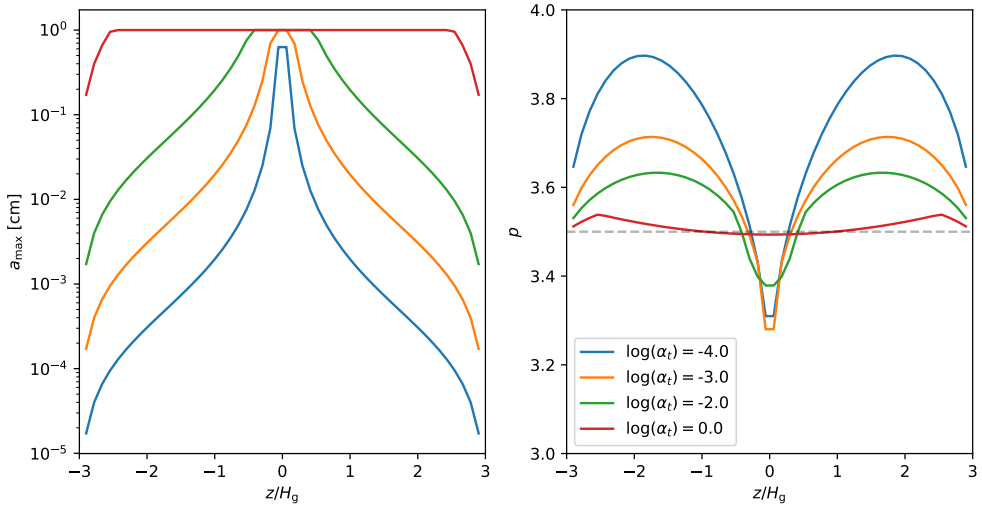


Figure 3.7: Settling model. Maximum grain size (left panel) and slope of the particle size distribution (right panel) as a function of the height above the mid plane. The color of each curve corresponds to a model with different α_t parameter, see legend on the bottom left corner of the right panel.

values of the α_t parameter ($\sim 10^{-3}$) are not high enough to prevent the dust settling, e.g. the maximum grain size is around $30 \mu\text{m}$, $200 \mu\text{m}$ and 2 mm at $z/H_g = 1$ for $\log(\alpha_t) = -4, -3, -2$, respectively.

Figure (3.8) shows the effects of the dust settling on the ratio \mathcal{R}_ν (first row), the spectral indices in the scattering case (second row), and in the absorption case (third row) as a function of the α_t parameter. The wavelength is indicated in the top right corner of each panel. In all the panels, the light blue and orange lines represent the properties with and without vertical temperature gradient, respectively; and the dashed and solid lines are the optically thin and thick regime, respectively. Similarly to the results of Figure (3.6), the temperature vertical gradient decreases all the spectral indices compared with the vertically isothermal model.

The similarity between this Figure (3.8) and Figure (3.6) is not a coincidence. For small turbulence ($\log(\alpha_t) < -2$) and in the optically thick regime, the emission is dominated by the small grains in the upper layers of the disk, which have a small albedo at mm wavelengths, then $\mathcal{R}_\nu \sim 1$ and $\alpha^{\text{sca}} = \alpha^{\text{abs}} = 2$. The maximum grain size in the upper layers of the disk increases with α_t , then, the spectral indices are characterized by the properties of these large grains. Moreover, note from equation (3.27) than $a_{\max}(z) \propto \alpha_t$, then α_t is equivalent way to measure $a_{\max}(z)$ in the optically thick regime.

In the optically thin regime, there are not hidden dust grains due to optical depth effects and $\mathcal{R}_\nu \sim 1$ for all α_t ; and the spectral indices coincide between the models

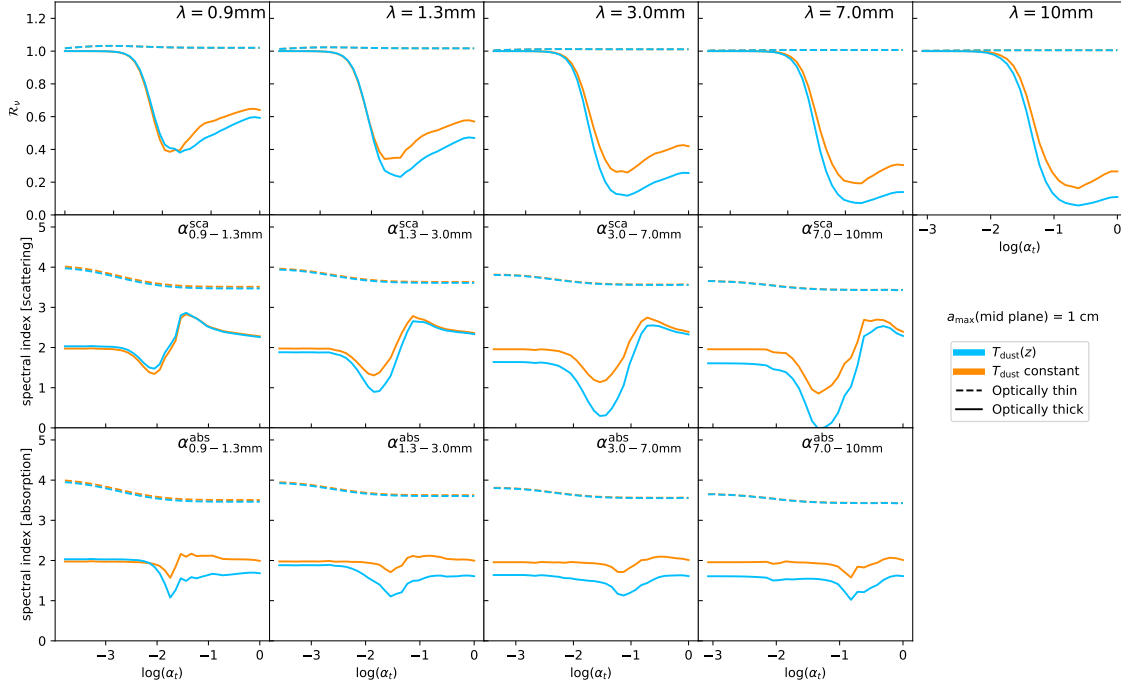


Figure 3.8: Effect of the settling in the ratio \mathcal{R}_ν (first row), the spectral index in the scattering and absorption case (second and third row, respectively) as a function of the α_t parameter. The observed wavelength increases from left (0.9 mm) to right (1 cm). In all the panels, the light blue lines are the properties with a temperature model that varies with the height above the mid plane and the orange lines have constant temperature. The dashed and solid lines are the optically thin and optically thick regimes, respectively.

where the vertical temperature gradient is taken or not into account.

3.3.3 Spectral Energy Distribution

The inclusion of scattering in the radiative transfer equation modifies the spectral indices, as shown in the above section. This means that the shape of the spectral energy distribution (SED) is modified with respect to the pure absorption case. In this section we explore the effects of the scattering on the SED for a given disk model with different inclination angles with respect to the plane of the sky.

The disk model is given by the azimuthally average radial profiles of the disk used in Section 4.5 below, where the disk is assumed to be in hydrostatic equilibrium and the dust surface density is given by $\Sigma_d = 25(\varpi/\text{au})^{-1}$. The maximum grain size is set to $a_{\max} = 1 \text{ mm}$ in all the disk. Using equations (3.6) and (3.7) one can construct the 3D source function in the disk and integrate the radiative transfer equation along a given line of sight to obtain the SED.

The left panel of Figure (3.9) shows the SED for different inclination angles $\mu = \cos(i)$, where i is the inclination angle of the disk with respect to the plane of

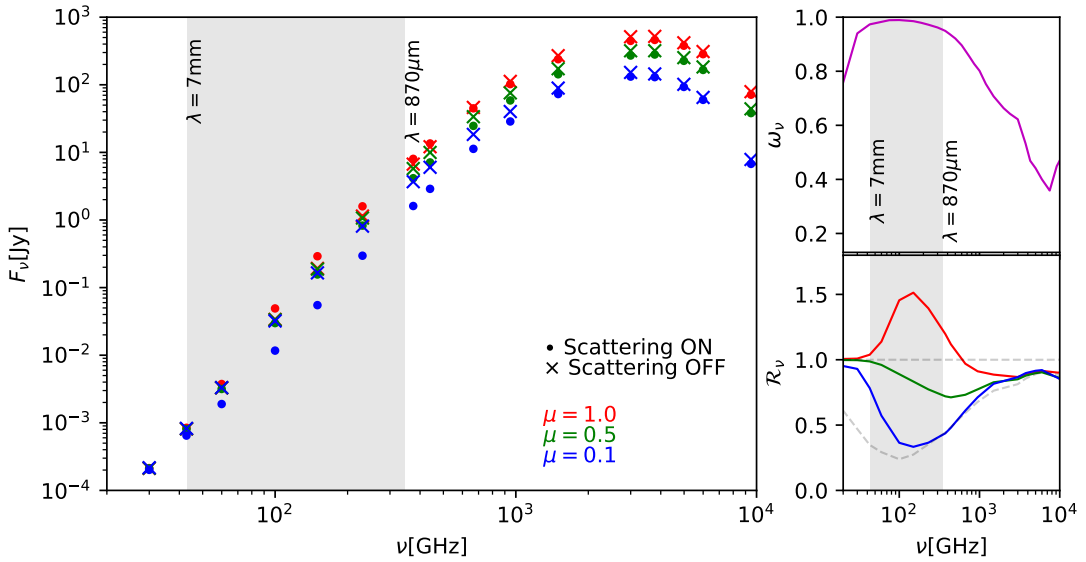


Figure 3.9: Left panel: SED for a protoplanetary disk model (see text) viewed from different line of sights, $\mu = 1.0$ (red), 0.5 (green) and 0.1 (blue). The dot and crosses are the models where the scattering is turn on and turn off, respectively. Top right panel: Albedo as a function of the frequency for a maximum grain size of 1 mm. Bottom right panel: Intensity ratios R_ν between the scattering and non-scattering fluxes for the different inclination angles. The maximum grain size of this model is set to $a_{\max} = 1$ mm in all the disk.

the sky. The color points correspond to $\mu = 1.0$ (red), $\mu = 0.5$ (green) and $\mu = 0.1$ (blue). In all the cases, the points represent the models that include scattering in the radiative transport. The crosses are the models where only the true absorption is included. The albedo properties are shown in the top right panel. The bottom right panel shows the ratio R_ν for the different inclination angles. The two reference dashed lines are: $R_\nu = 1$, and the optically thick limit (equation 3.15). A gray area between $\lambda = 870 \mu\text{m}$ and 7 mm is included for reference in all panels, where many protoplanetary disks have been observed in the last years with ALMA and VLA.

In the mm range, the ratio R_ν is larger than 1 for the face-on disk, however, R_ν decreases for higher inclination angles as the optical depth increases. This is same behavior shown in Figure (3.2), where for a constant and high albedo ω_ν , the ratio R_ν decreases from left to right as the the optical depth increases. The largest decrease of the SED with and without scattering at millimeter wavelengths occurs at the largest optical depths ($\mu = 0.1$; blue solid line in the bottom right panel).

3.4 Apparent excess emission at 7 mm

Excess emission at 7 mm has been reported in several disks around T Tauri stars (e.g. the disks around Di Cha, T Cha, Sz 32 ([Ubach et al., 2017](#))) and Herbig AeBe stars (e.g, the disks around HD 35187, HD 142666, HD 169142 ([Sandell et al., 2011](#))). In these disks, the observed intensity at 7 mm is larger than the intensity expected from an SED extrapolation using the ALMA wavelengths. The excess emission, which in some cases is a factor of 2 or larger, cannot be explained by the flux calibrator uncertainty of the VLA at 7 mm, where the flux uncertainty is $\sim 10\%$ for a single epoch observation.

Many authors have interpreted the excess emission as optically thick free-free emission from a compact ionized gas (e.g. [Macías et al. 2017](#)), free-free emission from ionized winds ([Sandell et al., 2011](#)), or emission from spinning dust ([Hoang et al., 2018](#)). The latter occurs due to the fast rotation of polycyclic aromatic hydrocarbons (PAHs) or silicate grains with sizes of some nanometers. The flux from the spinning dust emission at low frequencies ($\nu < 60$ Gz) can be one order of magnitude larger than that of the dust thermal emission for Herbig AeBe and T Tauri stars depending on the dust size distribution of these nano particles. Although this effect has not been confirmed, the existence of the nano silicate grains should also match with the presence of silicate features at smaller wavelengths ($\lambda \sim 10 \mu\text{m}$). It is not clear to the date what is the main physical mechanism that can produce the 7 mm excess.

Here, it is shown that the effect of scattering can produce an *apparent excess emission* at $\lambda = 7$ mm when interpreted as a pure absorption case. Consider a disk with mm or cm size grains, where the albedo is large at mm wavelengths ($\omega_\nu \gtrsim 0.6$). Consider further a typical case, where the disk is optically thick at ALMA wavelengths but optically thin at 7 mm observed with the VLA. In these conditions, the emergent intensity decreases at the ALMA wavelengths and increases at 7 mm compared with the pure absorption case. This combined effect could be interpreted as an excess emission at 7 mm if the ALMA emission is extrapolated to 7 mm.

The effect of the maximum grain size on the apparent excess at 7 mm can be studied based on the spectral indices in Figure (3.3) as follows: In the typical pure absorption case, the spectral indices at sub-mm and small mm wavelengths varies from $\alpha_{\lambda_1, \lambda_2}^{\text{abs}} = 2$ (at small optically thick wavelengths) to $\alpha_{\lambda_1, \lambda_2}^{\text{abs}} = 2 + \beta_{\kappa_\nu}$ (at large optically thin wavelengths); then, as $\beta_{\kappa_\nu} > 0$, the ratio $\alpha_{1.3-3.0\text{mm}}^{\text{abs}}/\alpha_{3.0-7.0\text{mm}}^{\text{abs}}$ is always less than 1. This does not always occur in the scattering case, where the

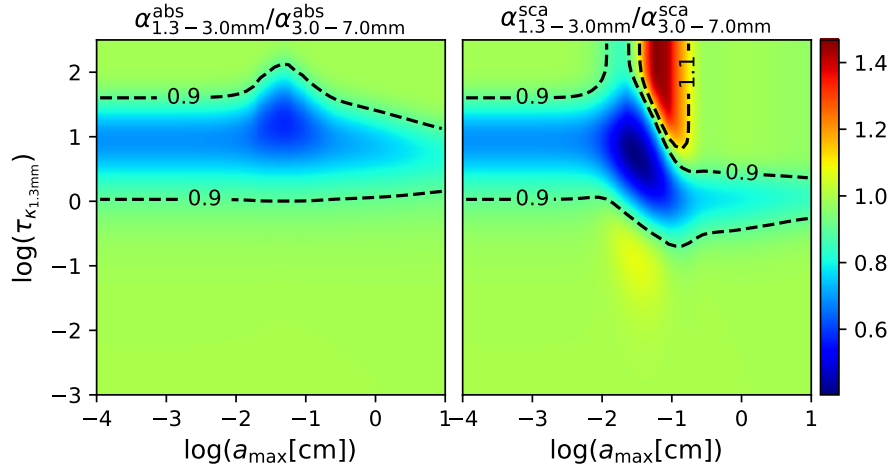


Figure 3.10: Ratio between the spectral indices in the scattering and absorption cases (see Figure 3.3) at mm wavelengths as a function of the optical depth at $\lambda = 1.3$ mm and the maximum grain size. For reference, the dashed lines show the region where the ratio is 0.9 and 1.1.

ratio $\alpha_{1.3-3.0\text{mm}}^{\text{sca}}/\alpha_{3.0-7.0\text{mm}}^{\text{sca}}$ could be larger than 1 depending on the optical depth regime and the maximum grain size.

Figure (3.10) shows the ratio between $\alpha_{1.3-3.0\text{mm}}$ and $\alpha_{3.0-7.0\text{mm}}$ in the pure absorption case (left panel) and the scattering case (right panel) as function of the optical depth at 1.3 mm and the maximum grain size. Isocontours where the ratio is 0.9 and 1.1 are shown with dashed lines, as a reference. In the absorption case, the ratio is 1 in the optically thin regime (where both spectral indices are given by $2 + \beta_\kappa$) and in the optically thick regime (where both spectral indices are 2). For intermediate optical depths, the spectral index at smaller wavelengths is smaller than at longer wavelengths, thus the ratio is always smaller than 1 as expected.

In the scattering case, the ratio is also 1 in the optically thin regime. For very optically thick disks ($\log(\tau_{\kappa_{1.3\text{mm}}}) \gtrsim 1.5$), the ratio is also 1 for very small grains (where the albedo is small) and for very large grains (where the albedo is approximately constant ($\beta_{\omega_\nu} \sim 0$) and the scattering equally affects all the wavelengths (equation 3.15)). However, the region between $-1.5 \lesssim \log(a_{\text{max}}[\text{cm}]) \lesssim -1$ and $\log(\tau_{\kappa_{1.3\text{mm}}}) \gtrsim 1$ has a ratio larger than 1. The SED of a disk with the latter properties would look anomalous and the emergent intensity at 7 mm could be interpreted as an excess emission if the scattering effects are not taken into account.

Figure (3.11) explores the effects of the scattering on the 7 mm emission interpretation for a disk with $a_{\text{max}} = 1$ mm and $\log(\tau_{\kappa_{1.3\text{mm}}}) = 1.3$ using equations (3.11) and (3.13). The SED of this disk model is shown in the left panel. The red dots are the pure absorption emission case (scattering OFF), and the blue triangles are

the scattering case (scattering ON). The black arrows show the difference between both cases. Note that the emission in all the ALMA wavelengths decreases with respect to the pure absorption case, while at VLA wavelengths the emission slightly increases by a factor of 1.1.

Then, if the millimeter emission is interpreted as a pure absorption case (which is the usual assumption in many papers) and the ALMA emission ($\nu = 100, 230, 344$ GHz) is extrapolated to smaller frequencies $\nu = 30$ and 42 GHz, the observed intensities at these longer wavelengths would seem to have an excess emission due to the combined effect of the decrease of the emission at optically thick small wavelengths and the increase of the emission at optically thin large wavelengths.

The flux calibration error at ALMA and VLA is around $\sim 10\%$. The width of the extrapolated line takes into account the propagation due to this error. Even when this uncertain is taken into account, it is not enough to explain the excess by calibration errors.

Top right panel of this Figure shows the optical depth associated to the scattering (blue triangles) and pure absorption cases (red dots). The bottom right panel shows the emission excess defined as

$$E\% = \left(\frac{I_{\nu}^{\text{sca}} - I_{\nu}^{\text{ext}}}{I_{\nu}^{\text{ext}}} \right) \times 100, \quad (3.29)$$

where I_{ν}^{ext} is the extrapolated intensity (blue crosses). The vertical error bars correspond to the uncertainties in the flux calibration in the ALMA and VLA observations. Note that at 42 GHz, the emission excess is around 70%, with a lower limit of $\sim 40\%$ and an upper limit of $\sim 100\%$.

Finally, note that, even if the 7 mm emission slightly increases in the scattering case, the main reason for the apparent 7 mm excess is the decrease of the emission at optically thick millimeter (ALMA) wavelengths due to the scattering effects. This deficit of the emission at optically thick ALMA wavelengths also lead to [Zhu et al. \(2019\)](#) to propose that the disks are more massive than expected when the observations are wrongly interpreted as a pure absorption case. They proposed that this hidden mass would make the mass of the observed disks consistent with the inferred solid mass in exoplanets.

3.5 The HL Tau disk

HL Tau is a low mass star of $1.7 M_{\odot}$ ([Pinte et al., 2016](#)) in the Taurus-Auriga star formation region at a distance of 147 pc ([Galli et al., 2018](#)). The disk around

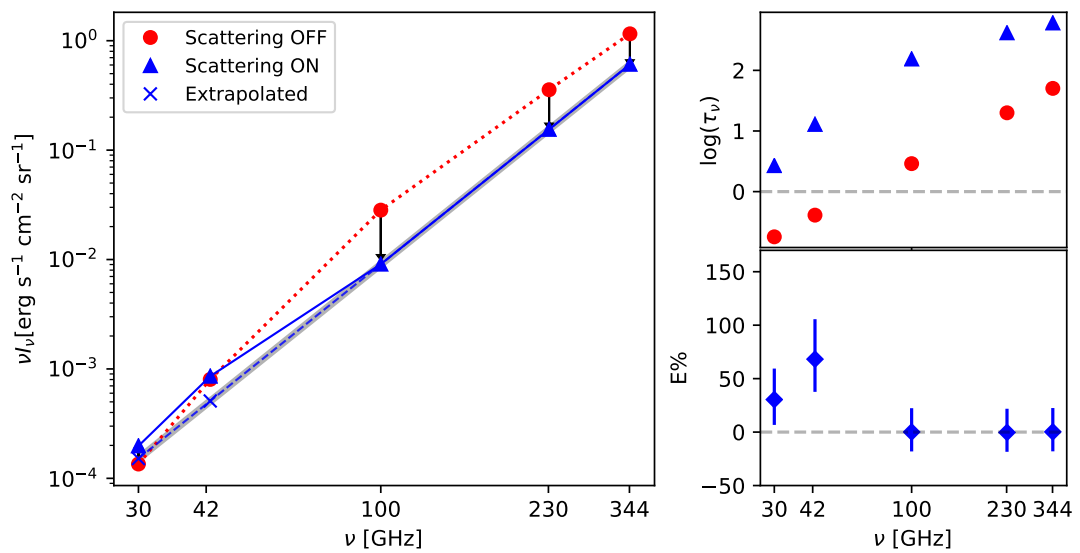


Figure 3.11: Scattering effects on the SED for a disk with maximum grain size $a_{\max} = 0.1$ cm and $\log(\tau_{\kappa_{1\text{mm}}}) = 1.3$. Left panel: SED at millimeter wavelengths for a pure absorption model (red dots) and taking into account the scattering (blue triangles). The blue crosses are the extrapolated VLA intensity using the ALMA frequencies. The width of this curve takes into account the propagation of the 10% calibration error of the ALMA observations. Top right panel: optical depths associated to the disk at different wavelengths in the scattering off (red dots) and scattering on (blue triangles) models. Bottom right panel: Excess emission at different wavelengths. The vertical error bars are the uncertainties due to the usual flux calibration error in the observations.

this young star (lifetime ~ 1 Myr, [van der Marel et al. \(2019\)](#)) has been observed with high angular resolution with ALMA and VLA, and shows multiple gaps and rings structures in the dust continuum emission. In this section, which is based on the results shown at [Carrasco-González, Sierra, et al. \(2019\)](#), a multi-wavelength analysis of this disk is done using the results from the above sections.

The radial profiles of the dust continuum observations at $\lambda = 0.87, 1.3, 2.1, 8.0$ mm (bands 7, 6, 4 and Ka+Q, respectively) with original synthesized beams of $\sim 30, 35, 49$, and 42 m.a.s., respectively, were all convolved to a common beam of 50 m.a.s. (or 7.35 au at the assumed distance). This beam was chosen because it gives the best compromise between resolution and sensitivity given the original beam sizes and rms noises.

The radial profiles (azimuthally averaged) are used to find the dust properties of the disk using the solution for the radiative transfer equation with scattering. The free parameters used to fit the equation are: the optical depth at a reference frequency, the maximum grain size (which sets the albedo and the opacity spectral index β_χ), and the dust temperature. Top panel of Figure (3.12) shows the observed radial profiles of the brightness temperature at each wavelength (see legend in the top right corner). The bottom panel shows the spectral indices between consecutive wavelengths (see legend in the top left corner). This disk does not have spectral indices below the optically thick limit $\alpha = 2$. The vertical dashed lines show the position of the gaps and rings. The notation for gaps and rings is D (dark), B (bright) respectively, followed by the position in au.

Figure (3.13) and (3.14) show the results from the fit. The first figure summarizes the observational fitted properties, and the second figure shows the physical dust properties. In Figure (3.13), the upper panel is the optical depth at different wavelengths (see legend on top right corner), middle panel is the opacity spectral index β_χ , and the bottom panel is the albedo at $\lambda = 1.3$ mm. The optical depths and the opacity spectral index are related by $\tau_\nu \propto \nu^{\beta_\chi}$ (equation 3.8). In Figure (3.14), the upper panel is the dust temperature, the middle panel is the dust surface density, and the bottom panel is the maximum grain size.

The position of several snow lines are shown as reference as vertical colored regions: blue (H_2O), red (CH_3OH , HCN), green (NH_3), and gray (CO_2). The freezing temperatures for these molecules were taken from [Zhang et al. \(2015\)](#). The gray dashed line shown in the middle panels is the column gas density (number of particles per cm^2) from [Yen et al. \(2016\)](#) derived from HCO^+ observations.

The gray dashed lines in the top and bottom panels compare the fitted dust temperature and the maximum grain size with a power-law function. The best

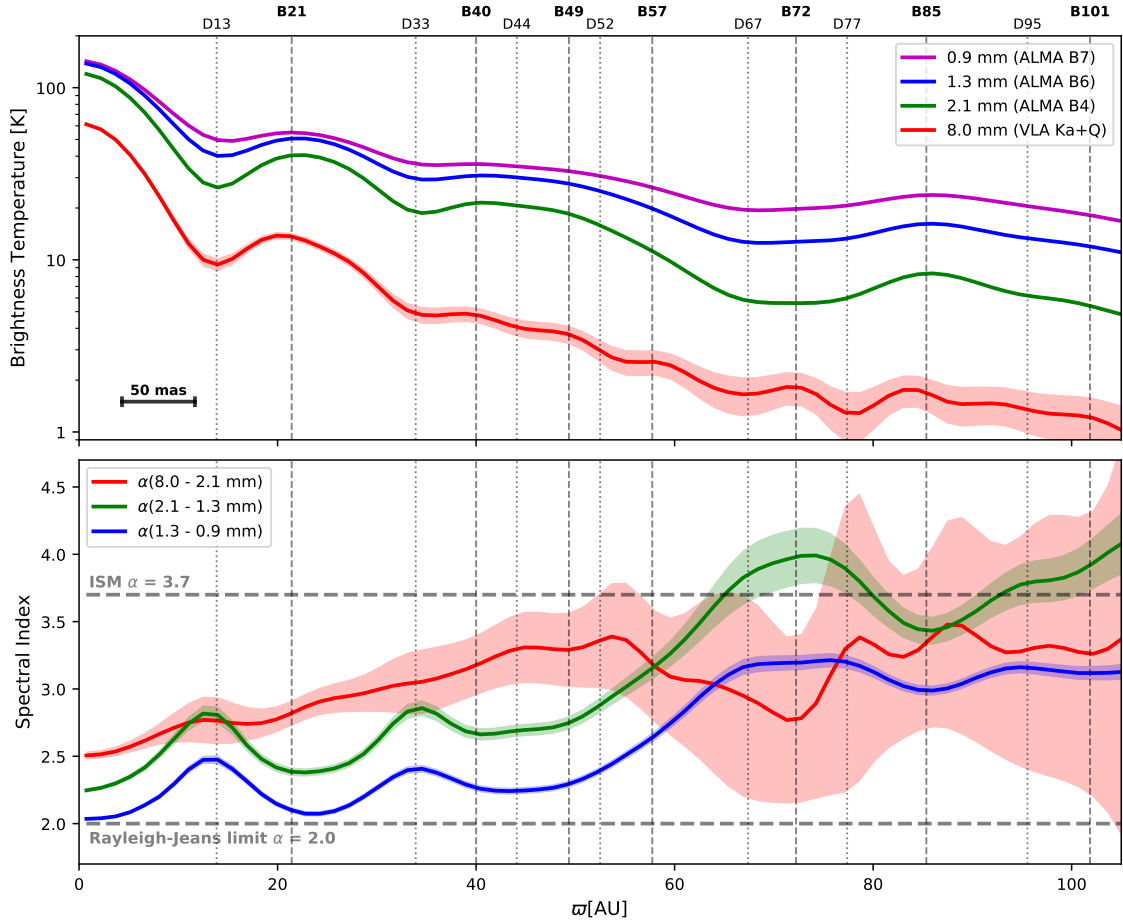


Figure 3.12: Radial profiles of the HL Tau disk. Top panel: Brightness temperature at $\lambda = 0.9, 1.3, 2.1, 8.0 for the magenta, blue, green, and red lines respectively. Bottom panel: Spectral indices between consecutive wavelengths: $0.9 - 1.3, $1.3 - 2.1, and $2.1 - 8.0 for the blue, green and red lines, respectively. The light and dark dashed lines show the position of the gaps and rings, respectively.$$$$

power-law models are $T_{\text{dust}}/\text{K} = 150(\varpi/10\text{au})^{-0.5}$ and $a_{\text{max}}/\text{mm} = 0.9(\varpi/40\text{au})^{-0.2}$.

Note the correlation between the different parameters in these plots. For example, the peaks of the optical depth correspond to peaks in the dust surface density, which also correlate with the peaks in the continuum emission. At B21, there is a small increase of the dust temperature compared with its global decrease with the disk radius. Also, the size of the dust grains has a local maximum in the inner border of B21, which could be associated to some snow line (Okuzumi et al., 2016) (see discussion below). The bright rings at B40 and B49 are separated by a distance similar to that of the beam, this is the reason why the optical depth and the dust surface density seem to have a maxima just in between these two maxima. The dust temperature and grain size do not show a maxima at this position.

At B72, the optical depth and dust surface density are also correlated, but in contrast to the inner bright rings, the grain size has a deep minima ($a_{\text{max}} \sim 500 \mu\text{m}$). Many authors have proposed the presence of a planet at this disk radius (e.g. Bae et al. 2017, Dong et al. 2018), which could be responsible for the increase of the maximum grain size at B85, where the dust grains could be accumulating due to the pressure gradients generated by the depletion of gas in the inner ring. Even when the gas observations from Yen et al. (2016) can give some idea about the origin of the bright rings in the dust continuum observations, it is not possible to give a complete and consistent description of all the bright rings and correlate them with dust trap prescriptions because the gas surface density is not well constrained due to its low angular resolution and sensitivity.

The position of the snow lines are relevant because they could be associated to local maxima and minima at different radii of the dust surface density and the maximum grain size. This occurs because the sticking efficiency of dust aggregates changes around the snow lines (Güttler et al., 2010). Dust evolution models, where the sticking and fragmentation properties change due to the sublimation or freezeout of gas volatiles on the grains surface, have demonstrated to accumulate dust grains close to the snow lines (e.g. Okuzumi et al. 2016). This scenario is probably the case for the small local changes of the dust properties in the gaps and rings in the inner disk ($\varpi < 60 \text{ au}$), where the different snow lines match with the bright and dark rings, and where the maximum grain size and dust surface density have local maxima/minima with respect to the global radial gradient. However, the outer wide gap (between D67 and D77) does not seem to be related to a snow line, and its maximum grain size is smaller than all the other gaps, suggesting that its origin is not the same. The gas and dust surface densities also have a minimum at this radius.

Note that the separation between some maxima and minima are in the order of the profiles resolution (50 mas = 7.35 au), therefore, local variations of the dust properties are actually the minimum contrast between the gaps and rings due to the smoothing/convolution effects.

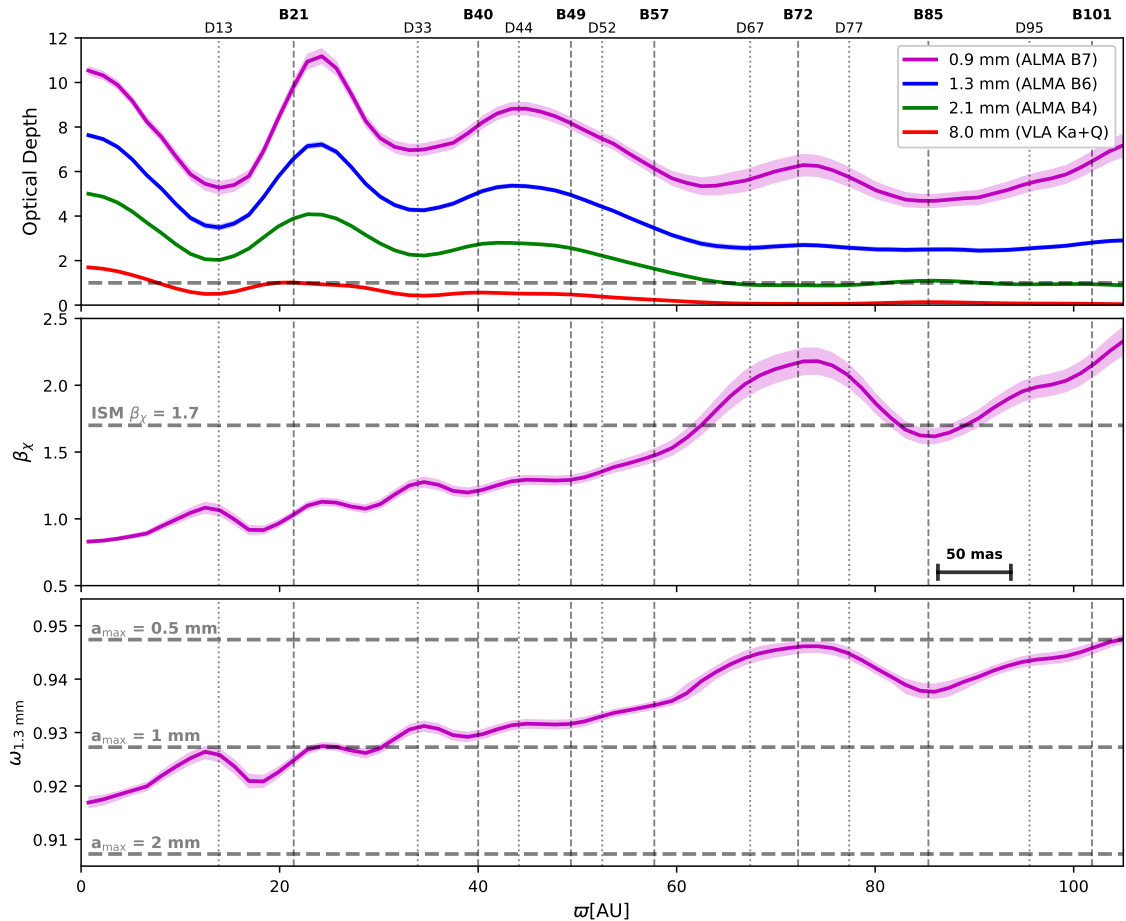


Figure 3.13: Radial fits of the HL Tau disk. Top panel: Optical depth at $\lambda = 0.9, 1.3, 2.1, 8.0$ mm for the magenta, blue, green, and red lines respectively. Middle panel: Opacity spectral index. Bottom panel: Albedo at $\lambda = 1.3$ mm.

Figure (3.15) shows a comparison between the observed brightness temperature and the best fit model. The model well reproduces the observed brightness temperature at all wavelengths. Also, a 3 mm image (ALMA Partnership et al., 2015) at lower angular resolution (80 m.a.s.) was included to test the best fit model. Even when this observation was not used to fit the model, there is also a good agreement with the brightness temperature predicted by the model.

In order to compute the depth traced by each wavelength within the disk, consider a disk in vertical hydrostatic equilibrium (see chapter 3), where the dust density

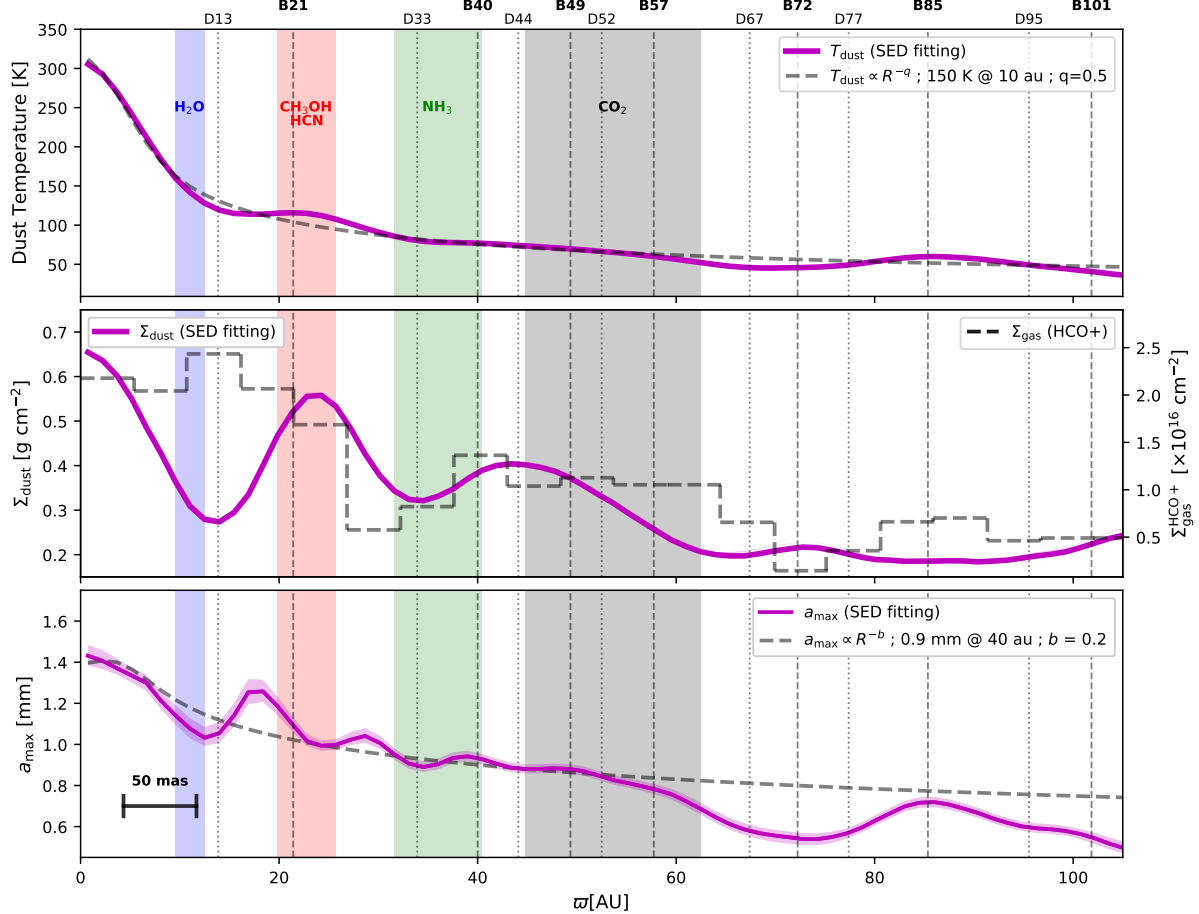


Figure 3.14: Radial fits of the HL Tau disk. Top panel: dust temperature. Middle panel: dust surface density. Bottom panel: maximum grain size. The blue, red, green, and gray vertical bands correspond to the snow line position of several molecules. The gray dashed lines in top and bottom panels are power law fits of the dust and maximum grain size, respectively. The gray dashed line in the middle panel is the column gas density from Zhang et al. (2015).

ρ_d given by

$$\rho_d = \frac{\Sigma_d}{\sqrt{2\pi}H_d} \exp \left[-\frac{1}{2} \left(\frac{z}{H_d} \right)^2 \right], \quad (3.30)$$

Σ_d is the dust surface density, H_d is the dust scale height, and z is the height above the mid plane. Then, the height z_1 where the optical depth is 1 (measured from the disk surface) can be found by

$$1 = \int_{z_1}^{\infty} \rho_d \chi_{\nu} dz. \quad (3.31)$$

The solution for z_1 from this equation is shown in Figure (3.16) for different wavelengths. Top panel shows z_1 normalized to H_d as a function of the radius at

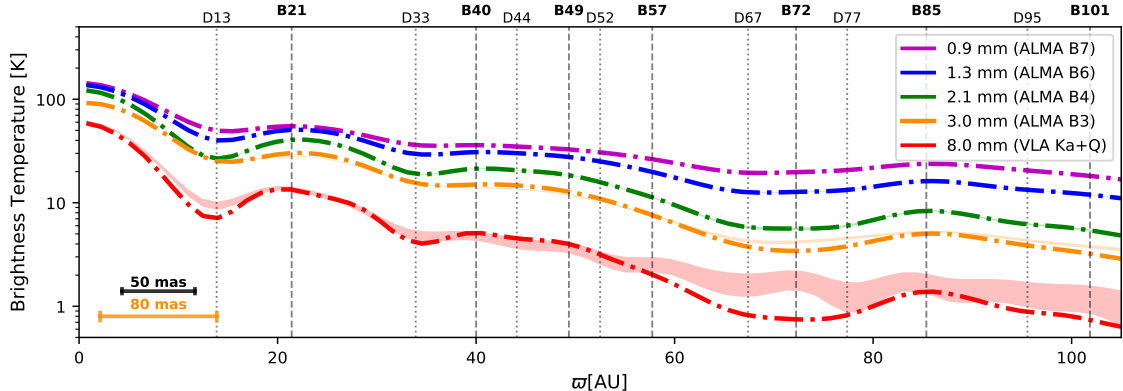


Figure 3.15: Comparison between the predicted brightness temperatures at each wavelength from the best fit model and observations. The dashed-pointed lines are the models and the shade areas are the $1-\sigma$ levels of the observed brightness temperature. Also, the lower angular resolution (80 m.a.s.) observation at $\lambda = 3$ mm (orange curves) was included and compared with the prediction from the model.

$\lambda = 0.9, 1.3$, and 2.1 mm (magenta, blue, and green line, respectively). The solution at $\lambda = 8$ mm is not shown because the disk is optically thin at this wavelength except in the most inner region ($\varpi \lesssim 7$ au). Bottom panel shows z_1 in astronomical units assuming that the dust scale height is $H_d = 0.1H_g$, where $H_g = c_s/\Omega_K$ is the gas scale height, $c_s = \sqrt{k_B T/\mu_m m_H}$ is the sound speed, k_B is the Boltzmann constant, μ_m is the mean molecular weight, m_H is the proton mass, and Ω_K is the Keplerian angular velocity around a star with a mass of $1.7 M_\odot$. The gray dashed light and dark curves show the height where the dust mass is 50, 90% of the total column mass at each radius, which corresponds to a scale height of 0.67, 1.64 H_d respectively. In this Figure, as in the previous ones, the angular resolution is 7.35 au, which is in the order of the separation between rings and gaps. Then, due to the convolution effects, the minima are actually a upper limit to the actual depths of the gaps, while the maxima are a lower limit to the actual height of the rings.

Note that the smaller the wavelength, the larger the height where the optical depth is unity, as expected. The smaller wavelength (ALMA Band 7) only traces the disk surface ($z > H_d$) in the rings (B21, B40, B49), but the rest of the wavelengths can penetrate within one dust scale height. In the gaps (D13, D33), all the wavelengths reach a region below one dust scale height. In the outer disk (B57 and beyond), where the dust surface density is smaller than in the inner disk, all the wavelengths also trace a region below one scale height.

These solutions assume a vertically isothermal disk and the same maximum grain size above the mid plane. A possible future improvement to these results could be to include the effects of sedimentation and temperature.

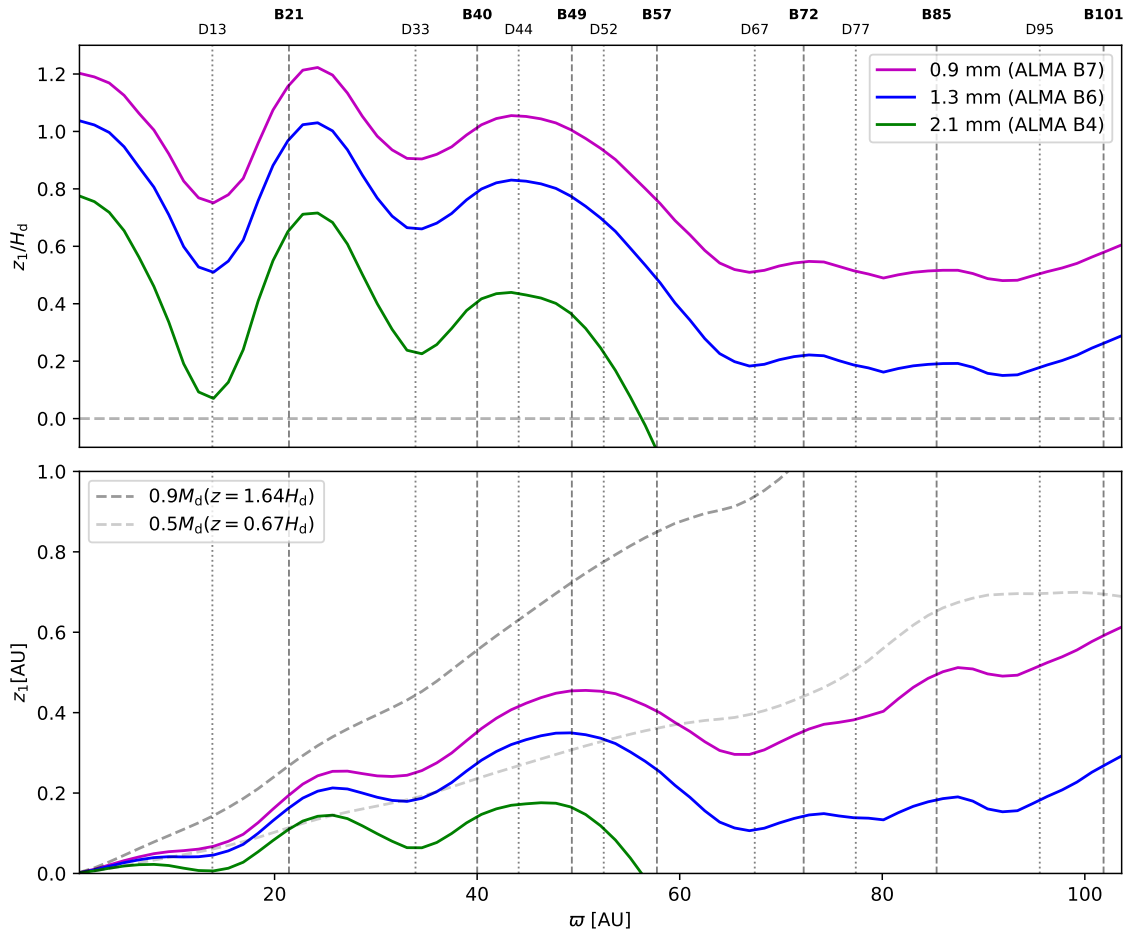


Figure 3.16: Height z_1 where $\tau_\nu = 1$ at $\lambda = 0.9, 1.3, 2.1$ mm for the magenta, blue, and green line respectively. Top panel: z_1 normalized to the dust scale height. Bottom panel: z_1 in astronomical units assuming $H_d = 0.1H_g$. The gray dashed light and dark lines are the height where the dust mass is 50, 90 % of the total at each radius respectively.

Chapter 4

Gas and dust dynamics

Planets form inside protoplanetary disks due to the evolution and growth of the dust grains. It is well known that the dust particles settle to the mid plane of the disks due to the vertical component of the stellar gravity (Armitage, 2010), during this process these grains can grow and reach sizes of some millimeters depending on the disk properties. The sedimentation of all the dust particles exactly to the mid plane is only prevented by the vertical turbulence of the gas disk, which eventually creates a thinner dust disk compared with the gas disk (Dubrulle et al., 1995). If the self-gravity of the disk is neglected, the only force acting on the dust disk is the gravity of the central star; however, the forces acting on the gas disk are the stellar gravity and the gas pressure gradients. This difference induces a shear velocity between both components and an angular momentum interchange, which is the responsible of the radial motions of the dust particles (e.g. Takeuchi & Lin 2002, Weidenschilling 1977).

The dust particles move very fast toward the star for typical disk properties. The accretion time for a centimeter dust particle can be estimated from $t_{\text{acc}} \sim \varpi/v_\varpi$, where ϖ , v_ϖ are disk radii and radial velocity, respectively. The radial dust velocity is completely derived below (equation 4.19), and can be shown that $t_{\text{acc}} \sim (\text{St} + \text{St}^{-1})/(\eta\Omega_K)$, where St is the Stokes number (equation 4.25) and η is a factor that modifies the gas disk rotation from the Keplerian angular rotation Ω_K . This factor is defined in equation (4.9) and it can be approximated to the square of the aspect ratio of the disk (i.e. the ratio between the height and the radius of the disk), with a typically value of ~ 0.1 , such that $\eta \sim 10^{-2}$. Then, the accretion time is around $t_{\text{acc}} \sim 2 \times 10^4$ years for a centimeter dust grain within a disk with a gas surface density $\Sigma_g = 60 \text{ g/cm}^2$ at 20 au¹, or $t_{\text{acc}} \sim 4 \times 10^4$ at 100 au if the gas surface density linearly decreases with the disk radius.

¹Reference numbers taken from the HL Tau disk properties in the above chapter.

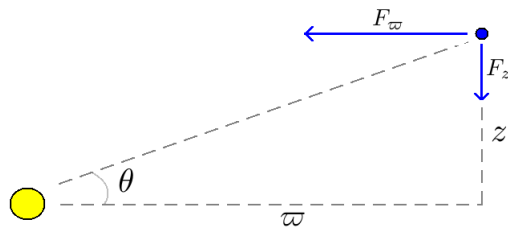


Figure 4.1: The radial and vertical gravitational force due to the star at a height z above the mid plane and at a radial distance ϖ .

Whatever the case, the accretion time is very low compared with the typical lifetime of the disk ($\sim 10^6$ years). The migration could be prevented if the dust to gas mass ratio increases, since the inertia of the dust becomes important compared with the gas inertia; however, in the typical dust-to-gas mass ratio $\sim 1/100$, the gas dynamics dominates.

Even if the radial migration of dust particles is prevented, it is not clear which mechanisms can prevent the fragmentation of large bodies when they collide; for example Brauer et al. (2008) determined that the particles cannot grow to sizes larger than millimeters throughout the disk if the threshold of the velocity fragmentation is in the order of some meters per second. These problems are known as the *growth barrier* and they are still an open question in the theoretical understanding of the planet formation theory.

Despite the theoretical impediments, there is observational evidence of planetesimals (e.g. Matthews et al. 2010) and of centimeter-millimeter sized particles on protoplanetary disks (e.g. Testi et al. 2003, Rodmann et al. 2006, Wilner et al. 2005, Natta et al. 2007).

In this chapter, the gas and dust dynamics are described respectively in the following two sections. These two sections are the basis for understanding the theory the dust trapping models (radial and azimuthal) presented in the rest of this chapter.

4.1 Gas dynamics

Consider a gas test particle located at a radial distance ϖ from the center of the star and at a distance z above the mid-plane of the disk as shown in Figure (4.1). For a fixed radial distance ϖ , the gravitational force in the radial axis decreases when z increases due to the distance from the star to the test particle increases and because the radial component of the force (F_ϖ) decreases when the angle θ increases. So, the test particle rotates at a lower angular velocity around the star at a given radius when the distance z increases.

The gravitational forces of the star acting on the test particle in the vertical (F_z) and radial direction (F_ϖ) are

$$F_z = -\frac{GM_*}{(\varpi^2 + z^2)} \sin \theta = -\frac{GM_*}{(\varpi^2 + z^2)^{3/2}} z, \quad (4.1)$$

$$F_\varpi = -\frac{GM_*}{(\varpi^2 + z^2)} \cos \theta = -\frac{GM_*}{(\varpi^2 + z^2)^{3/2}} \varpi. \quad (4.2)$$

These are the formal equations at any height above the mid plane, however, as the height of the disk tends to be much smaller than the disk radius, from now on, we focus on the mid plane ($z = 0$) dynamics.

If the mass of the disk is small compared with that of the star, the self-gravity of the disk can be ignored. Then, the equilibrium of forces in the radial and vertical direction are

$$0 = \Omega_g^2 \varpi - \Omega_K^2 \varpi - \frac{1}{\rho_g} \frac{\partial P}{\partial \varpi} + \text{dust-gas interactions} \quad (4.3)$$

$$0 = -\Omega_K^2 z - \frac{1}{\rho_g} \frac{\partial P}{\partial z}. \quad (4.4)$$

where

$$\Omega_K^2 = \frac{GM_*}{\varpi^3}, \quad (4.5)$$

is the Keplerian angular velocity, Ω_g is the gas angular velocity, P is the gas pressure, and ρ_g is the gas density. The third term of equation (4.3) is the gas pressure force on itself.

Assuming that the disk is isothermal in the vertical direction $P = c_s^2 \rho_g$, where c_s is the sound speed. The solution of the gas density from equation (4.4) is given by

$$\rho_g = \rho_0 \exp \left(-\frac{z^2}{2H_g^2} \right), \quad (4.6)$$

where ρ_0 is the gas surface density in the mid plane, and the gas scale height H_g is related with the sound speed and the angular velocity in the mid plane by

$$H_g = \frac{c_s}{\Omega_K}. \quad (4.7)$$

In the horizontal direction, equation (4.3) can be solved if the dust-gas interactions are neglected. This assumption is usually true because the gas mass tends to be much larger than the dust mass, then, the gas dynamics is not modified by the dust dynamics. This assumption is not true for disks with high dust-to-gas mass

ratio. Then, the solution for small dust-to-gas mass ratios is given by

$$\Omega_g = \Omega_K [1 - \eta]^{1/2}, \quad (4.8)$$

where

$$\eta = -\frac{1}{\Omega_K^2 \rho_g \varpi} \frac{\partial P}{\partial \varpi} \quad (4.9)$$

is the factor that modifies the gas angular velocity from the Keplerian angular velocity. As the pressure depends on the temperature and gas density and both tend to decrease with the disk radius, then $\eta > 0$ and the gas disk becomes sub-Keplerian. However, if the pressure increases with the radius (e.g. in gas rings), the gas disk becomes super-Keplerian.

4.2 Dust dynamics

The dust grains follow the same equations of motion than the gas but without the forces from the pressure gradients. Note from equation (4.3) that if $P = 0$, then the dust angular velocity tends to the Keplerian angular velocity. However, the dust-gas interactions modify their angular velocity from the pure Keplerian rotation. This interaction between gas and dust is the responsible of the dust grain migration in the disks (see detailed derivation below).

A dust grain feels a drag force due to the collisions with the gas molecules because of the relative velocity between gas and dust is not zero. The drag force depends of the size of the dust particle (a) compared with the mean free path of the gas (λ_{mfp}); if $a < \lambda_{\text{mfp}}$ the gas is described as individual molecules with a typical thermal speed (v_{th}) given by their Maxwellian distribution, this is called the Epstein regime. But if $a > \lambda_{\text{mfp}}$, the gas molecules are described as a fluid around an obstruction, and it is called the Stokes regime. In both cases, the friction force is proportional to the cross area.

In the Epstein regime, the drag force can be derived from the frequency of collisions of the dust particle with the gas molecules. If a spherical dust particle with size a moves with a speed v relative to the gas, which has a thermal speed v_{th} , the front cross section area (that normal to the velocity vector \vec{v}) collides with a larger number of molecules than in the back cross section area (see Figure 4.2).

If the dust collides with N_1 molecules in a time τ , the frequency of collisions in the front side is

$$f^{\text{front}} = \frac{N_1}{\tau}. \quad (4.10)$$

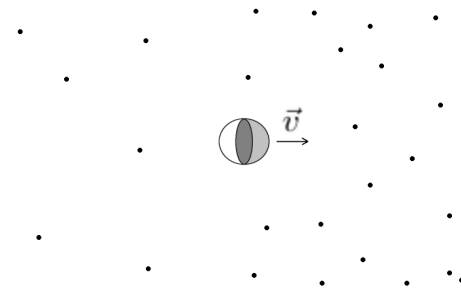


Figure 4.2: A dust particle with radius s moving through a medium with constant density. The collisions in the direction of motion of the grain is larger than in the back side.

The number of colliders within the swept volume V_1 is a fraction of the total colliders (N) inside a volume V , such that $N_1 = (V_1/V)N = V_1n$, where n is the number density of molecules in the gas. The swept volume corresponds to a cylinder with radius a and length $l = v_{\text{rel}}\tau$, where v_{rel} is the relative impact speed of the grain with respect to the gas, and τ the time needed to travel a distance l . Then, the frequency of collisions can be written as

$$f^{\text{front}} = \frac{\pi a^2 l n}{\tau} = \pi a^2 (v_{\text{th}} + v) \frac{\rho_g}{\mu_m m_H}, \quad (4.11)$$

where $v_{\text{th}} + v$ is the relative impact velocity. From the same arguments, the frequency of collisions in the back side is

$$f^{\text{back}} = \pi a^2 (v_{\text{th}} - v) \frac{\rho_g}{\mu_m m_H}, \quad (4.12)$$

where f^{back} cannot be smaller than 0. The critical point occurs when $v = v_{\text{th}}$, where the speed of the dust is high enough that there are not collisions in the back side; if $v > v_{\text{th}}$, then $f^{\text{back}} = 0$.

If it is assumed that the magnitude of the momentum of the molecules does not change after the collisions (only their direction) i.e. the gas does not increase its temperature, the change of the momentum of the dust grain is $\Delta p_d = -2\mu_m m_H v_{\text{th}}$; and the net force that the dust particle “feels” is

$$F_D = \Delta p_d (f^{\text{front}} - f^{\text{back}}) = -4\pi a^2 \rho_g v_{\text{th}} v. \quad (4.13)$$

A more rigorous analysis, where one considers that not all the collisions are parallel to the velocity vector, introduces a factor of $1/3$. Thus, in the vector form,

$$\vec{F}_D = -\frac{4\pi}{3} \rho_g a^2 v_{\text{th}} \vec{v} = -\frac{m \vec{v}}{\tau_{\text{fric}}}, \quad (4.14)$$

where τ_{fric} is the time scale of the drag force acting on a particle of material density $\rho_m = m/(\frac{4\pi}{3}a^3)$, and defined as

$$\tau_{\text{fric}} = \frac{\rho_m}{\rho_g} \left(\frac{a}{v_{\text{th}}} \right). \quad (4.15)$$

In the Stokes regime, the drag force is given by

$$\vec{F}_D = -\frac{C_D}{2} \pi a^2 \rho_g v_{\text{th}} \vec{v}, \quad (4.16)$$

where C_D is a coefficient that depends of the Reynolds number ([Weidenschilling 1977](#)). For typical dust disk properties, the mean free path can be estimated by $\lambda_{\text{mfp}} \sim 1/(\sigma_c n_d)$, where n_d is the number density of molecules with cross-section σ_c . [Armitage \(2007\)](#) determined that the mean free path in the mid plane of a disk at 1 au is around $\lambda_{\text{mfp}} \sim 2.5$ cm. At a larger radius (or above the mid plane), where the gas density decreases, the mean free path increases, then, the Epstein regime is a good approximation for millimeter or centimeter dust grains. From now on, the thermal velocity is characterized by the sound speed $v_{\text{th}} = c_s$.

4.2.1 Dust radial migration

As discussed above, the dust particles only feel the gravitational effect of the star and the drag force, so they tend to rotate with the local Keplerian angular velocity. However, the gas rotates sub-Keplerian or super-Keplerian (depending on the local pressure gradients), creating a difference in the angular velocity and an angular momentum interchange between the gas and dust.

The equations of motion of the dust in the radial and angular coordinates respectively are

$$\frac{dv_{\varpi}}{dt} = \Omega_d^2 \varpi - \Omega_K^2 \varpi - \frac{1}{\tau_{\text{fric}}} (v_{\varpi} - u_{\varpi}), \quad (4.17)$$

$$\frac{d(\varpi^2 \Omega_d)}{dt} = -\varpi \frac{(v_{\phi} - u_{\phi})}{\tau_{\text{fric}}}; \quad (4.18)$$

where $\vec{v} = (v_{\varpi}, v_{\phi}, v_z)$ and $\vec{u} = (v_{\varpi}, u_{\phi}, u_z)$ are the velocities for the dust and gas respectively in cylindrical coordinates, Ω_d is the dust angular velocity, and Ω_K is the Keplerian angular velocity. Equation (4.17) is the Newton's second law, and equation (4.18) is the angular momentum evolution due to the torque generated by the interaction with the gas. The first term of the right hand of the Newton's equation is the centrifugal acceleration of the dust, the second term is the gravitational force due to the star and the third one is the drag force in the radial coordinate.

One can merge these two equations in order to obtain the radial velocity of the dust particles ([Takeuchi & Lin, 2002](#)), obtaining

$$v_{\varpi} = \left[\frac{\text{St}^{-1} u_{\varpi} - \eta v_K}{\text{St}^{-1} + \text{St}} \right], \quad (4.19)$$

where St is the Stokes number defined by $\text{St} = \Omega_g \tau_{\text{fric}}$, and $v_K = \Omega_K \varpi$ is the Keplerian velocity. In the limit of small ($\text{St} \ll 1$) and large ($\text{St} \gg 1$) particles, the radial velocity of the dust can be approximated as

$$v_{\varpi} = \begin{cases} u_{\varpi} - \text{St} \eta v_K & \text{if } \text{St} \ll 1 \\ -\text{St}^{-1} \eta v_K & \text{if } \text{St} \gg 1. \end{cases} \quad (4.20)$$

The size of the grain by itself does not determine the value of St , it also depends on the location of the dust particle in the disk, though Ω_g and ρ_g . The “coupling” of the dust particles depends on the value of the Stokes number. The radial velocity for the small particles ($\text{St} \ll 1$) is a function of the gas velocity; but for the large particles ($\text{St} \gg 1$), it is independent of the gas velocity. Both regimes of equation (4.20) can be explained as follows:

The large dust particles ($\text{St} \gg 1$) move around the star with a Keplerian velocity because their dynamics are decoupled; the angular momentum is interchanged due to this velocity difference. Note from equation (4.20) that the larger the Stokes number, the smaller the radial dust velocity; then, those particles with a very large Stokes number do not radially migrate. However, dust particles with Stokes number around unity ($\text{St} \gtrsim 1$), the radial migration is not neglected. If locally, the dust grains with Stokes number around unity rotate faster than the gas molecules (sub-Keplerian gas; $\eta > 0$), they loose angular momentum and move radially inward; but if they rotate slower than the gas (super-Keplerian gas; $\eta < 0$) they gain angular momentum and move radially outward.

On the other side, the small particles ($\text{St} \ll 1$) are well coupled to the gas and they rotate approximately with the same gas speed. In the places where the gas is sub-Keplerian, their centrifugal force is not enough to balance the gravitational attraction, so they move radially inward. In the places where the gas velocity is larger than the local Keplerian velocity, the dust moves radially outward relative to the gas motion, but its velocity relative to the star depends of the magnitude of η and the gas radial velocity.

The ratio $f(\text{St})$ between the radial velocity (equation 4.19) and the radial velocity

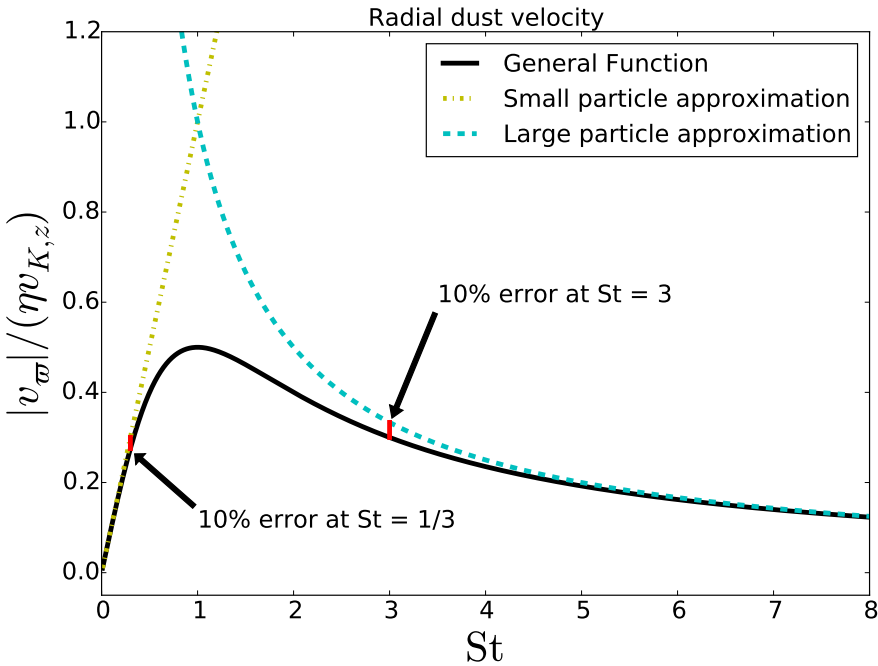


Figure 4.3: Radial dust velocity. The black solid line is the radial dust velocity as a function of St . The dot-dashed yellow line is the approximation for small particles, and the dashed cyan line is the approximation for large particles. We set $u_\omega = 0$ as an illustrative case.

approximation for small particles (equation 4.20) is given by

$$f(St) = \frac{St^{-1}}{St^{-1} + St}. \quad (4.21)$$

The approximation of the radial velocity for small particles within an error of 10% is good for $St < 1/3$. Using the same criterion, the approximation for large particles is good for $St > 3$. For $1/3 < St < 3$, equation (4.19) for v_ω has to be used. The regimes of these approximations can be seen in Figure (4.3), where we assume $u_\omega = 0$ as an illustrative case.

4.3 Dust trapping

In the last few years, high quality (sub)mm observations of disks at high angular resolution have shown that a significant fraction of them hosts one or more concentric rings and gaps (e.g. [ALMA Partnership et al. \(2015\)](#), [Andrews et al. \(2018\)](#)). These radial structures have been seen in both, the gas and the dust (e.g. [Isella et al. \(2016\)](#)). Although their origin is still under debate, these structures must have a strong impact on the evolution of the dust and gas. Ultimately, understanding this

evolution is fundamental to figure out how the formation of planetary systems takes place.

As discussed in the previous section, dust grains migrate radially in protoplanetary disks due to the angular momentum interchange between dust and gas. The dust radial velocity is proportional to the radial pressure gradient (equation 4.19). Small dust grains ($\sim \mu\text{m}$) are well coupled with the gas, and large grains ($\sim 1 \text{ mm}, \text{cm}$) feel a strong drag force and are expected to migrate to the star in a timescale much less than the lifetime of the gaseous disk, this problem is known as the radial drift barrier, first discussed by [Weidenschilling \(1977\)](#).

However, if the gas pressure has local maxima, as in the case of vortices (e.g., [Barge & Sommeria \(1995\)](#)) or rings (e.g., [Pinilla et al. \(2012\)](#), [Carrasco-González, Sierra, et al. \(2019\)](#)), the dust grains could be trapped, avoiding or retarding their accretion toward the star, and creating the appropriated conditions to build planetesimals. In the following sections, analytical models of the radial and azimuthal dust trapping are described.

4.4 Radial dust trapping

This section studies from an analytic point of view how the dust grains could be trapped in axisymmetric rings where the gas pressure has local maxima, and apply this model to the disk around HD 169142. In this approach, the dust grains radially migrate toward the pressure maxima and reach an equilibrium with the turbulent mixing which depends on the grain size, but they do not grow. The creation of the gas gaps is not addressed (which in turns creates the gas pressure maxima), but we are only interested in the redistribution of dust grains given the gas surface properties, i.e., the dust dynamics is only influenced by the drag force and turbulent mixing. Possible gravitational interactions with planets within the gaps are also ignored.

This model is similar to work done by [Birnstiel et al. \(2013\)](#) in the azimuthal coordinate for grain sizes with the same Stokes number. However, here we also include the effects of the particle size distribution on the total dust properties and the changes of the Stokes number as a function of the local gas properties in the disk.

Section (4.4.1) describes the analytical model of dust concentration within the gas pressure maxima based on the dust dynamics within protoplanetary disks. Section (4.4.2) tests the analytical dust model by comparing it with recent dust and gas disk simulations. This model is then used to describe the dust emission of the disk

around the HD 169142 star (Section 4.4.3).

4.4.1 Analytical model

Dust grains can be described as a pressure-less fluid, so their evolution in a thin disk can be followed by the advection-diffusion equation

$$\frac{\partial \Sigma_d}{\partial t} = \nabla \cdot (\Sigma_d \vec{v}) - \nabla \cdot \left[D \Sigma_g \nabla \left(\frac{\Sigma_d}{\Sigma_g} \right) \right], \quad (4.22)$$

where D {cm²s⁻¹} is the dust diffusion coefficient, Σ_d and Σ_g are the dust and gas surface densities, respectively, and $\vec{v} = (v_\varpi, v_\phi)$ is the dust velocity in cylindrical coordinates (ϖ, ϕ). A steady state solution can be reached if the flux of dust grains toward pressure maxima is balanced by diffusion, in contrast with disks where the pressure monotonically decreases with the radius and where the dust grains always migrate radially inward. In an axisymmetric disk with local pressure maxima, the steady state solution of equation (4.22) is given by

$$0 = \Sigma_d v_\varpi - D \Sigma_g \frac{d}{d\varpi} \left(\frac{\Sigma_d}{\Sigma_g} \right). \quad (4.23)$$

This equation assumes that the dust follows the gas, i.e., that there is not back reaction of the dust on the gas. This effect can be neglected if the dust-to-gas mass ratio is less than 1 (e.g., Taki et al. (2016)).

In the Epstein regime, the radial dust velocity is given by equation (4.19), which can be rewritten in terms of the pressure gradient (equation 4.9) as

$$v_\varpi = \left(\frac{\text{St}}{1 + \text{St}^2} \right) \frac{1}{\Omega_K \Sigma_g} \frac{dP}{d\varpi}, \quad (4.24)$$

where

$$\text{St} = \frac{\pi \rho_m a}{2 \Sigma_g}, \quad (4.25)$$

is the Stokes number of a dust grain with radius a and material density ρ_m , and $P = \Sigma_g c_s^2 / (\sqrt{2\pi} H_g)$ is the gas pressure. Assuming that the dust diffusion coefficient is $D = D_g / (1 + \text{St}^2)$ (Youdin & Lithwick, 2007), where $D_g = \alpha_t c_s^2 / \Omega_K$ is the gas diffusion coefficient and α_t the viscosity coefficient, then, equation (4.23) can be written as

$$0 = \frac{d}{d\varpi} \left(\frac{\Sigma_d}{\Sigma_g} \right) - \frac{\text{St}}{\alpha_t c_s^2 \Sigma_g} \frac{dP}{d\varpi} \left(\frac{\Sigma_d}{\Sigma_g} \right). \quad (4.26)$$

Neglecting the thermal gradients with respect to the density gradients,² the solution of the above equation is

$$\frac{\Sigma_d(\varpi)}{\Sigma_g(\varpi)} = \frac{\Sigma_d(\varpi_0)}{\Sigma_g(\varpi_0)} \exp \left[\int_{\varpi_0}^{\varpi} \frac{St}{\alpha_t} \frac{d \ln(\Sigma_g)}{d\varpi} d\varpi \right], \quad (4.27)$$

where $\Sigma_d(\varpi_0), \Sigma_g(\varpi_0)$ are the dust and gas densities at a reference radius ϖ_0 . Finally, the dust surface density can be written as

$$\Sigma_d(\varpi, a) = \epsilon_0 \Sigma_g(\varpi) \exp[-ka], \quad (4.28)$$

where

$$k = \frac{\pi \rho_m}{2\alpha_t} \left(\frac{1}{\Sigma_g(\varpi)} - \frac{1}{\Sigma_g(\varpi_0)} \right), \quad (4.29)$$

and ϵ_0 is the dust-to-gas mass ratio at the reference radius ϖ_0 . Figure (4.4) shows the normalized dust surface density for grains of different sizes $a[\text{cm}] = 10^{-4}, 10^{-3}, 10^{-2}, 10^{-1}, 10^0$, $\alpha_t = 10^{-2}$, and a gas surface density with two local maxima at $\varpi = 24$ au and 60 au (black dashed line). This profile corresponds to the gas surface density profile of HD 169142 discussed in Section (4.4.3.1) below. Note that the largest dust grains are more concentrated around the first maxima. As the radii of the grains decrease, the dust particles tend to be well mixed with the gas. The grains with a size smaller than 10^{-3} cm (yellow dashed line) trace the gas surface density.

Equation (4.28) can also be written as

$$\epsilon(\varpi, a)/\epsilon_0 \propto \exp[-1/\Sigma_g(\varpi)], \quad (4.30)$$

where $\epsilon(\varpi, a)$ is the local dust-to-gas mass ratio. Therefore the local dust to gas mass ratio follows the gas extrema (maxima or minima). Equation (4.28) also predicts that the gaps in the dust surface density are deeper than in the gas surface density. Note that, because the dust mass is conserved, the dust maxima are enhanced due to the redistribution of the dust grains.

The total dust surface density is given by the sum of the dust densities for each grain size. For a particle size distribution $n(a)da \propto a^{-p}da$ with minimum and maximum grain sizes, a_{\min} and a_{\max} , respectively, the total dust surface density is

$$\Sigma_d(\varpi) = \frac{\int_{a_{\min}}^{a_{\max}} \Sigma_d(\varpi, a) a^3 n(a) da}{\int_{a_{\min}}^{a_{\max}} a^3 n(a) da}. \quad (4.31)$$

²For typical sound speed and gas surface density gradients, $d \ln c_2^2/d\varpi \sim -1/2$ and $d \ln \Sigma_g/d\varpi \sim -1$, there would be a correction term of $3/2$ in front of the second term in eq. (4.26). However, for a disk with gaps, the difference tends to be larger $|d \ln \Sigma_g/d\varpi| \gg |d \ln c_2^2/d\varpi|$.

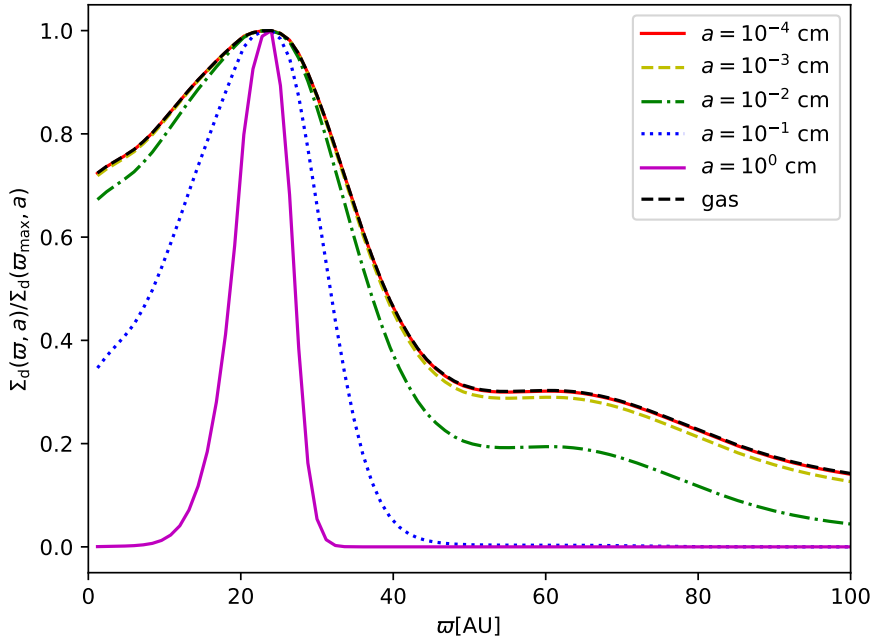


Figure 4.4: Normalized dust surface density for grains of different sizes.

In this equation, the factor $a^3 n(a) da$ weights the amount of mass associated to each dust grain size, which is assumed to be constant because the dust grains are only redistributed in the disk without coagulation or fragmentation. In addition, the redistribution of the dust grains is taken into account by the factor $\Sigma_d(\varpi, a)$, which includes the dust size differential migration, see Figure (4.4)³. Thus, the integral can be computed using the global values of the disk (a_{\max}, p).

In particular, if the original value of the particle size distribution is $p = 3.5$ and $a_{\max} \gg a_{\min}$, the integral is

$$\Sigma_d(\varpi) = \frac{\epsilon_0 \Sigma_g}{2\sqrt{ka_{\max}}} \operatorname{erf}(\sqrt{ka_{\max}}), \quad (4.32)$$

where erf is the error function. Furthermore, ϵ_0 is constrained by the total dust mass in the disk. If ϵ_{global} is the global dust-to-gas mass ratio (typically $\sim 1/100$), then

$$\epsilon_{\text{global}} = \frac{\int_A \Sigma_d(\varpi) dA}{\int_A \Sigma_g(\varpi) dA} = \frac{\int_A \Sigma_d(\varpi) dA}{M_g}, \quad (4.33)$$

³The local changes in the particle size distribution are discussed in Section (4.4.3.5).

where M_g is the total gas mass. Therefore, using Equation (4.32) one obtains

$$\epsilon_0 = \epsilon_{\text{global}} M_g \left[\pi \int_0^R \frac{\Sigma_g(\varpi) \operatorname{erf}(\sqrt{ka_{\max}})}{\sqrt{ka_{\max}}} \varpi d\varpi \right]^{-1}, \quad (4.34)$$

where R is the disk radius. Finally, replacing equation (4.34) in equation (4.32) one obtains the total dust surface density as a function of the gas surface density, the maximum grain size and the global dust-to-gas mass ratio as

$$\Sigma_d(\varpi) = \frac{\epsilon_{\text{global}} M_g}{2\pi} \left[\frac{\Sigma_g \operatorname{erf}(\sqrt{ka_{\max}}) / \sqrt{ka_{\max}}}{\int_0^R \Sigma_g \operatorname{erf}(\sqrt{ka_{\max}}) / \sqrt{ka_{\max}} \varpi d\varpi} \right]. \quad (4.35)$$

This equation gives the dust surface density when the gas surface density in axisymmetric rings is known. Since the gas surface density evolves in a diffusion timescale which is much longer than the advection timescale of the dust (see Appendix B), the dust will always concentrate following the gas maxima.

Dullemond et al. (2018) proposed a dust model that assumes that the gas pressure maxima are given by gaussian functions. To obtain the dust surface density of grains with a single size, they assume locally a maximum gas surface density given by the Toomre stability criterion. Instead, our model uses a gas profile that can be obtained from observations or simulations. Given this profile, it predicts the total dust surface density taking into account the differential concentration of all grain sizes.

4.4.2 Application of the model to a numerical simulation

Flock et al. (2015), Ruge et al. (2016) performed non-ideal 3D magneto-hydrodynamical simulations of a protoplanetary disk where they followed the dynamics of dust particles of different sizes. As expected, they found that the largest grains tend to be more concentrated around the pressure maxima. This section compares the dust surface density from the simulation for each grain size with that predicted by our analytic dust model (equation 4.28). Then, the gas surface density that appears in the dust model equation is given by the azimuthally averaged gas density profile from the simulation.

A snapshot of the simulation at a time of 400 inner orbits of the disk is chosen. At this time the gas surface density has developed a ring structure without vortices⁴, and the dust grains have had enough time to concentrate in the ring following the drag force of the gas. The gas density profile has a local maximum (ring) centered

⁴The azimuthal fluctuations of the gas surface density in the ring with respect to the azimuthal average are smaller than 6%.

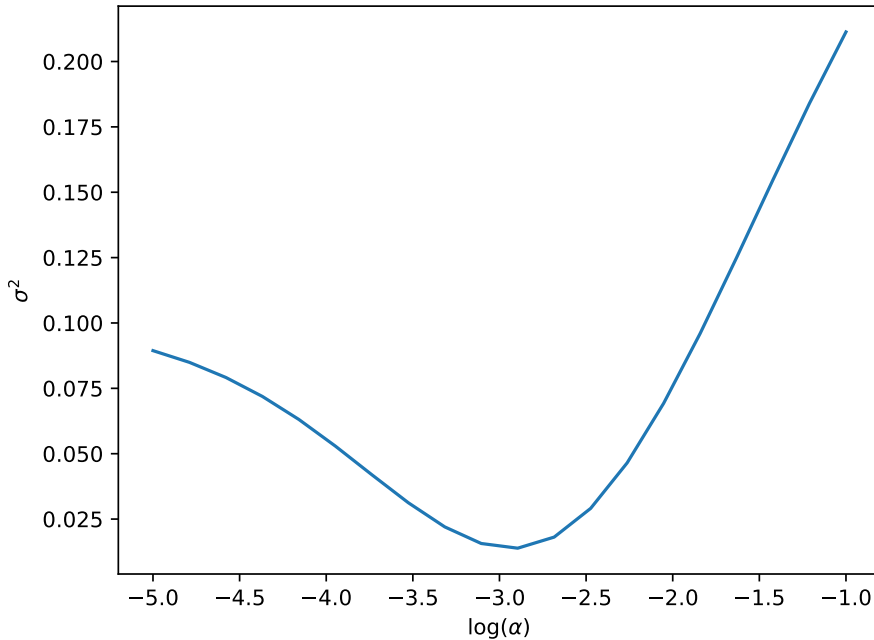


Figure 4.5: Error estimation between the analytic model and simulations as a function of viscosity coefficient α_t .

at 65 au. We consider the gas density profile between 55 to 85 au, where the radial drift has stopped and the dust has achieved a steady state.

The concentration of the dust surface density depends on the assumed value of the viscosity coefficient α_t (equation 4.29) which is found from the best fit model by minimizing the function

$$\sigma^2 = \frac{1}{N_a N_p} \sum_a \sum_{\varpi} [\Sigma_{d,\text{norm}}^{\text{sim}}(\varpi, a) - \Sigma_{d,\text{norm}}^{\text{mod}}(\varpi, a)]^2; \quad (4.36)$$

where N_a is the number of dust particle sizes, and N_p is the number of radial points sampled, $\Sigma_{d,\text{norm}}^{\text{mod}}$ is the normalized dust surface density profile of the model, and $\Sigma_{d,\text{norm}}^{\text{sim}}$ is the normalized azimuthally-averaged dust density profile of the simulation.

The sum over ϖ compares the radial profiles and the sum over a take into account all the grain sizes, which vary from $50 \mu\text{m}$ to 1.0 cm in 10 logarithmically equally spaced bins. Figure (4.5) shows σ^2 as a function of α_t . The minimum is obtained for $\alpha_b = 1.3 \times 10^{-3}$, which is of the same order of magnitude of the averaged value, 3×10^{-3} , found in the simulation. The value of dust-to-gas mass ratio ϵ_0 is not fitted because the dust particles included in the simulation are only a representative sample of the total dust mass; that is the reason why the normalized dust surface densities are compared.

Figure (4.6) shows the normalized surface densities from the model (solid lines)

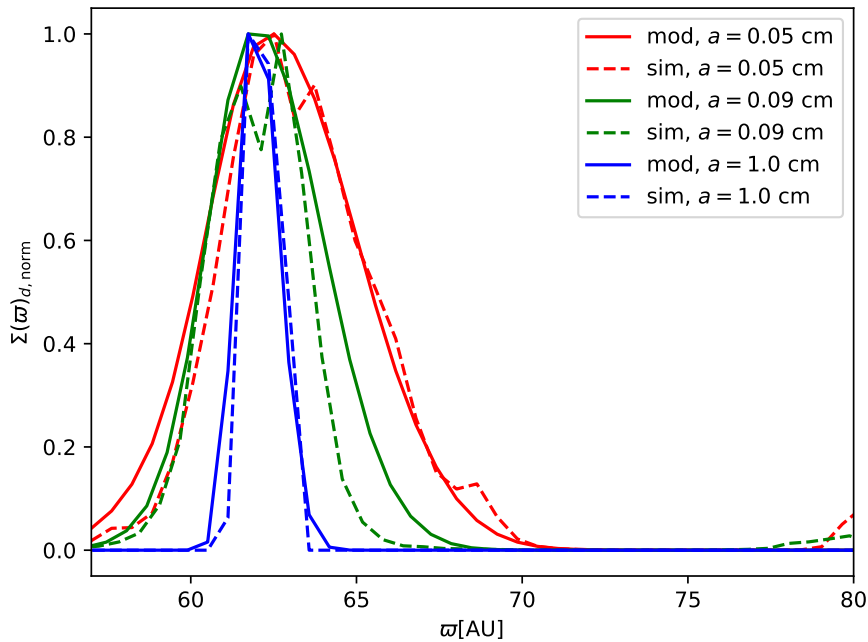


Figure 4.6: Normalized surface density from the model (solid lines) and the simulation (dotted lines) for grains with sizes $a = 0.05 \text{ cm}$ (red line), 0.09 cm (green line) and 1.0 cm (blue line).

and the simulation (dotted lines) using the viscosity coefficient α_b and for three representative dust grain sizes: $a = 0.05 \text{ cm}$ (red line), 0.09 cm (green line), and 1.0 cm (blue line). In all cases the width of the model profiles match the simulation profiles. The origin of the small differences is that the turbulence in the simulation depend on the local properties of the disk, but in the analytical model presented in this work, the parameter α is assumed to be constant in the disk.

4.4.3 Radial dust trapping in HD 169142

In this section, the analytical model (equation 4.35) is applied to give the dust surface density $\Sigma_d(\varpi)$ and simultaneously explain the millimeter dust emission of the disk around HD 169142 at different wavelengths $\lambda = 0.87, 1.3, 3.0 \text{ mm}$, using the observed gas properties.

Section (4.4.3.1) summarizes the observed properties of the central star and the disk in this source. Section (4.4.3.2) derives the disk gas surface density and excitation temperature from the ^{12}CO and ^{13}CO maps. These disk gas properties are used in the analytical model to predict the dust surface density, in order to determine the best fit values for the global dust-to-gas mass ratio (ϵ_{global}) and the viscosity coefficient (α_t). We choose the parameters that minimize the reduced chi-squared of the dust continuum emission of the observed dust maps and the emission of a grid

of models. Section (4.4.3.3) describes how the dust properties are computed, and Section (4.4.3.4) presents the results for the best values of ϵ_{global} and α_t .

4.4.3.1 HD 169142

HD 169142 is a Herbig Ae star (The et al., 1994) in the Sagittarius constellation with an age of 10 Myr (Pohl et al., 2017), a mass of $M_* = 1.65 M_\odot$ (Blondel & Djie, 2006) with an effective temperature $T_* = 8100$ K, a star radius of $R_* = 2.2 R_\odot$ (Osorio et al., 2014), and at a distance of $d = 117 \pm 4$ pc (Gaia Collaboration et al., 2016). The disk around HD 169142 is seen almost face-on, with an inclination angle of ~ 14 degrees ($\cos i = 0.974$), and with its major axis along a position angle P.A. = 5 deg (Raman et al., 2006) on the plane of the sky.

IR-polarized scattered-light images (Quanz et al., 2013) revealed that the disk has a central cavity, surrounded by a bright rim of radius $\sim 0.21''$ (~ 25 au at 117 pc), and an annular gap ranging from $\sim 0.28''$ - $0.48''$ (~ 33 - 56 au) in radius. Millimeter observations (Fedele et al. 2017, Macías et al. 2017) confirm the first ring and also reveal a second rim of radius $\sim 0.21''$ (~ 60 au at 117 pc). An unresolved IR source was detected inside the central cavity (Biller et al. 2014, Reggiani et al. 2014) at a radius of $\sim 0.16''$ (19 au) and was interpreted as a substellar or planetary companion candidate. The dust thermal emission of the disk was first imaged with the VLA at 7 mm (Osorio et al. 2014, Macías et al. 2017). These 7 mm observations confirmed the IR results and revealed that the ring of radius 25 au is indeed narrow and azimuthally asymmetric, with a bright knot at PA= -40 deg. These 7 mm images also suggest the presence of a possible new gap at radius ~ 85 au, located very close to the CO snowline, as imaged from DCO⁺ ALMA data (Macías et al., 2017). Finally, the VLA observations revealed a compact source of ionized material near the center of the cavity that could be tracing a weak radio jet, a photoionized inhomogeneous region of the inner disk, or an independent orbiting object.

The HD 169142 disk has been observed with ALMA at $\lambda = 0.87$ mm, 1.3 mm, and 3 mm (archival data from program 2012.1.00799.S, Fedele et al. 2017, and Macias et al. 2019). The submillimeter and millimeter continuum ALMA maps of the dust nicely confirmed the ringed structure of the disk initially revealed by the infrared polarized images and the 7 mm observations. The line emission of the gas has been observed with ALMA using ¹²CO, ¹³CO, C¹⁸O $J : 2 \rightarrow 1$ rotational transitions by Fedele et al. (2017).

In all the cases, the contrast between the rings and the gaps in the line emission maps is weaker than in the continuum maps. For the ¹²CO this could be a consequence of the line emission being optically thick. However, the ¹³CO emission,

that is usually optically thin, also shows a smaller contrast compared to the dust emission; this behavior is similar to the dust model described in Section (4.4.1). Also, the line emission extends to a radius of ~ 240 au, significantly larger than the radius inferred from the dust continuum emission, which only extends to ~ 100 au. This difference could be explained by the radial dust migration (e.g., Brauer et al. (2008)).

Figure (4.7) shows the normalized azimuthally-averaged⁵ specific intensity of the dust continuum emission at $\lambda = 870 \mu\text{m}$ (red solid line), 1.3 mm (yellow dash-dotted line), and 3 mm (green dashed line). It also shows the normalized azimuthally-averaged profiles the velocity-integrated specific intensity of the $^{13}\text{CO } J : 2 \rightarrow 1$ (cyan solid line) and the $^{12}\text{CO } J : 2 \rightarrow 1$ (blue dash-dotted line) line emission. All the dust maps were convolved to the same circular beam of 0.20 arcsec, while the gas maps have a circular beam of 0.16 arcsec. These beams are equivalent to 23.4 and 18.7 au at the assumed distance of 117 pc respectively. Note that, since the dust analytical model depends on the gas surface density (equation 4.35), the model can only resolve dust structures with the angular resolution of the gas maps; this is the reason why we choose a higher angular resolution in the gas; however, prior to compare the dust properties from the observations and the analytic model, we convolve the analytic dust model such that the final beam coincide with the observations.

From now on, for simplicity of the model and because the disk inclination in the plane of the sky ($\cos i = 0.974$) is small, we consider that the disk is face-on. Then, the curves shown in Figure 4.7 are assumed to correspond to a face-on disk.

4.4.3.2 Gas surface density

The gas surface density can be inferred using both an optically thin and an optically thick line. We use the $J : 2 \rightarrow 1$ lines and assume that ^{12}CO is optically thick and the ^{13}CO is optically thin. The ^{13}CO column density for the $J : 2 \rightarrow 1$ rotational transition (e.g. Estalella & Anglada (1994)) is given by

$$N^{13\text{CO}} = c_0 \tau_0^{13} T_{\text{ex}} \Delta v \left[\frac{\exp[3h\nu/(2k_B T_{\text{ex}})]}{\exp[h\nu/(k_B T_{\text{ex}})] - 1} \right], \quad (4.37)$$

where $c_0 = 16\pi k_B \nu^2 J / [(2J + 1)hc^3 A_{J,J-1}]$, h, k_B are the Planck and Boltzmann constants, Δv is the line width and $\nu = 230 \text{ GHz}$, $A_{2,1} = 3.25 \times 10^{-7} \text{ s}^{-1}$ are the frequency and the Einstein coefficient for this transition, respectively. The excitation

⁵Taking into account the disk inclination in plane of the sky.

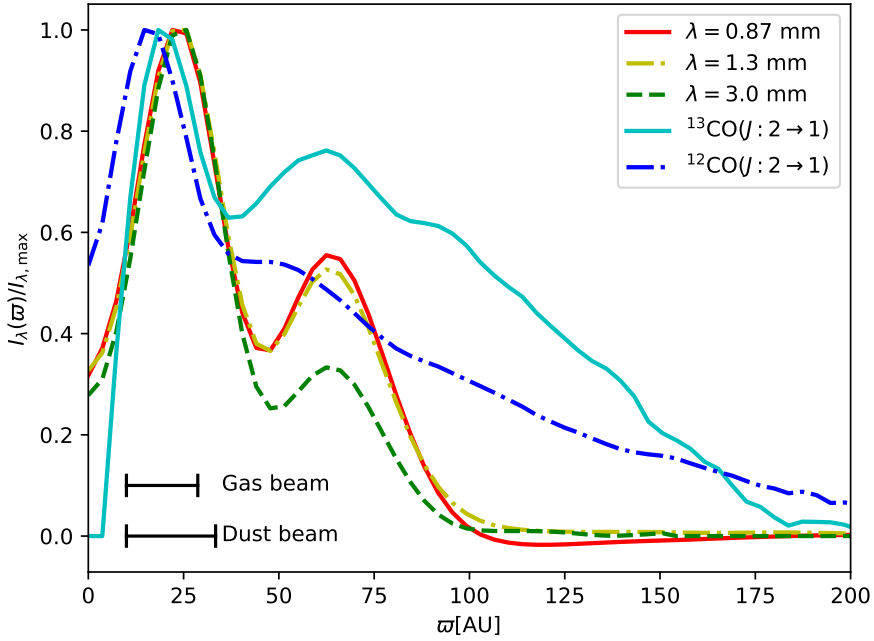


Figure 4.7: Normalized HD 169142 specific intensities as a function of disk radius. The continuum dust emission at $\lambda = 0.87, 1.3$, and 3.0 mm are represented by the red solid line, yellow dash-dotted line, and green dashed line respectively. The velocity-integrated specific intensity of the ^{13}CO and ^{12}CO molecules are the cyan solid line and the blue dash-dotted line respectively. The dust emission maps have been convolved to a beam of 0.2 arcsec, while the gas maps were convolved to a beam of 0.16 arcsec (bottom left bars).

temperature T_{ex} is given by

$$T_{\text{ex}} = \frac{h\nu/k_B}{\ln \left[1 + \frac{h\nu/k_B}{T_0^{12} + \mathcal{J}^{12}(2.7\text{K})} \right]}, \quad (4.38)$$

where T_0^{12} is the brightness temperature of the ^{12}CO J: $2 \rightarrow 1$ line, $\mathcal{J}_\nu(T) = (h\nu/k)/(\exp(h\nu/kT) - 1)$ is the velocity-integrated specific intensity in units of temperature, and $\mathcal{J}^{12}(2.7\text{K})$ is the intensity at the frequency of the ^{12}CO J: $2 \rightarrow 1$ evaluated at the background temperature. Finally, the optical depth of the ^{13}CO J: $2 \rightarrow 1$ line (τ_0^{13}) is given by

$$\tau_0^{13} = -\ln \left[1 - \frac{T_0^{13}}{\mathcal{J}^{13}(T_{\text{ex}}) - \mathcal{J}^{13}(2.7\text{K})} \right], \quad (4.39)$$

where T_0^{13} is the brightness temperature of the ^{13}CO J: $2 \rightarrow 1$ line, and $\mathcal{J}^{13}(T_{\text{ex}})$ is the intensity evaluated at the excitation temperature. We find that $\tau_0^{13} < 0.8$ throughout the disk.

Figure (4.8) shows the brightness temperature of the ^{13}CO (red line), ^{12}CO (blue

line), and the excitation temperature (green line) as a function of the disk radius. Note that at all radii $T_{\text{ex}} > T_0^{12} > T_0^{13}$.

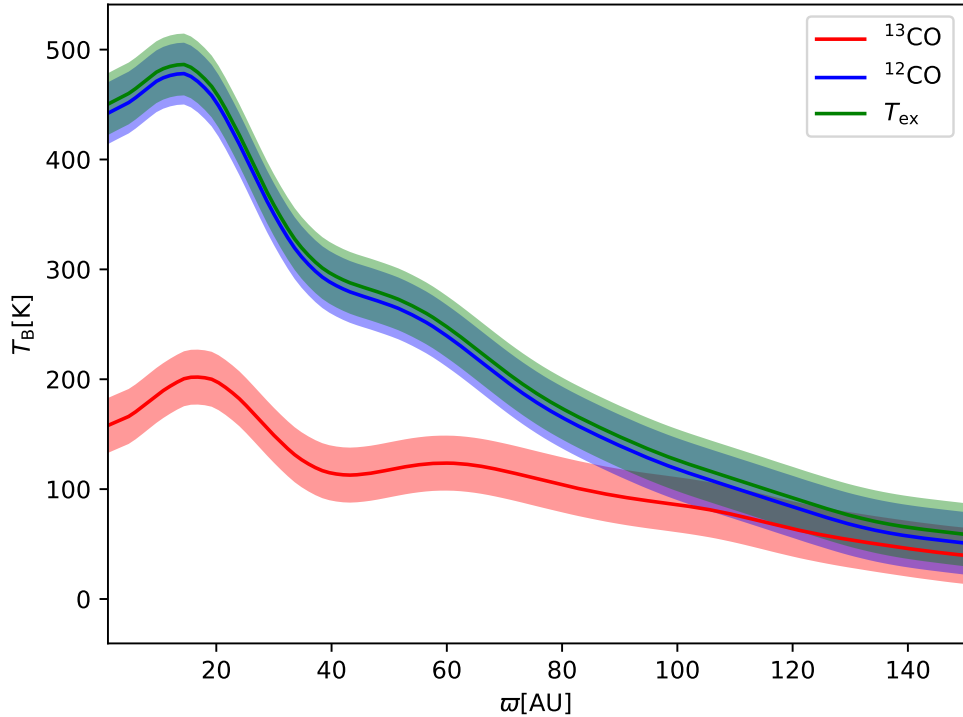


Figure 4.8: HD 169142 CO brightness temperature. The red, blue and green lines are the ^{13}CO , ^{12}CO brightness temperature and the excitation temperature, respectively, as a function of the disk radius. The width of each curve corresponds to the error associated to the RMS of each image.

To obtain the gas surface density at each radius one needs an abundance factor between ^{13}CO and H_2 (which dominates the gas mass), such that $\Sigma_g = m_{\text{H}_2} [\text{H}_2 / ^{13}\text{CO}] \times N^{^{13}\text{CO}}$. The abundance is obtained by normalizing the gas surface density with the total mass of the disk $M_{\text{disk}} = 2\pi \int_0^R \Sigma_g \varpi d\varpi$. For a disk mass of $M_{\text{disk}} = 0.019 M_{\odot}$ (Fedele et al., 2017), the abundance between the ^{13}CO and the H_2 molecules of $[^{13}\text{CO}/\text{H}_2] = 1.0 \times 10^{-5}$, similar to values found in the ISM (e.g. Dickman (1978)).

The top panel of Figure (4.9) shows the gas surface density model as a function of the radius. The width of the line gives the uncertainty in the gas surface density due to the noise of the CO maps and the error propagation. In the next section we use this gas surface density to model the dust surface density using equation (4.35).

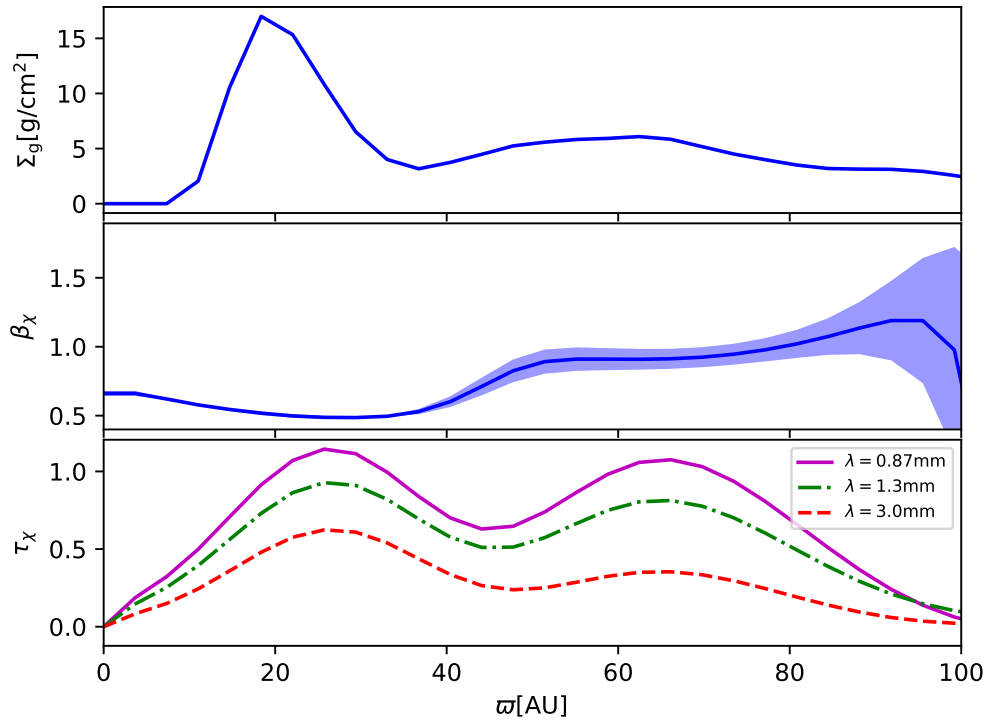


Figure 4.9: HD 169142 disk properties. Top panel: Gas surface density model derived from the assumed ^{12}CO (optically thick) and ^{13}CO (optically thin) emission. Middle panel: Opacity spectral index β_χ (between $\lambda = 870 \mu\text{m}$ and 3 mm) of the dust emission. Bottom panel: Optical depth (absorption + scattering) at $\lambda = 0.87 \text{ mm}$ (magenta solid line), 1.3 mm (green dash-dotted line), and 3.0 mm (red dashed line).

4.4.3.3 Dust properties

In order to infer the dust properties, it is assumed that the dust temperature follows a power-law with the disk radius given by

$$T_d = T_0 \left(\frac{\varpi}{\varpi_0} \right)^{-q}, \quad (4.40)$$

where $T_0 = 500 \text{ K}$ at $\varpi_0 = 1 \text{ au}$ and $q = 1/2$. This slope is estimated by assuming an equilibrium between the star incident radiation and the dust grains emission, such that $T_d^4 \approx T_*^4 W(\varpi)$, where $W(\varpi)$ is the dilution factor given by $W(\varpi) = 1/2(1 - [1 - (R_*/\varpi)^2]^{1/2})$, and T_* , R_* are the effective temperature and radius of the star respectively (Section 4.4.3.1). Since a large dust central hole has been previously reported in the disk around HD 169142 (e.g. Fedele et al. 2017, Macías et al. 2017), the inner and outer dust radius are set to be 15 au and 90 au respectively.

All the dust opacity properties are the same as in Chapter 2. To determine the maximum grain size, $a_{\max}(\varpi)$, one has to fit a power-law to the observed intensity

I_ν and relate the observed opacity spectral index β_{obs} with the maximum grain size (as discussed in chapter 2). From this method one can find $a_{\max}(\varpi)$ at each radius⁶.

The middle panel of Figure (4.9) shows β_{obs} derived from the dust continuum observations following the latter procedure, without assuming optically thin emission nor the Rayleigh-Jeans approximation, and including the scattering effects. The width of the curve represents the error in the fit. The error is negligible for $\varpi < 80$ au, where the signal-to-noise ratio in the dust emission maps is high. The bottom panel of the same Figure shows the optical depth (absorption + scattering) at $\lambda = 870 \mu\text{m}$ (magenta solid line), 1.3 mm (green das-dotted line), and 3.0 mm (red dashed line): the disk is optically thin at $\lambda = 1.3$ mm and 3.0 mm; it is only marginally thick close to the two maxima at $\lambda = 870 \mu\text{m}$. As mentioned before, we assume a face-on disk. Then, the optical depth in Figure (4.9) refers to that measured along the disk axis. The optical depth along the line of sight is larger by a negligible factor of $1/\cos(i) \sim 1.03$.

Figure (4.10) shows the maximum grain size, $a_{\max}(\varpi)$, as a function of the disk radius assuming a slope of the particle size distribution of $p = 2.5$ (magenta solid line), 3.0 (green dash-dotted line), and 3.5 (red dashed line) (see more details in Appendix A). In the following we assume $p = 3.5$ and in Section (4.4.3.5) we discuss this assumption.

We find that $a_{\max}(\varpi)$ is very large at the position of the first maximum ($a_{\max} > 10$ cm) and decreases with the disk radius, reaching a value of ~ 2 mm at $\varpi = 90$ au. This behavior could be due to differential radial migration of the dust grains toward the gas pressure maxima and/or dust growth. In previous works (e.g. Calvet et al. 2005), the large values of the maximum grain size have been avoided by decreasing the slope of the particle size distribution. The reason is that the largest particles need to contribute significantly to the opacity, which is not true for grains so much larger than the wavelength (Draine, 2003). For example, in this disk, the maximum grain size in the inner ring is ~ 3 mm, 1 mm if the slope of the particle size distribution is $p = 3.0, 2.5$ respectively.

4.4.3.4 Best fit dust model

The dust-to-gas mass ratio ϵ_{global} and the α_t parameter that appear in equations (4.29) and (4.35) are the unknown parameters of the dust model.

These parameters are fitted by creating a grid of models and comparing their radial intensity profiles ($I_\lambda^{\text{mod}}(\varpi)$) with the observed azimuthally averaged intensity

⁶See discussion about on the degeneracy between a_{\max} and the slope p in Section (4.4.3.5).

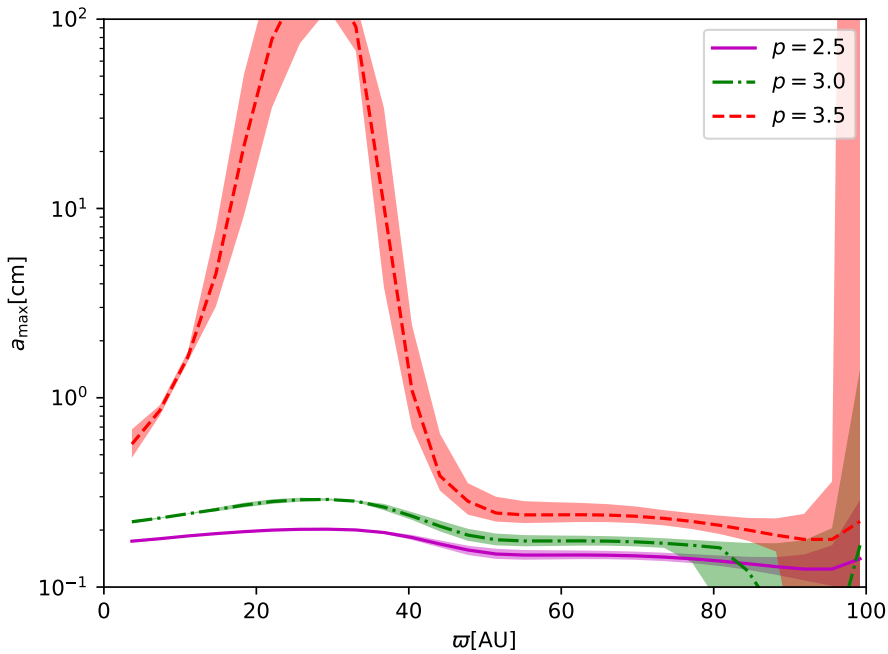


Figure 4.10: Maximum grain size as a function of the radius for different slopes in the particle size distribution: $p = 2.5$ (magenta solid line), 3.0 (green dash-dotted line), and 3.5 (red dashed line).

profiles ($I_\lambda^{\text{obs}}(\varpi)$) at each wavelength. We vary α_t from 10^{-5} to 10^{-1} , while ϵ_{global} varies from 10^{-4} to 10^{-1} . The number of models for each parameter is 50 (the total number of models is 50×50) and the values are logarithmically equally spaced. Left panels of Figure (4.11) show the reduced chi-squared

$$\chi^2_{r,\lambda} = \frac{1}{N_p} \sum_{\varpi} \left[\frac{I_\lambda^{\text{mod}}(\varpi) - I_\lambda^{\text{obs}}(\varpi)}{\sigma_\lambda^{\text{obs}}(\varpi)} \right]^2, \quad (4.41)$$

of the dust models at $\lambda = 870 \mu\text{m}$ (first row), 1.3 mm (second row), and 3.0 mm (third row), where N_p is the number of radii and $\sigma_\lambda^{\text{obs}}(\varpi)$ is the uncertainty of the observed intensity at each radius. The latter is given by

$$\sigma_\lambda^{\text{obs}}(\varpi) = \text{RMS}_\lambda / \sqrt{n}, \quad (4.42)$$

where RMS_λ is the root mean square noise of the observed map, and n is the number of beams within the area of each ring. The right panels show the intensity profiles of the best dust models (red solid line), the optical depth models (green dashed line), and the observed intensity profiles (blue line) whose error is given by the width of the line.

Figure (4.12) plots the isocontours where the value of the reduced chi-squared

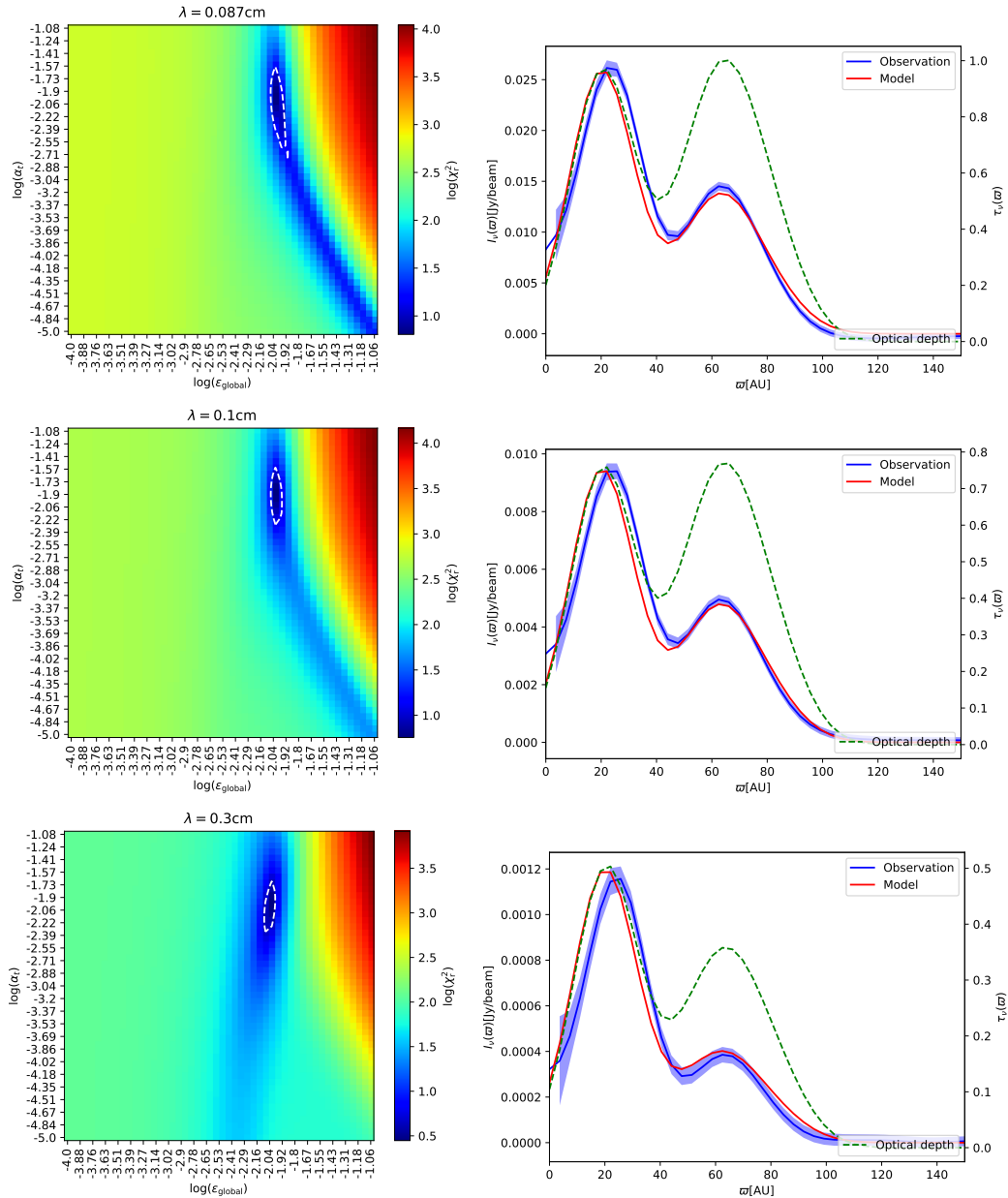


Figure 4.11: Exploration of the parameter space for the dust continuum emission at $\lambda = 870\text{ }\mu\text{m}$ (first row), 1.3 mm (second row), and 3.0 mm (third row). Left panels: Reduced chi-squared (χ^2_r) for different dust models in the $(\epsilon_{\text{global}}, \alpha_t)$ space. The white dashed lines are the isocontours where the reduce chi-squared is equal to 1.5 times the minimum value of χ^2_r at each wavelength. Right panels: Best model at each wavelength; the blue line is the observational dust continuum emission, the red solid line is the best emission model and the green dashed line is the best optical depth model.

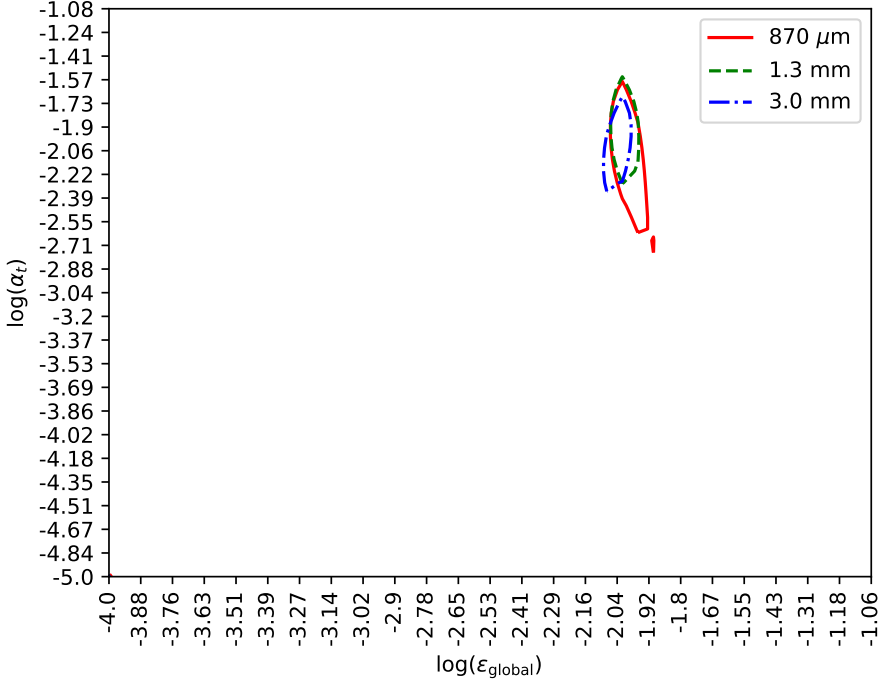


Figure 4.12: Isocontours where the reduced chi-squared is equal to 1.5 times the minimum value of χ^2_r for each wavelength $\lambda = 870 \mu\text{m}$ (red solid line), 1.3 mm (green dashed line), and 3.0 mm (blue dash-dotted line).

Table 4.1: Best physical parameters

λ (mm)	$\log(\alpha_t)$	$\log(\epsilon_{\text{global}})$
0.87	-1.90 ^{+0.33} _{-0.73}	-1.98 ^{+0.12} _{-0.06}
1.3	-1.82 ^{+0.25} _{-0.48}	-1.98 ^{+0.06} _{-0.06}
3.0	-1.90 ^{+0.17} _{-0.40}	-1.98 ^{+0.06} _{-0.12}

is 1.5 times the minimum value of $\chi^2_{r,\lambda}$ for all wavelengths: $\lambda = 870 \mu\text{m}$ (red solid line), 1.3 mm (green dashed line), and 3.0 mm (blue dash-dotted line). The best parameters at each wavelength are summarized in Table (4.1). The uncertainties of the parameters correspond to the maximum and minimum values of each variable within the isocontours. To obtain a global model, one requires that the parameters do not depend on wavelength. The best values for ϵ_{global} are the same, and the best values of α_t slightly differ with wavelength. Therefore, the best averaged parameters that describe the dust concentration in the disk of HD 169142 are: $\epsilon_{\text{global}} = (1.05^{+0.15}_{-0.13}) \times 10^{-2}$ and $\alpha_t = (1.35^{+0.51}_{-0.85}) \times 10^{-2}$; this means that the total dust mass is $(2.0^{+0.28}_{-0.25}) \times 10^{-4} M_\odot$. Note that the fitted value of α_t depends on the resolution of the gas structure. For example, if in higher angular resolution observations a ring fragments into thinner rings, that would require a smaller value of α_t to concentrate the dust in these rings.

Figure (4.13) shows the disk maps for different wavelengths; the left panels are the observed maps, the middle panels show the emission of the dust model with the best averaged parameters, and the right panels are the maps of absolute differences ($|\text{observation} - \text{model}|$). The wavelength increases from top to bottom ($\lambda = 870 \mu\text{m}$, 1.3 mm , 3 mm respectively). The white lines in the difference maps are the isocontours where the difference is 5 times the RMS of each map. The main differences between the observations and models are the non-axisymmetric structures, which are not taken into account in the dust model, which assumes an axi-symmetric disk. A bidimensional analysis of this disk should be done in order to improve the difference maps and explain the azimuthal asymmetries. For this, deeper observations of this disk with the VLA at $\lambda = 7 \text{ mm}$ (Macías et al., 2017), which reveal that the inner ring has important azimuthal substructures, could be included to improve the fits.

For the best averaged parameters, Figure (4.14) shows the dust surface density (the red solid line), the local dust-to-gas mass ratio (green dashed line), the global dust-to-gas mass ratio ϵ_{global} (green dotted line), and the gas surface density scaled by the global dust-to-gas mass ratio (blue dash-dotted line). The latter would mimic the dust surface density if there is no dust migration, which is not the case in HD 169142. The local dust-to-gas mass ratio in the first maximum increases by a factor of 6 compared with the global dust-to-gas mass ratio; while in the second local maximum it is below the average value. In addition, this figure shows that the maximum dust-to-gas mass ratio is less than 0.06, therefore, one can neglect the back reaction of the dust on the gas. Similar values of the dust-to-gas mass ratio (~ 0.05) have been found in many disks, e.g. in the disks around HD 169142 (Panić et al., 2008), TW Hydra (Thi et al., 2010), HD 245185 (Ansdell et al., 2015), HD 100546 (Miley et al., 2019), and in the Lupus (Ansdell et al., 2016) and Orion Nebula cluster (Eisner et al., 2016).

The amplitude of the dust surface density in the second maximum ($\varpi = 60 \text{ au}$) is much smaller than in the first maximum ($\varpi = 24 \text{ au}$), in contrast with the behavior of the intensity profiles (bottom panels of Figure (4.11)); this occurs because of opacity effects associated to the maximum grain size at each radius: In the first maximum, the grains have a maximum size larger than 10 cm; such grains do not have a large opacity at millimeter wavelengths. However, in the second maximum, the grains have a maximum size $\sim 2 \text{ mm}$, which have a large opacity at millimeter wavelengths. For this reason, the contrast in the maxima of the dust surface density is larger than expected.

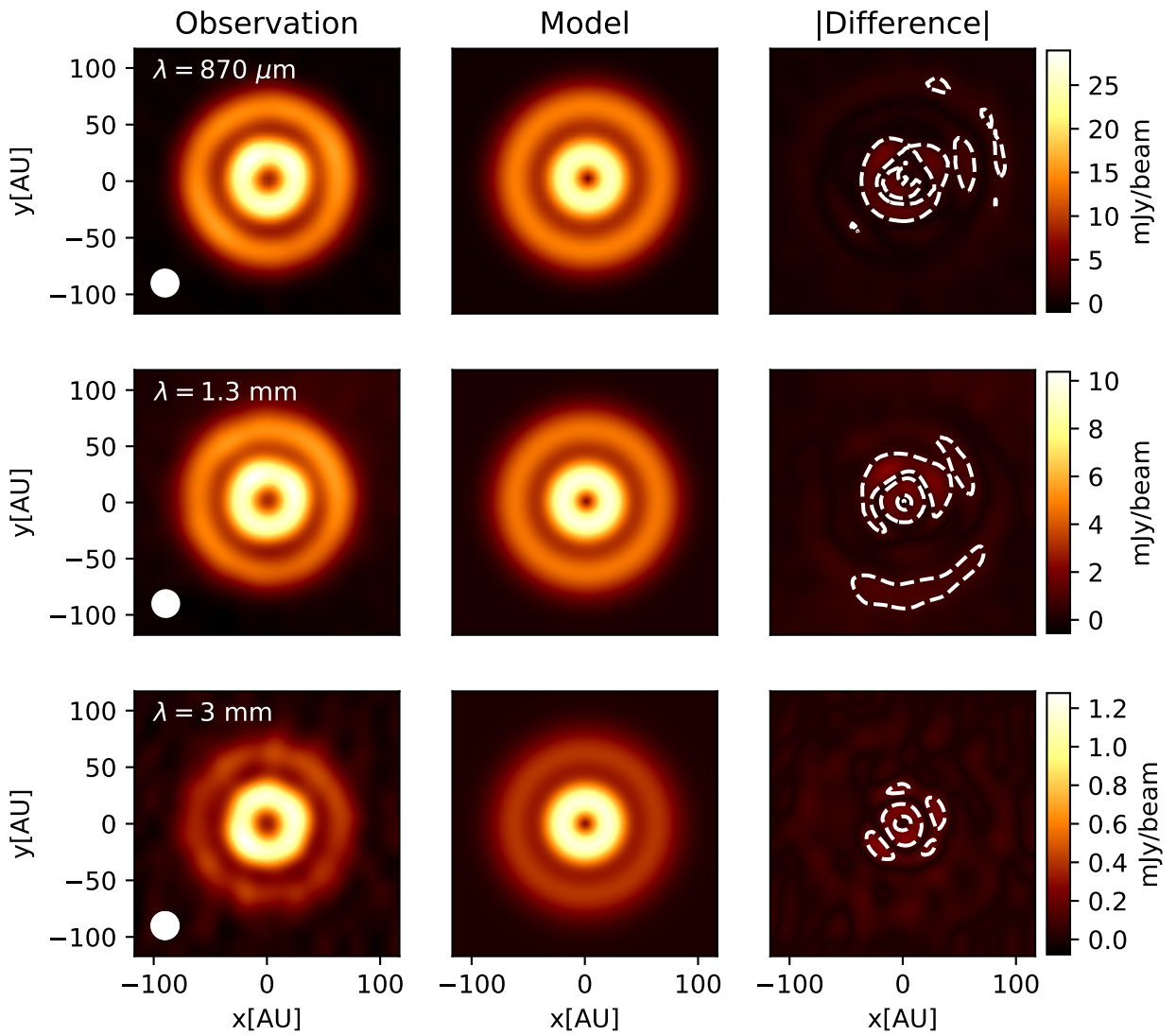


Figure 4.13: Maps of the thermal dust emission at $\lambda = 870 \mu\text{m}$ (first row), 1.3 mm (second row), and 3.0 mm (third row). The left, middle and right panels are the observational, model and difference maps. The white lines of the difference maps are the isocontours where the difference is 5 times the RMS of each map.

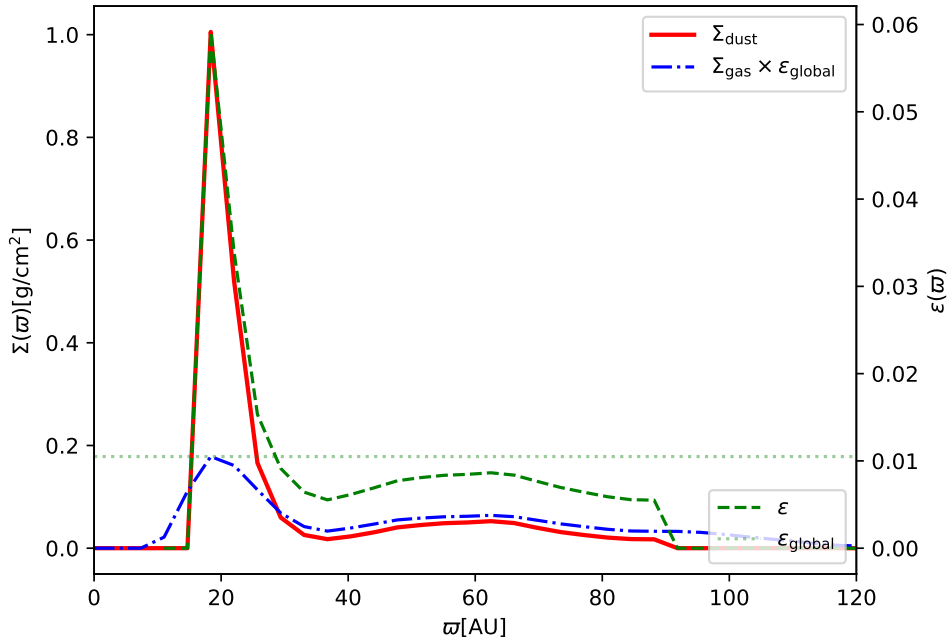


Figure 4.14: Dust properties using the best averaged parameters: $\epsilon_{\text{global}} = 1.05 \times 10^{-2}$, $\alpha_t = 1.35 \times 10^{-2}$. The red solid line is the dust surface density, the blue dash-dotted line is the gas surface density scaled by the global dust-to-gas mass ratio, the green dashed line is the local dust-to-gas mass ratio, and the green dotted line is the global dust-to-gas mass ratio.

4.4.3.5 Degeneration between a_{\max} and p

The opacity spectral index (β_χ) can be explained by a maximum grain size a_{\max} for a given value of the slope of the particle size distribution p (see Figure 2.4). However, if the latter changes, the maximum grain size should be modified constrained by the value of β_χ . The degeneration between these two variables is shown in Appendix A.

In this section we study the local changes of the particle size distribution due to dust size differential migration, and change the maximum grain size consistently.

The model to obtain the slope p as a function of the disk radius based on the results of the analytical model (Section 4.4.1) as follows: If the total dust surface density is given by equation (4.31), the term $\Sigma_d(\varpi, a)n(a)da$ can be interpreted as proportional to the local particle size distribution after dust concentration. If $n_2(a)da$ is this new distribution and c_1 the proportionality factor, then,

$$n_2(a)da = c_1 \Sigma_d(\varpi, a)n(a)da. \quad (4.43)$$

The number of particles per unit volume must be the same as the original when averaged in all the disk area A ; then $\int_A n_2(a)da dA = \int_A n(a)da dA$. So, the propor-

tionality factor is constrained by

$$c_1 = \frac{A}{\int_A \Sigma_d(\varpi, a) dA}. \quad (4.44)$$

Then, substituting equations (4.28, 4.44) in equation (4.43), one obtains

$$\begin{aligned} n_2(a)da &= \left[\frac{A\Sigma_g(\varpi) \exp[-ka]}{\int_A \Sigma_g(\varpi) \exp[-ka] dA} \right] n(a)da, \\ a^{-p_2} &\propto \left[\frac{\exp[-ka]}{\int_A \Sigma_g(\varpi) \exp[-ka] dA} \right] a^{-p}. \end{aligned} \quad (4.45)$$

Equation (4.45) only depends on the viscosity coefficient α_t via the factor k defined in equation (4.29). One expects that, if the viscosity coefficient $\alpha_t \rightarrow \infty$ (i.e. $k \rightarrow 0$), there is no dust differential migration and the dust particle size distribution does not change, i.e., $p_2 = p$.

For the gas surface density $\Sigma_g(\varpi)$ in the top panel of Figure (4.9), we fit the term within the brackets of equation (4.45) with a power-law in order to obtain the value of p_2 for different values of α_t . The top panel of Figure (4.15) shows p_2 as a function of the radius for 3 values of α_t , assuming that the original distribution has a slope $p = 3.5$. The blue solid line represents a relatively low value of α_t , the green dashed line of an intermediate value, and the red dash-dotted line of a high value⁷. One recovers the original value of p for the large value of α_t as expected. For intermediate and low values of α_t , the slope p_2 decreases from its original value (p) in the inner disk and increases in the outer disk.

The bottom panel of Figure (4.15) shows the maximum grain size a_{\max} needed to explain the value of β_{obs} shown in the middle panel of Figure (4.9), given the p_2 curves shown in the top panel (see Appendix A). Note that for small turbulence, the value of p_2 decreases at $\varpi \sim 30$ au. Then, part of β_{obs} is explained by the decrease of p_2 , and the maximum grain size needed to explain the observed opacity spectral index does not need to be as large as the case with $p = 3.5$. Therefore, any physical process that changes the slope $p \rightarrow p_2$, will alter the inferred value of a_{\max} .

4.5 Azimuthal dust trapping

One of the ideas proposed in order to avoid the fast radial migration of the dust grains toward the central star is dust trapping in azimuthal pressure bumps. Barge

⁷One refers to the magnitude of α_t compared with the Stokes number. A large, intermediate and low value of α_t in this context means $St/\alpha_t \gg 1$, $St/\alpha_t \sim 1$, and $St/\alpha_t \ll 1$ respectively.

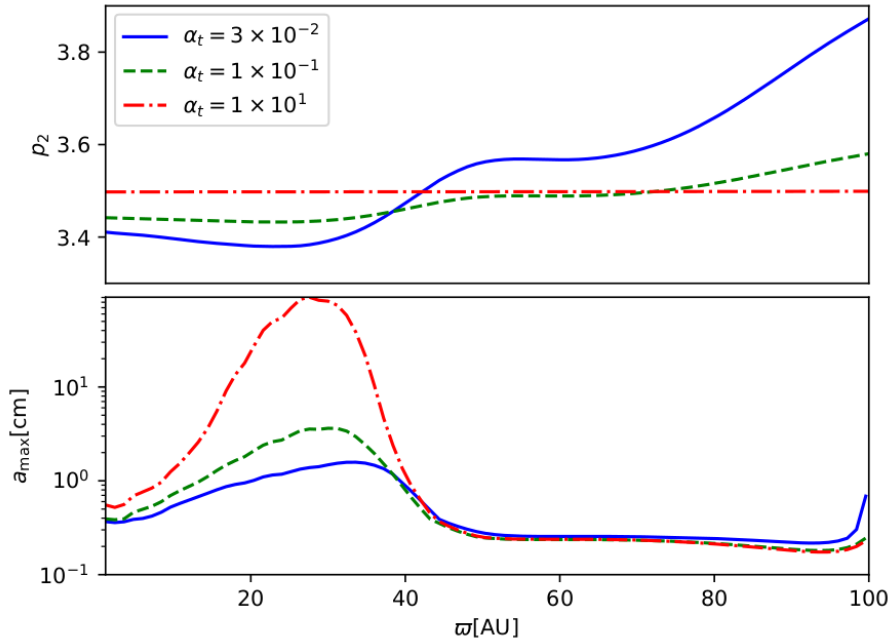


Figure 4.15: Degeneration between p and a_{\max} to explain the profile of β in the HD 169142 disk.

& Sommeria (1995) found that persistent gaseous vortices can effectively concentrate and segregate large amounts of solid particles via pressure gradients, possibly starting the formation of planetesimals. The dynamics of large scale vortices has been studied using 2D (Surville & Barge, 2015) and 3D (Richard et al., 2013) hydrodynamical simulations in protoplanetary disks; these azimuthal asymmetries naturally arise due to the Rossby wave instability (Li et al., 2000) or the baroclinic instability (e.g. Barge et al. 2016) in the outer edge of the dead zone, where turbulence due to the Magneto Rotational Instability (MRI) is depressed due to the low ionization state of the disk material. These structures can survive over a hundred rotation periods (measured at the radius of the center of the vortex) and increase the dust to gas mass ratio one order of magnitude (Inaba & Barge, 2006). This large concentration of dust mass could become gravitationally unstable, and start the formation of planetesimals.

High angular resolution mm observations with ALMA and VLA , and infrared observations with SPHERE on the VLT have found large scale structures in several sources that could be the signatures of vortices in the disk. Some examples are the disks around the young stars Oph IRS 48 (van der Marel et al., 2013), HD 142527 (Casassus et al., 2013), LkH α (Isella et al., 2013), MWC 758 (Marino et al., 2015), SAO 206462, and SR 21 (Pérez et al., 2014). Spiral arms structures have also been found in the dust emission, e.g., around MWC 758 and Elias 2-24 (Benisty et al.

(2015); Pérez et al. (2016)). These observations are important to understand the gas dynamics and the physical processes that could lead to the formation of planetesimals in protoplanetary disks. They also set important constraints to the parameters used in the theoretical models.

In this section we consider the millimeter emission of a dust vortex in a protoplanetary disk obtained from the gas numerical simulation performed by Barge et al. (2017). We extend the Lyra-Lin dust vortex model (Lyra & Lin, 2013) for a single grain size to a power-law distribution of grain sizes. To calculate the dust millimeter emission we compute dust opacities in different regions of the vortex according to the size segregation, which changes the dust to gas mass ratio and the slope in the particle size distribution. The effects of scattering and true absorption are both included. The dust surface density model (Section 4.5.2) allows us to calculate the local dust properties (particle size distribution and dust to gas mass ratio) as a function of the position in the disk vortex. Section (4.5.3) presents the simulated disk observations at mm wavelengths. Section (4.5.4) compares the emission of a model without dust segregation, and in Section (4.5.5) the scattering is neglected when creating the simulated disk observations. Finally, in 4.5.6, we discuss the case when the maximum grain radius in the dust particle size distribution is 1 cm.

4.5.1 Gas disk model

For the disk and the vortex, we use the result of numerical simulations of Barge et al. (2017) performed over 100 rotations of the vortex around a $2 M_{\odot}$ star. The vortex is located at 60 au from the star. The disk has a mass $M_d = 0.14 M_{\odot}$ and a disk radius $R_d = 100$ au, which mimic the disk around the Oph IRS 48 young star. Figure 4.16 shows the gas surface density Σ_g and the gas temperature T of the disk as a function of the cartesian coordinates (x, y) . The gas temperature increases toward the vortex center because the gas is assumed adiabatic with an adiabatic index $\gamma_{\text{ad}} = 1.4$; then, given the ideal gas equation and the gas pressure $P \propto \Sigma_g T$, the adiabatic equation can be written as $T \propto 1/\Sigma_g^{1-\gamma_{\text{ad}}} \propto \Sigma_g^{0.4}$.

In the vertical direction (z), the disk is assumed to be isothermal and in hydrostatic equilibrium. We assume a distance $d = 120$ pc, similar to the distance to Oph IRS 48.

4.5.2 Dust disk model

In a gaseous vortex, the dust particles tend to drift toward the pressure maximum at a rate that depends on their coupling with the gas, measured by the Stokes number

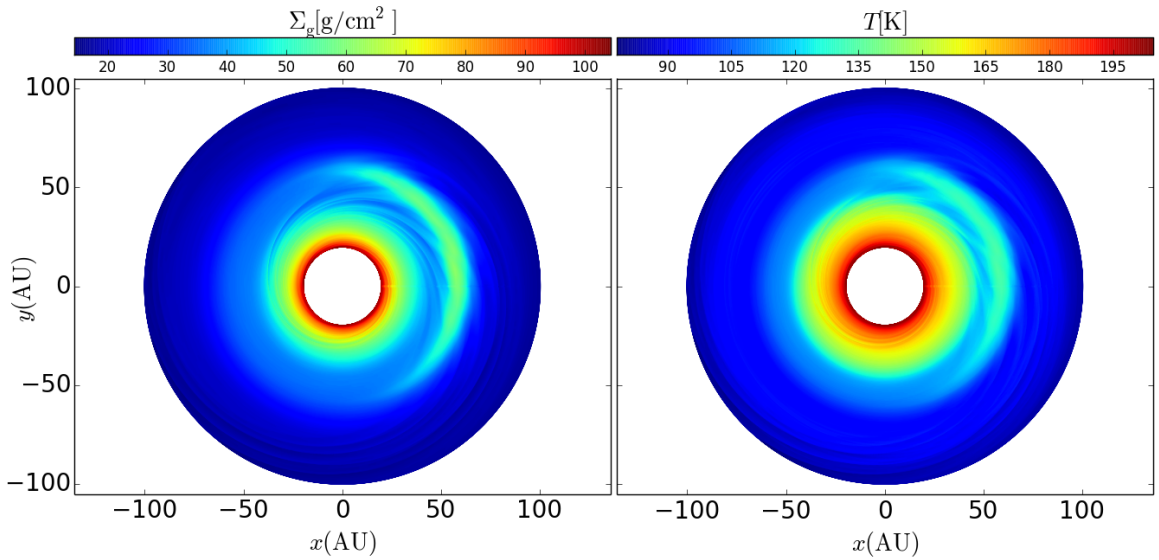


Figure 4.16: Gas surface density (left) and gas temperature (right) of a disk containing a large scale vortex (after 100 vortex rotations) obtained from the simulation of [Barge et al. \(2017\)](#).

(equation 4.25).

[Lyra & Lin \(2013\)](#) found an analytic formulation for the dust concentration in a vortex as a function of the normalized Stokes number ($S = \text{St}/\alpha_t$), where α_t is the turbulent viscosity parameter. In their model, the surface density of the gas and dust depends on the semi minor axis coordinate b that defines concentric ellipses with an aspect ratio χ , such that the semi major axis is χb . For each ellipse, the gas and dust surface density are given by

$$\Sigma_{g,V}(b) = \Sigma_{g,\max} \exp\left(-\frac{b^2}{2H_v^2}\right), \quad (4.46)$$

$$\Sigma_{d,V}(b, a) = \frac{\Sigma_{d,\max}(a)}{\sqrt{S_v + 1}} \exp\left(-\frac{b^2}{2H_v^2}(S_v + 1)\right), \quad (4.47)$$

where $\Sigma_{g,\max}$, $\Sigma_{d,\max}(a)$ are the gas and dust maximum surface densities, $H_v = H/f$ is the vortex scale length, where $f < 1$ multiplies the isothermal scale height H , this factor depends on the aspect ratio of the vortex χ . The normalized Stokes number

$$S_v = \frac{\pi \rho_m a}{2\alpha_t \Sigma_{g,\max}}, \quad (4.48)$$

is evaluated in the vortex center, since the vortex is small compared with the disk size, and the gas surface density does not vary much over its area.

For a given position in the vortex with polar coordinates (ϖ, θ) , the corresponding

ellipse has a coordinate

$$b = \sqrt{(\varpi - \varpi_0)^2 + \frac{\varpi_0^2}{\chi^2} (\theta - \theta_0)^2}, \quad (4.49)$$

where (θ_0, ϖ_0) are the coordinates of the vortex center.

The total gas surface density and the dust surface density of grains with radius a can be written as

$$\Sigma_g = \Sigma_{g,V}(b) + \Sigma_{g,back}(\varpi), \quad (4.50)$$

$$\Sigma_d(a) = \Sigma_{d,V}(b, a) + \Sigma_{d,back}(\varpi, a), \quad (4.51)$$

where $\Sigma_{g,back}(\varpi), \Sigma_{d,back}(\varpi, a)$ are the background disk gas and dust surface densities, respectively.

Since $\Sigma_d(a)$ is a function of the grain size, the total surface density of the dust depends on the particle size distribution, $n(a)da \propto a^{-p}da$. Integrating equations (4.50, 4.51) in all the disk, the mass of gas and the mass of dust with grain radius a are

$$M_g = 2\pi\chi H_v^2 \Sigma_{g,max} + M_{g,back}, \quad (4.52)$$

$$M_d(a) = \frac{2\pi\chi H_v^2 \Sigma_{d,max}(a)}{(S_v + 1)^{3/2}} + M_{d,back}(a), \quad (4.53)$$

where $M_{g,back}$ is the gas mass of the background disk and $M_{d,back}(a)$ is the background disk mass of dust with radius a .

The global dust to gas mass ratio $\epsilon(a)$ of particles with size a is defined as

$$\epsilon(a) \equiv \frac{M_d(a)}{M_g} = \frac{\frac{2\pi\chi H_v^2 \Sigma_{d,max}(a)}{(S_v + 1)^{3/2}} + M_{d,back}(a)}{2\pi\chi H_v^2 \Sigma_{g,max} + M_{g,back}}. \quad (4.54)$$

If $\epsilon(a)$ is conserved in the disk, i.e. the background disk also satisfies $\epsilon(a) = M_{d,back}(a)/M_{g,back}$, the dust is redistributed in the vortex but does not coagulate and/or fragment. Therefore, the dust maximum surface density for a size a is

$$\Sigma_{d,max}(a) = \epsilon(a) \Sigma_{g,max} (S_v + 1)^{3/2}. \quad (4.55)$$

For a particle size distribution in the background disk with $p = 3.5$, the mass is dominated by the large grains. If $M_d^c(a)$ is the cumulative dust mass from the

minimum grain size a_{\min} to a size a , then, the ratio between the cumulative mass and the total dust mass in the disk (M_d^T) is

$$\frac{M_d^c(a)}{M_d^T} = \frac{\int_{a_{\min}}^a a^3 a^{-3.5} da}{\int_{a_{\min}}^{a_{\max}} a^3 a^{-3.5} da} \approx \sqrt{\frac{a}{a_{\max}}}, \quad (4.56)$$

where $a_{\max} \gg a_{\min}$ is assumed. Furthermore, because the dust mass is dominated by the large dust particles, they can be used to trace the dust surface density. Then, we approximate the dust mass of the grain population with size a by the cumulative mass, i.e., $M_d(a) \sim M_d^c(a)$. Thus, equation (4.56) can be rewritten as

$$\frac{\epsilon(a)}{\epsilon_{\text{global}}} = \sqrt{\frac{a}{a_{\max}}}, \quad (4.57)$$

where $\epsilon_{\text{global}} = M_d^T/M_g$ is the global dust-to-gas mass ratio taking into account all the dust grain sizes.

Then, using equations (4.51, 4.55, 4.57), the dust surface density for grains with size a is

$$\begin{aligned} \Sigma_d(a) &= \epsilon_{\text{global}} \sqrt{\frac{a}{a_{\max}}} \left[\Sigma_{g,\max}(S_v + 1) \exp \left(-\frac{b^2}{2H_v^2} (S_v + 1) \right) \right. \\ &\quad \left. + \Sigma_{d,\text{back}}(\varpi) \right]. \end{aligned} \quad (4.58)$$

In this equation, the background dust surface density is written as $\Sigma_{d,\text{back}}(\varpi, a) = \epsilon(a)\Sigma_{g,\text{back}}(\varpi)$.

For the hydrodynamic simulation performed by [Barge et al. \(2017\)](#), the center of the vortex is located at $\theta_0 = 0.37$ rad and $\varpi_0 = 59.16$ au. The gas surface density is fitted using a function of the form

$$\Sigma_g = A_1 \exp \left(-\frac{b^2}{2\sigma_b^2} \right) + A_2 \left(\frac{\varpi}{60 \text{ au}} \right)^{-q}, \quad (4.59)$$

where the first term represents the vortex structure (see equations 4.46, 4.49) and the second term is the background surface density. The best fit of the numerical data leads to: $A_1 = 30.34 \text{ g cm}^{-2}$, $\sigma_b = 5.14 \text{ au}$, $\chi = 9.4$, $A_2 = 28.9 \text{ g cm}^{-2}$, $q = 1.1$. Note that $A_1 = \Sigma_{g,\max}$ and $\sigma_b = H_v$ in equation (4.46).

For a disk in hydrostatic equilibrium, the dust particle size distribution is related

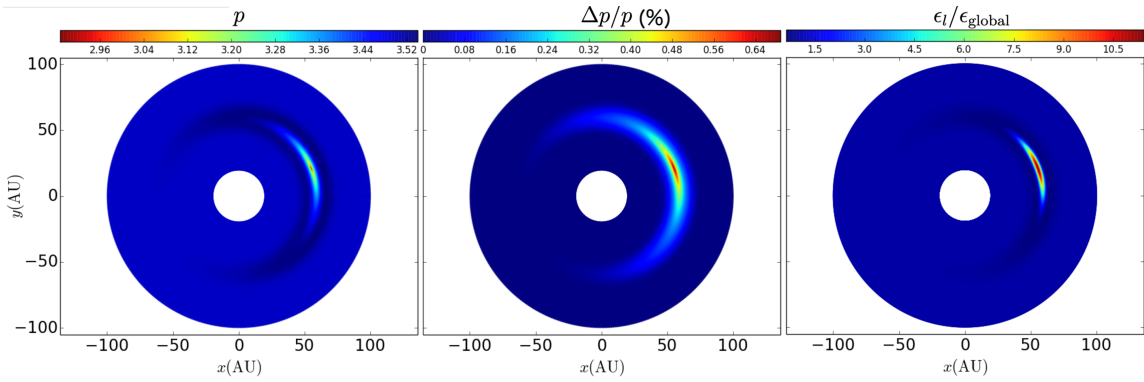


Figure 4.17: Dust particle accumulation within the vortex derived from the gas properties of Barge et al. (2017). Left panel: Slope p of the power law fit to the dust particle size distribution $n(a)da \propto a^{-p}da$ (see text). Middle panel: fractional standard deviation $\Delta p/p$. Right panel: Map of the local dust to gas mass ratio (normalized to ϵ_{global})

with the dust surface density as⁸

$$n(a) = c \left[a^{-3} \frac{d\Sigma_d(a)}{da} \right], \quad (4.60)$$

where $c = 3/(2^{5/2}\pi^{3/2}H_{\text{d}}\rho_m)$ and H_{d} is the dust scale height. Then, from equation (4.58), the dust particle size distribution is

$$\begin{aligned} \frac{n(a)}{\epsilon_{\text{global}}c} &= \left(\frac{a^{-3.5}}{a_{\text{max}}^{1/2}} \right) \left\{ \Sigma_{g,\text{max}} (S_v + 1) \exp \left(-\frac{b^2}{2H_v^2} (S_v + 1) \right) \right. \\ &\quad \times \left. \left[\frac{S_v}{S_v + 1} - \frac{b^2 S_v}{2H_v^2} + \frac{1}{2} \right] + \frac{\Sigma_{g,\text{back}}(\varpi)}{2} \right\}. \end{aligned} \quad (4.61)$$

The first term of this equation represents the concentration of the dust particles within the vortex, it is only important for $b \lesssim H_v$. Equation (4.61) is approximated with a simple power law function of the form $\log n(a) = -p \log(a) + k$. The left and middle panels of Figure (4.17) show the slope p , the fractional standard deviation ($\Delta p/p$). The slope p decreases in the vortex and reaches a minimum value $p \sim 3.0$ at the vortex center. The fit is very good as shown by the low values of the fractional standard deviation.

Since the dust mass is dominated by the large grains, the local dust to gas mass ratio (ϵ_l) reduces to

$$\epsilon_l \approx \frac{\Sigma_d(a_{\text{max}})}{\Sigma_g}. \quad (4.62)$$

⁸This derivation differs from equation (4.45) because in this section the dust surface density was not integrated using a particle size distribution (as in equation 4.31), but it was approximated by the trace of the large dust grains, which dominate the dust mass.

This function is shown in the right panel of Figure (4.17), normalized to the total dust to gas mass ratio (ϵ_{global}). The maximum dust to gas mass ratio ($\epsilon_{l,\text{max}}$) is quite large at the vortex center, reaching a value $\epsilon_{l,\text{max}}/\epsilon_{\text{global}} \sim 10.5$. Note that the increase of the dust to gas mass ratio in the vortex center is due to the accumulation of dust grains from a small region around the vortex, while the rest of the disk remains with the standard ϵ_{global} value.

4.5.3 Synthetic observations

The CASA software (v 4.7.0)⁹ is used to simulate ALMA observations of the disk model shown in Figure (4.16) with the dust properties of Figure (4.17). We calculate the images at 1 and 3 mm for the configurations C4-6 (Band 7) and C4-8 (Band 4). The precipitable water vapor (PWV) was set to 1.3 and 1.5 mm in the Band 7 and Band 4 configuration, respectively. These antenna arrays provide a similar angular resolution $\theta_B \sim 0''10$, which corresponds to 12 au at the assumed distance of 120 pc.

The VLA observations are also simulated at 7 mm and 1 cm with CASA in the A configuration (the highest resolution). The FWHM beam of these configurations are $\theta_B \sim 0''043$ and $0''19$, respectively. In both simulations the PWV was set to 1.5 mm.

Figure (4.18) shows the ALMA simulated maps in the upper panels (left: 1 mm, right: 3 mm). Lower panels show the VLA maps (left: 7 mm, right: 1 cm). The vortex emission starts to show at 3 mm and becomes very evident at larger wavelengths, in the VLA images.

4.5.4 Effect of the Dust Concentration

Strong azimuthal asymmetries at mm wavelengths, as observed, e.g, in the OpH IRS 48 disk (van der Marel et al., 2013), are obtained in the disk models with a concentration of the dust particles around the vortex center, as shown in the Figure (4.18). The strong disk asymmetry comes from the enhancement of the dust to gas mass ratio due to size segregation inside the vortex, the opacity is increased by a factor of 10 at the vortex center. The smaller slope of the size distribution p within the vortex also increases the opacity at mm wavelengths (see Appendix A). For example, for $p = 3$ and $\lambda = 7$ mm, the opacity increases by a factor of ~ 1.8

⁹CASA, the Common Astronomy Software Applications package, is a software developed to support data processing of radio astronomical telescopes.

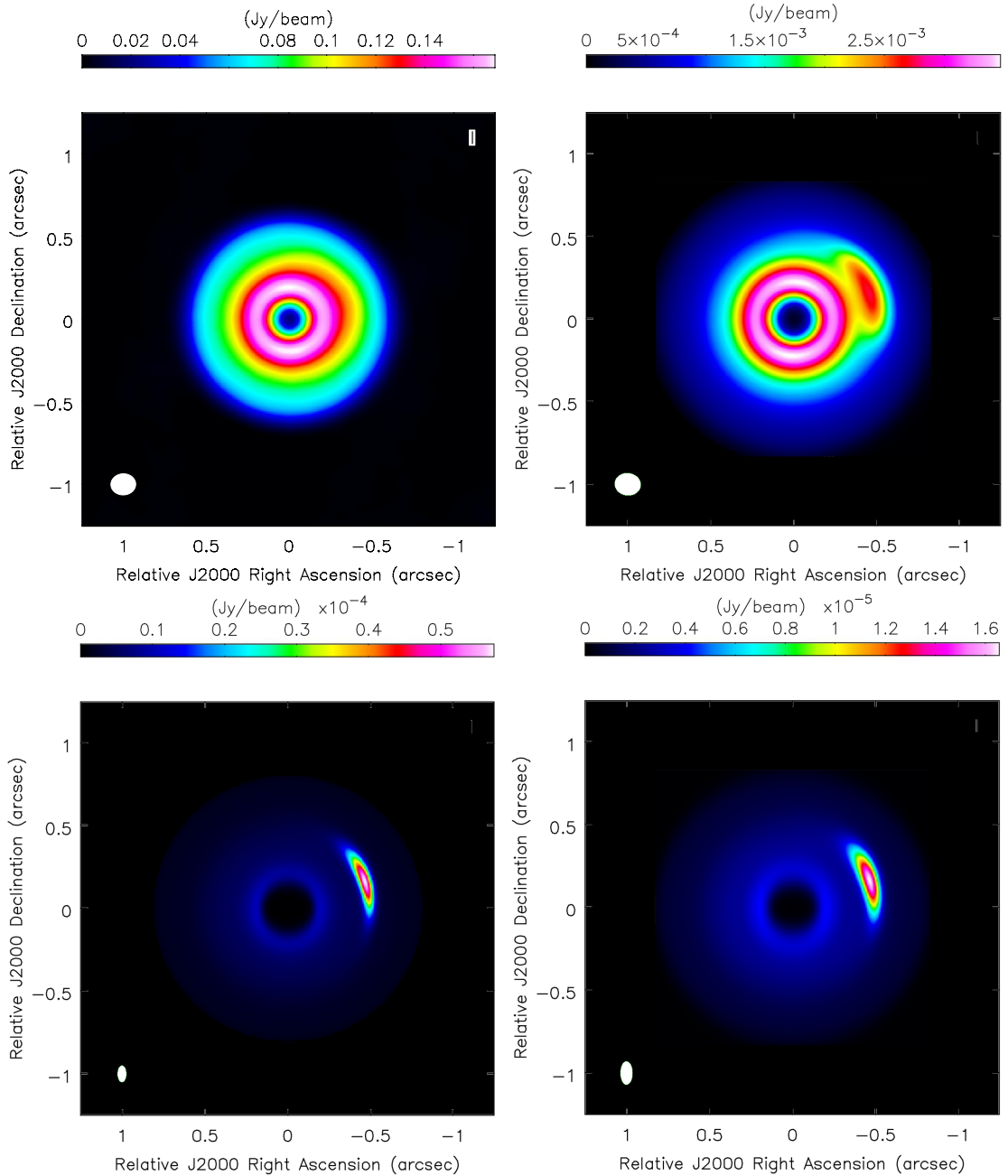


Figure 4.18: Upper panels: Simulated ALMA images at 1 mm (left) and 3 mm (right). Lower panels: Simulated VLA images at 7 mm (left) and 1 cm (right). The beam is shown in the left bottom corner of each image.

compared with the case $p = 3.5$. Both effects (higher dust to gas mass ratio and lower slope of the size distribution) are responsible for the increase of the opacity by a factor of 18 at the vortex center.

In order to explore the effect of dust concentration in the vortex, we made maps of the disk model at 1, 3, 7 mm and 1 cm assuming a constant dust to gas mass ratio of $\epsilon = 0.0131$ and a fixed slope of the dust particle size distribution $p = 3.5$ throughout the disk. These maps are shown in Figure (4.19) with the same observational parameters described in Section (4.5.3) and using the same color bar of Figure (4.18).

The ALMA maps at 1 and 3 mm do not change much from those in Figure (4.18) where segregation is taken into account. However, there is a dramatic change for the VLA observations at 7 mm and 1 cm. If the dust segregation is not included, the high contrast between the vortex and the disk vanishes.

In the model with dust segregation, the vortex dominates the emission at long wavelengths. For those wavelengths the disk becomes optically thin while the vortex remains optically thick due to the increase of the dust opacity in this region. Figure (4.20) shows the logarithm of the optical depth at 3, 7 mm and 1 cm. At 3 mm, all the disk is optically thick ($\log \tau_{3\text{mm}} > 0$). At 7 mm, the vortex is optically thick, but the rest of the disk becomes optically thin ($\log \tau_{7\text{mm}} < 0$). At 1 cm, the vortex still remains optically thick, while the background disk is optically thin. Therefore, dust segregation is a crucial ingredient to produce strong azimuthal asymmetries in the dust thermal emission at 7 mm and 1 cm. Note, however, that jets and photo-evaporated disk winds will also contribute to the 1 cm emission. Thus, high resolution images are necessary to distinguish the vortex at this wavelength (e.g. Macías et al. (2016)).

4.5.5 Absorption and Scattering

The contribution of the scattering coefficient to the total opacity was discussed in chapters 2 and 3. In this section we produce synthetic images without scattering to compare them with the results of the previous Section (4.5.3).

Figure (4.21) shows the simulated ALMA maps at 1 and 3 mm and the simulated VLA maps at 7 mm and 1 cm when only the absorption coefficient is included in the opacity, and using the same color bar of Figure (4.18). The 3 mm map shows a stronger azimuthal asymmetry compared with the 3 mm map of Figure (4.18). This occurs because the optical depth decreases by an order of magnitude making the background disk optically thin at 3 mm, 7 mm and 1 cm, while the vortex remains

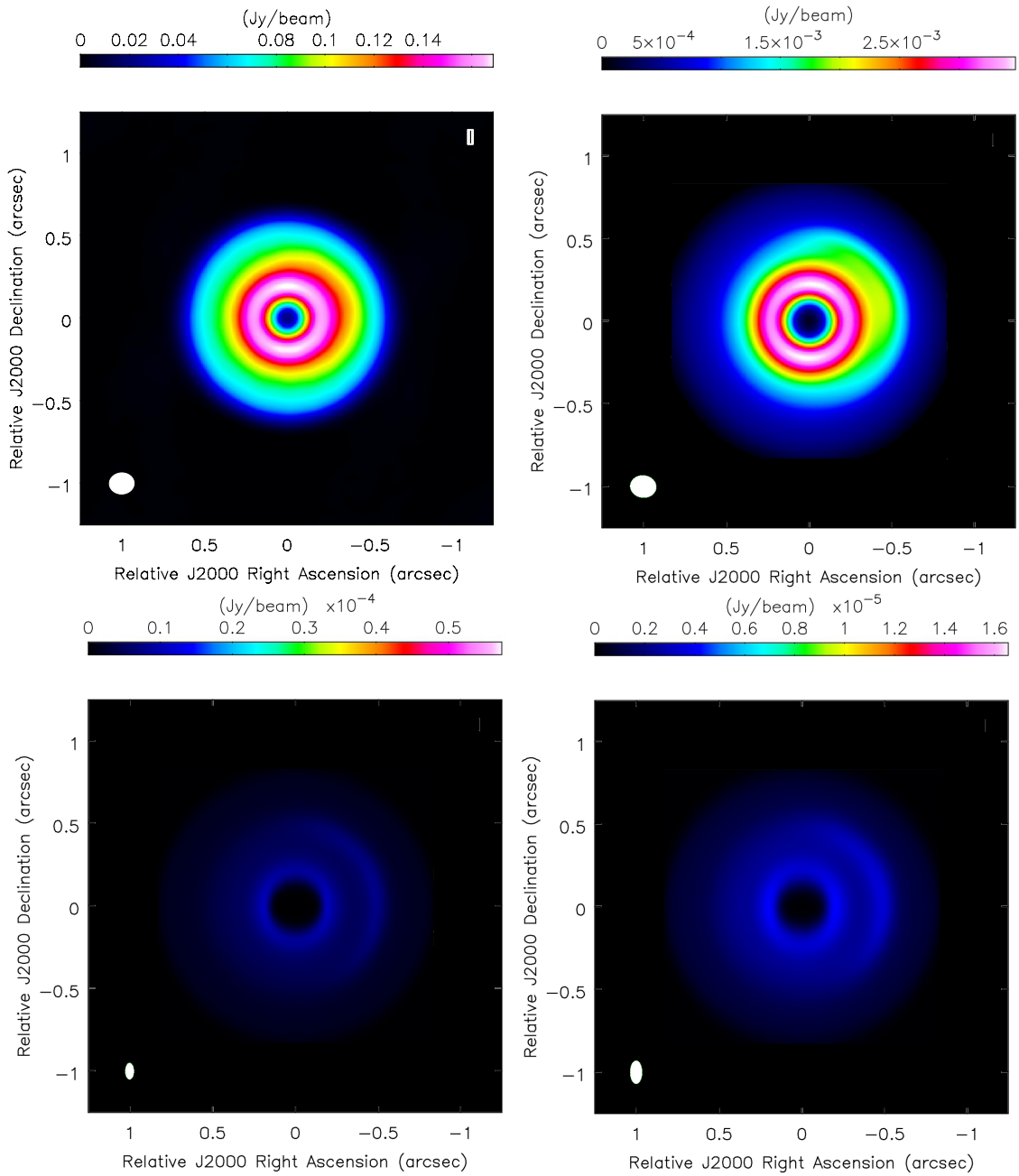


Figure 4.19: Upper panels: Simulated ALMA images at 1 mm (left) and 3 mm (right). Lower panels: Simulated VLA images at 7 mm (left) and 1 cm (right). These models do not include dust segregation inside the vortex (see text). The beam is shown in the left bottom corner of each image. The color bar of each map is the same as in Figure (4.18).

optically thick.

4.5.6 Maximum grain size

In the previous sections a_{\max} was set up to 1 mm; however, observational evidences suggest that the maximum grain size could reach $a_{\max} \sim 1$ cm (e.g., Pérez et al.

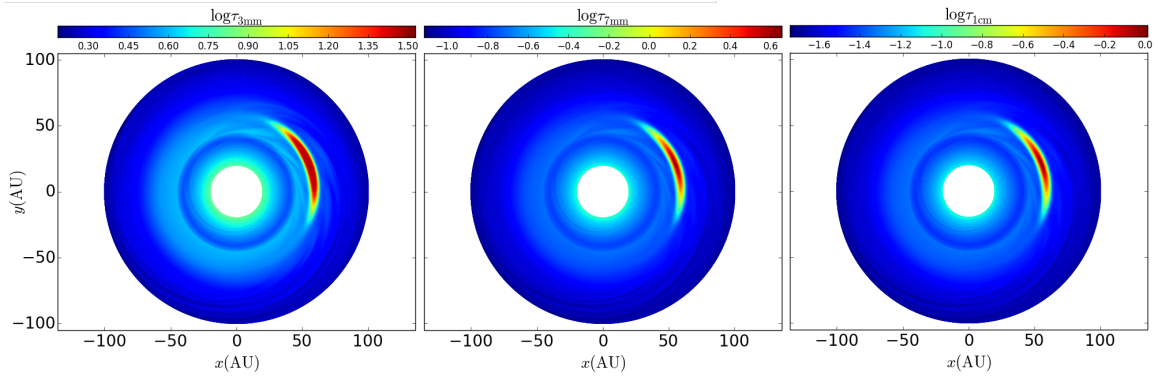


Figure 4.20: Logarithm of the optical depth of the disk at 3 mm (left), 7 mm (middle), and 1 cm (right).

2015). Figure (4.22) shows the dust properties when $a_{\max} = 1$ cm. The slope p does not change significantly compared to the previous model ($a_{\max} = 1$ mm). However, the maximum dust to gas mass ratio within the vortex is 7 times larger. This happens because 1 cm grains are more concentrated toward the vortex center since they have a Stokes number 10 times larger than 1 mm grains (equation 4.47).

Dust opacity also depends on a_{\max} (see Appendix A). For $a_{\max} = 1$ cm the opacity at 1, 3, 7 mm, and 1 cm is modified by a factor of 0.40, 0.55, 5.6, 20, respectively, compared with the case of $a_{\max} = 1$ mm. This means that at 7 mm and 1 cm the vortex emission will dominate the disk emission, but will have a small spatial extent, due to the strong dust concentration. At 1, 3 mm, the increase of the dust to gas mass ratio can overcome the decrease of the opacity; however, the background disk remains optically thick, thus, one expects maps similar to those in Figure (4.18).

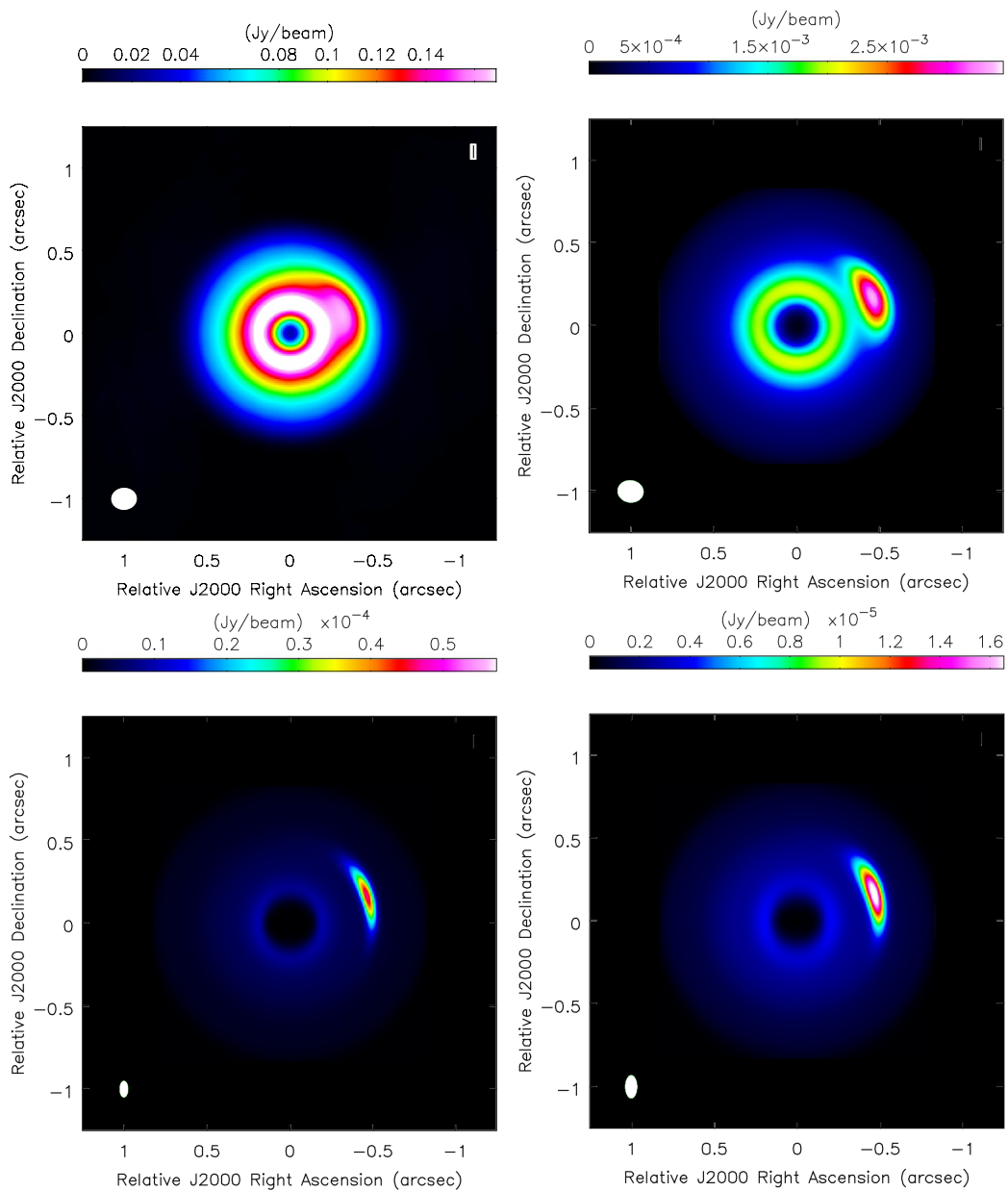


Figure 4.21: Upper panels: Simulated ALMA images at 1 mm (left) and 3 mm (right). Lower panels: Simulated VLA images at 7 mm (left) and 1 cm (right). For these maps the albedo is set to $\omega_\nu = 0$. The color bar of each map is the same as in Figure (4.18).

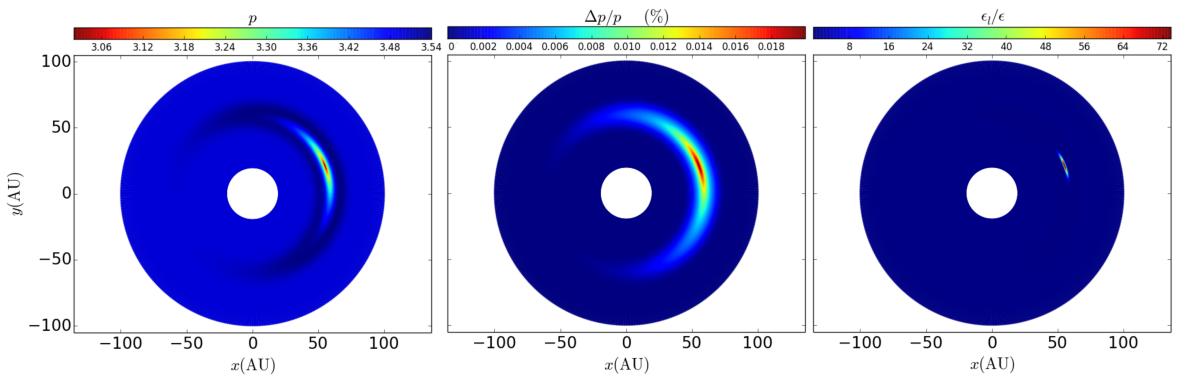


Figure 4.22: Dust particle accumulation within the vortex for $a_{\max} = 1$ cm. Left panel: Slope p of the power law fit to the dust particle size distribution $n(a)da \propto a^{-p}da$ (see text). Middle panel: fractional standard deviation $\Delta p/p$. Right panel: Map of the local dust to gas mass ratio (normalized to ϵ).

Chapter 5

Conclusions

Different physical processes taking place in protoplanetary disks are responsible of creating complex sub-structures in the disks. Mechanisms like dust migration, settling, dust traps, dust growth, turbulent mixing, photo-evaporation, accretion, dust-gas interactions, and planet formation are fundamental to explain the observed substructures and the disk evolution.

Our understanding of protoplanetary disks during the last decade has had a fast growth due to the high angular resolution observations with ALMA and VLA, which have revealed that most of the disks observed at an angular resolution better than ~ 10 au have radial and azimuthal structures such as rings, gaps, vortices, and/or spiral arms; and they are far from smooth.

Probably, the most peculiar and important process in protoplanetary disks is dust growth, from which the formation of planets is initiated. The typical grain sizes in disks (\sim mm, cm), compared with those in the interstellar medium ($\sim \mu\text{m}$), have important effects in the scattered light, specially when the disks are observed at radio frequencies, where the dust opacity could be dominated by scattering. For this reason, a correct analysis of the light captured by radio telescopes should be addressed in order to appropriately infer the disks properties.

This thesis studies the inclusion of the scattering opacity in the radiative transfer equation, in order to compute its effects and correctly apply them when simulating synthetic observations at mm wavelengths of disks with radial and azimuthal morphologies.

From these studies, we found and confirm previous studies that suggested that the scattering coefficient is much larger than the absorption coefficient at millimeter wavelengths if the dust grains have mm-cm sizes, even if the scattering coefficient decreases due to the non-isotropic scattering. The albedo is close to 1 for grains with a size $a \sim \lambda/2\pi$. Then, a realistic radiative transfer solution for protoplanetary

disks should not neglect the scattering effects.

When scattering is taken into account, we found that it modifies the emergent intensity (compared with the true absorption case) in protoplanetary disk with large albedo ($\omega_\nu \gtrsim 0.6$). In the optically thick regime (no matter the wavelength), the emergent intensity can decrease by a factor of 4. For intermediate optical depths $-2 \lesssim \log(\tau_{\kappa_\nu}) \lesssim -1$, it increases by a factor of 2, while in the optically thin regime the emergent intensity is not modified from the true absorption case.

These changes in the emergent intensity due to the scattering effects modify the inferred spectral indices at millimeter wavelengths compared with the true absorption case. The spectral index in the scattering and true absorption case coincide for all wavelengths only in optically thin case ($\log(\tau_{\kappa_{1.3\text{mm}}}) \lesssim -2$). The spectral indices are modified at large optical depths. In particular, spectral indices smaller than 2 can be obtained for optically thick disks and dust grains with sizes between $100 \mu\text{m}$ and 1 mm.

The changes in the spectral indices also have an impact on the shape of the spectral energy distribution (SED) when the albedo is large ($\omega_\nu \gtrsim 0.6$) and the optical depth is $\log(\tau_{\kappa_\nu}) \gtrsim -2$. The effects of the scattering on the SED depend on the inclination of the disk with respect to the plane of the sky because more inclined disks are optically thicker than face-on disks.

During many works, an usual method to fit the properties of protoplanetary disks has been to use a modified grey body model which does not consider the scattered light. We point out that neglecting the scattering effects on the radiative transfer of protoplanetary disks can lead to a wrong interpretation of an excess emission at optically thin millimeter wavelengths (e.g. $\lambda = 7 \text{ mm}$). For example, the incorrect interpretation of the observed SED as a true absorption case, would imply an excess emission of around 70% for a disk with $a_{\max} = 1 \text{ mm}$ and $\log(\tau_{\kappa_{1.3\text{mm}}}) = 1.3$. When scattering is taken into account, the anomalous spectral index between ALMA and VLA wavelengths, $\alpha_{3.0-7.0\text{mm}}^{\text{obs}}$, reported in several sources, could be explained by optically thick disks ($\log(\tau_{\kappa_{1.3\text{mm}}}) \gtrsim 1$) and dust grain sizes between $300 \mu\text{m} \lesssim a \lesssim 1 \text{ mm}$.

In order to show how the analytical solution to the radiative transfer equation with scattering effects can be used to explain the properties of protoplanetary disks, we focus on the multi wavelength observations of the HL Tau disk at radio frequencies. From this study, we found that a gradient in the maximum grain size as a function of the disk radius is inferred from the best fit models: large grains ($a_{\max} \approx 1 \text{ mm}$) in the center of the disk ($\varpi < 40 \text{ au}$) and small grains ($a_{\max} < 1 \sim \text{mm}$) in the outer disk ($\varpi > 40 \text{ au}$). Additionally, variations in the maximum grain size in the

dark and bright rings are also inferred. Most of the dark rings have small grains and small dust surface density, while the bright rings have large grains and large dust surface density. The ring at 21 au is associated to a maximum in the dust surface density but a minimum of the maximum grain size.

We note that the origin of the inner rings and gaps in the HL Tau disk can be associated to the ice lines of different molecules (which changes the fragmentation and sticking properties of the dust). This is not the case of the wide outer gap between 67 and 77 au, where both the dust surface density and the maximum grain size are low and have a local minimum. This gap can be created by the presence of a planet, as suggested by other authors.

Once the effects of the scattering on the radiative transfer equations were studied, we focus on the dust dynamics that could explain some of the radial and azimuthal asymmetries found in many protoplanetary disks. First we found a radial dust trap model that can explain the behavior of the dust grains trapped in gas rings of simulations such as the ones performed by Flock et al. (2015) and Ruge et al. (2016), and then it is used to explain the main characteristics of the thermal dust emission of the disk around the HD 169142 star. This radial dust trap model can be easily implemented in numerical simulations that follow only the gas in protoplanetary disks to account for the dust concentration, saving computational time.

The model is based on the equilibrium between the drag force and diffusion, which tends to accumulate dust grains in the gas pressure maxima and prevents the dust migration toward the central star. The redistribution of dust grains can effectively increase the dust-to-gas mass ratio and the thermal dust emission within the gas pressure maxima.

When this model is applied to the HD 169142 disks, we found that the small spectral index derived from the ALMA observations in the inner ring ($10 \lesssim \varpi \lesssim 40$ au) can be explained by the presence of large grains. The maximum dust size in the center of the inner ring (~ 27 au) is $a_{\max} > 10$ cm if the slope of the particle size distribution of $p = 3.5$. However, the maximum grain size decreases to ~ 3 mm, 1 mm if the slope of the particle size distribution is $p = 3.0, 2.5$ respectively.

From the model, we find that the global dust-to-gas mass ratio in the HD 169142 disk is $\epsilon_{\text{global}} = (1.05^{+0.15}_{-0.13}) \times 10^{-2}$ (similar to the ISM), and the viscosity coefficient (which controls the degree of dust trapping) is $\alpha_t = (1.35^{+0.51}_{-0.85}) \times 10^{-2}$. These parameters can simultaneously explain the dust emission radial profiles at $\lambda = 870 \mu\text{m}$, 1.3 mm, and 3.0 mm.

Finally, we focus on the properties of the azimuthal dust trapping in protoplanetary disks. We extend the Lyra-Lin solution for the dust concentration of a single

grain size to a power-law distribution of grain sizes $n(a)da \propto a^{-p}da$. Assuming dust conservation in the disk, we find an analytic dust surface density as a function of the grain radius. We calculate the increase of the dust to gas mass ratio ϵ and the slope p of the dust size distribution due to grain segregation within the vortex.

We apply this model to a numerical simulation of a disk containing a persistent vortex and found that dust segregation and concentration inside a vortex can significantly increase the local dust-to-gas mass ratio ϵ_l inside the vortex; the maximum $\epsilon_{l,\max}/\epsilon \sim 10$ is reached in the vortex center. This high value occurs due to the concentration in the vortex center of sub-mm and mm particles that dominate the mass distribution.

Also, from the model we find that the slope of the dust size distribution is less than the standard value ($p = 3.5$); the slope has a minimum close to the vortex center with $p \sim 3$. This change of slope affects both the absorption and scattering coefficients of the dust population and tends to increase the contrast between the vortex and the background disk in the dust millimeter emission.

However, the main effect that causes the strong azimuthal asymmetries is the increase of the dust-to-gas mass ratio. It enhances the azimuthal asymmetries in the millimeter emission by one order of magnitude at $\lambda = 7$ mm and 1 cm (optically thin disks).

These strong asymmetries are not found if one only considers the effect of an increase of the dust surface density within the vortex using a constant dust-to-gas mass ratio ϵ . In this case, the vortex region does not dominate the emission of the disk at mm wavelengths. The main difference is that when dust segregation is included, the vortex remains optically thick even at long wavelengths, but the rest of the disk becomes optically thin.

As mentioned or suggested during almost all the sections of this thesis, the properties of protoplanetary disks are not yet fully understood, but it is probably one of the fields in the astronomy with the most level of complexity and details. Most of the works and authors are capable to explain small differences in the dust and gas properties in the disk due to the high angular resolution observations, far from the power-law functions that were first proposed to explain these objects.

It is exciting to think about what we will be able to observe and explain in the future with more and better observations.

Appendix A

Opacity properties

The Mie theory (2.2) is used to compute the absorption coefficient $\kappa_\nu(a)$, the single scattering coefficient $\sigma_\nu^{\text{single}}(a)$, and the asymmetry parameter $g_\nu(a)$ for each dust grain size at millimeter wavelengths. The extinction coefficient $\chi_\nu(a)$ and the effective scattering coefficient $\sigma_\nu(a)$ are found using the equations (2.1, 2.3). These properties are shown in Figure (2.2).

Then, the opacity coefficients and the albedo are found using equations (2.7, 2.8) by assuming that the particle size distribution is given by $n(a)da \propto a^{-p}da$, between a minimum grain size $a_{\min} = 0.05 \mu\text{m}$ and a maximum grain size a_{\max} . The opacity spectral indices are then found using equations (2.9-2.11).

The slope of the particle size distribution and the maximum grain size have important effects on the opacity coefficients (Draine, 2006), then we set a parameter space of p and a_{\max} which vary from $2 < p < 4$, and $10 \mu\text{m} < a_{\max} < 10 \text{ cm}$, in order to compute the dust opacity properties.

These opacity properties (opacity spectral indices, opacity coefficients, and albedo) as a function of p and a_{\max} are shown in the following figures at different wavelengths. During the thesis, the dust properties usually corresponds to slices of these plots at constant $p = 3.5$ (ISM). These curves were shown in Figure (2.4).

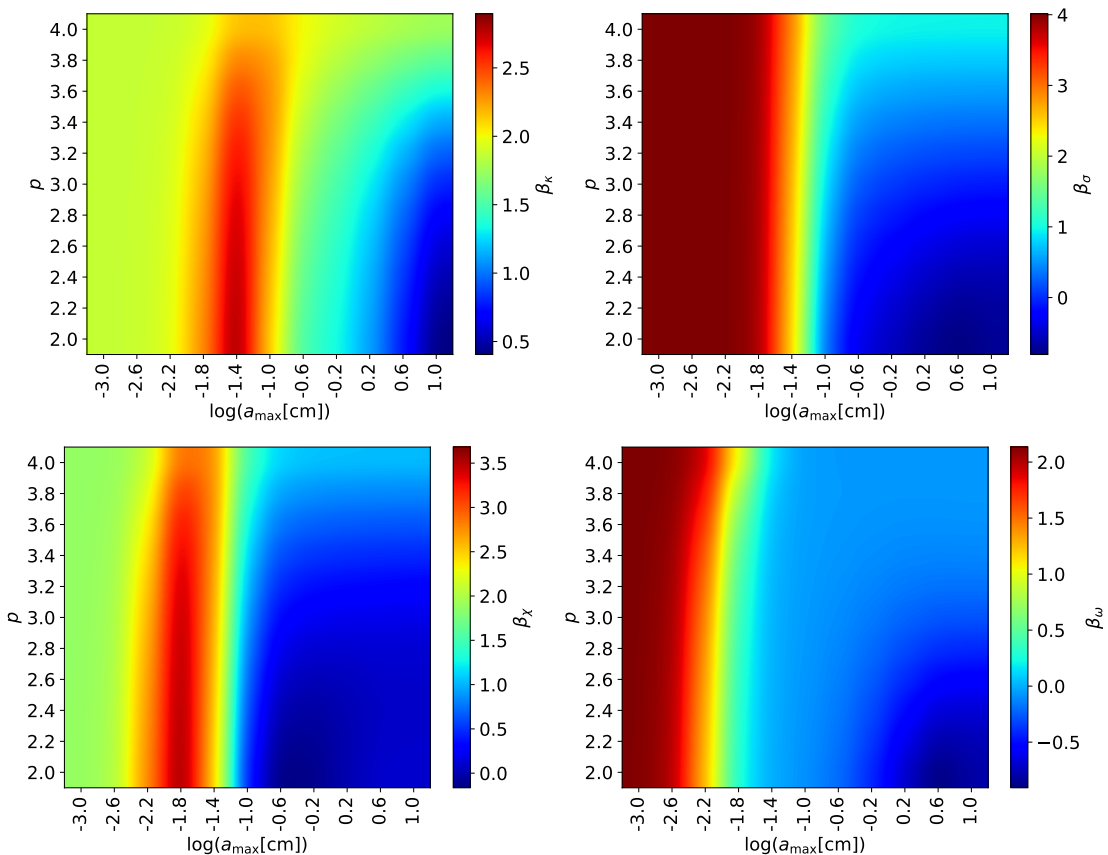


Figure A.1: Opacity spectral index as a function of the slope of the particle size distribution p and the maximum grain size a_{\max} . Top left: β_κ , top right: β_σ , bottom left: β_χ , bottom right: β_ω .

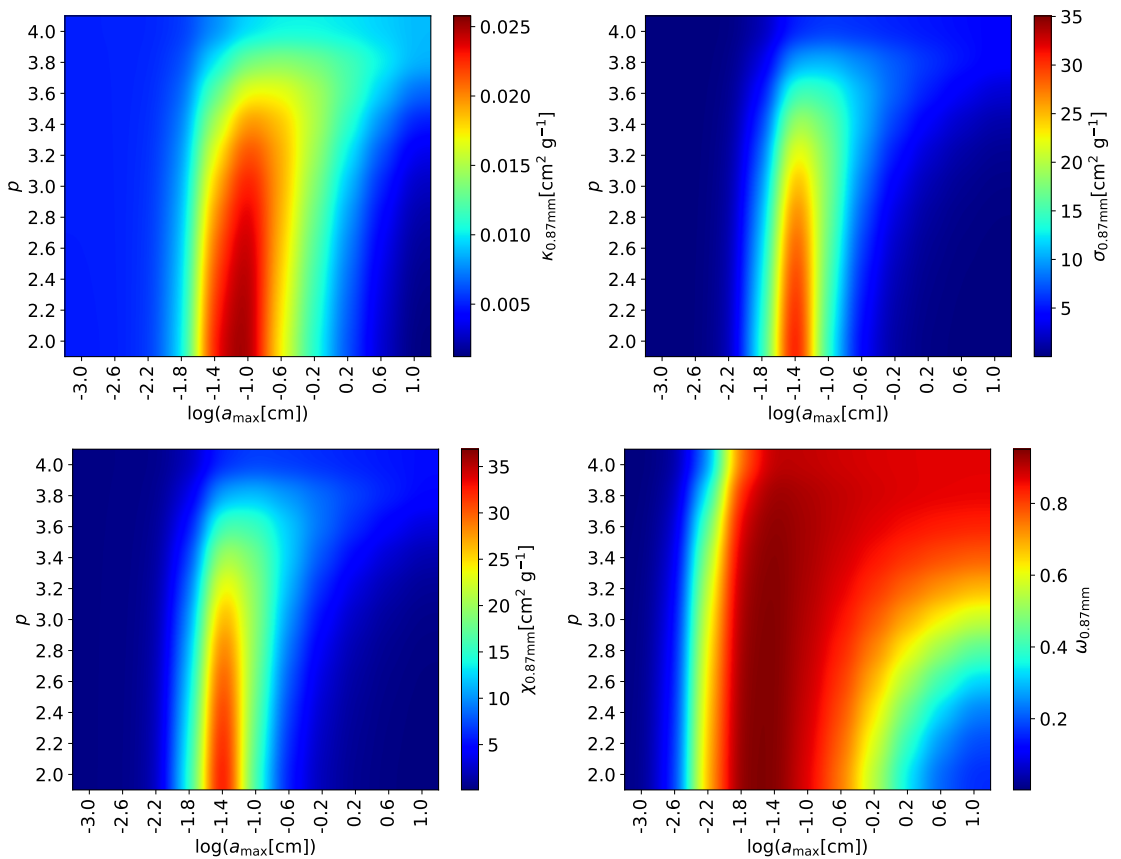


Figure A.2: Opacity properties as a function of the slope of the particle size distribution p and the maximum grain size a_{\max} at $\lambda = 0.87$ mm ($\nu = 345$ GHz, ALMA Band 7). Top left: absorption coefficient, top right: scattering coefficient, bottom left: extinction coefficient, bottom right: albedo.

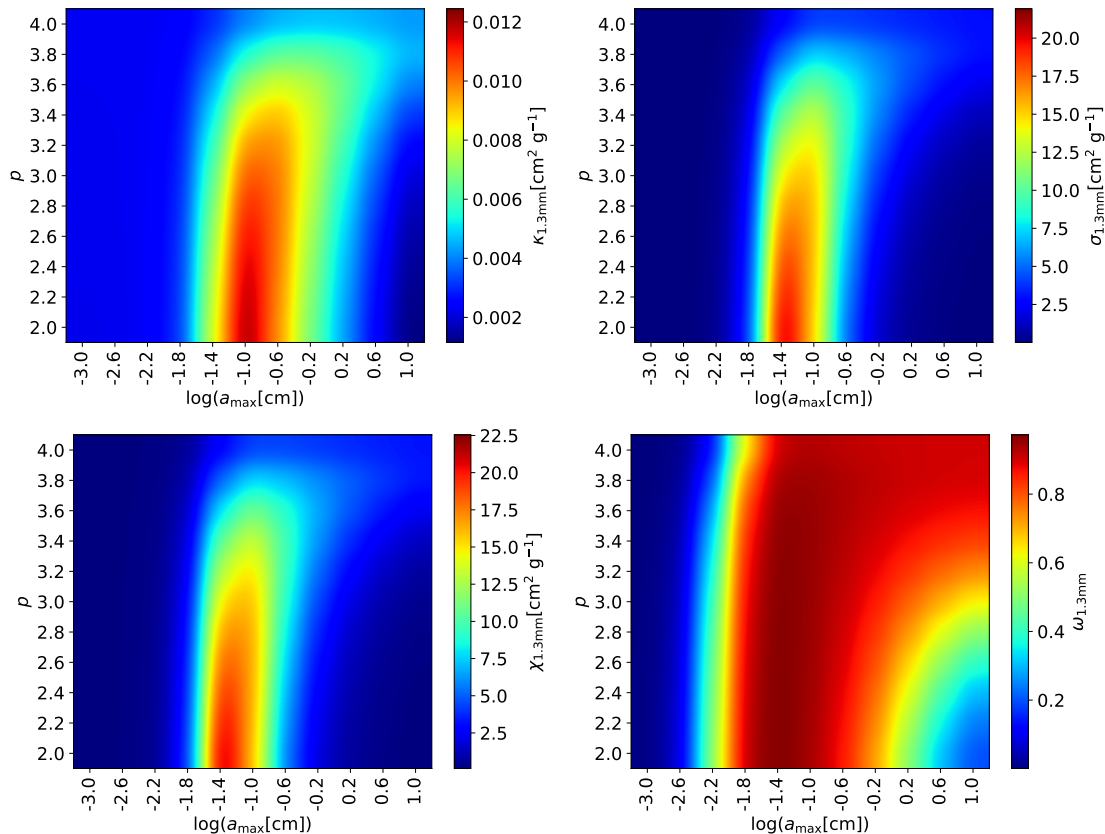


Figure A.3: Opacity properties as a function of the slope of the particle size distribution p and the maximum grain size a_{\max} at $\lambda = 1.3$ mm ($\nu = 230$ GHz, ALMA Band 6). Top left: absorption coefficient, top right: scattering coefficient, bottom left: extinction coefficient, bottom right: albedo.

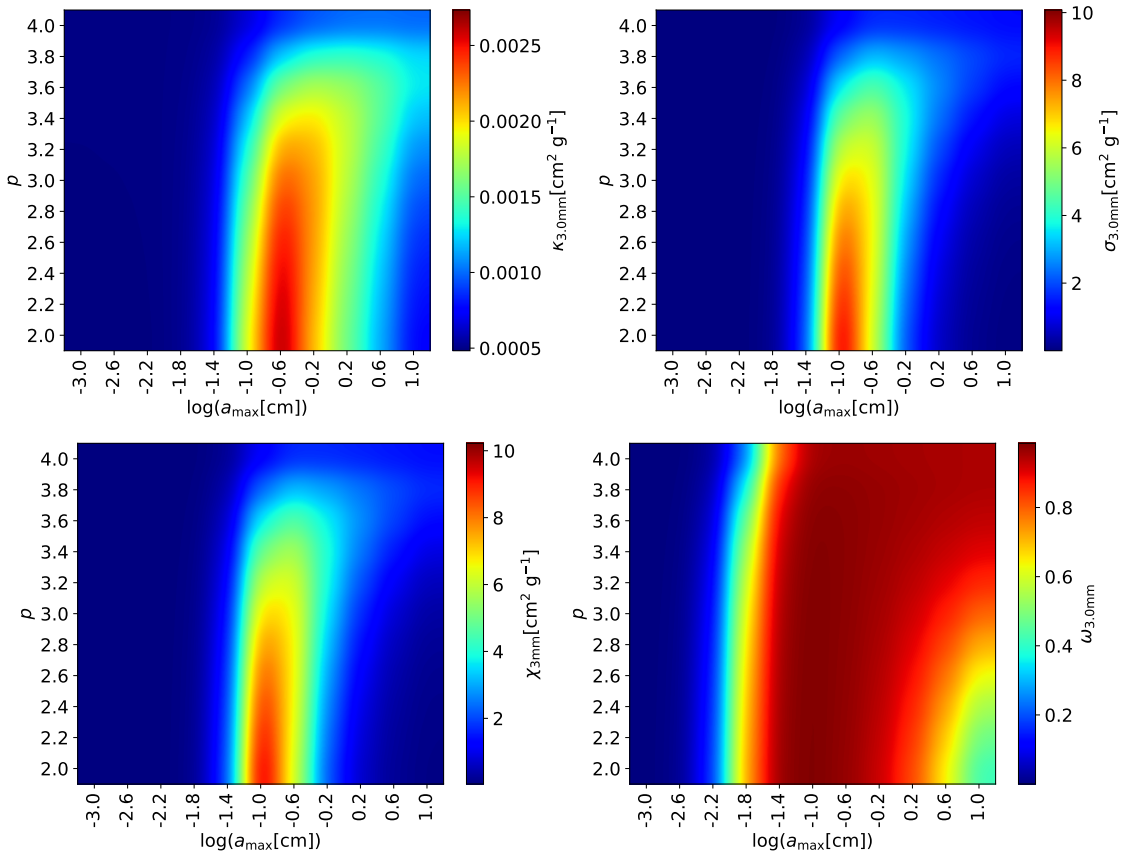


Figure A.4: Opacity properties as a function of the slope of the particle size distribution p and the maximum grain size a_{\max} at $\lambda = 3$ mm ($\nu = 100$ GHz, ALMA Band 3). Top left: absorption coefficient, top right: scattering coefficient, bottom left: extinction coefficient, bottom right: albedo.

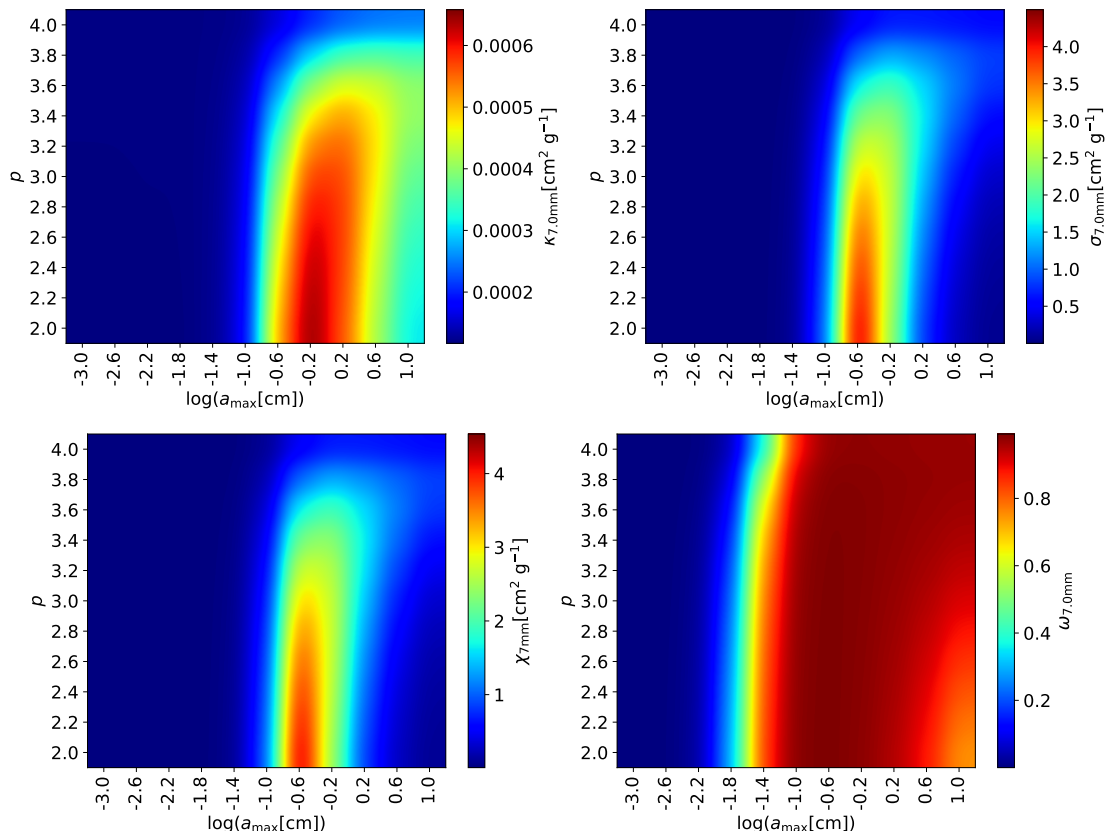


Figure A.5: Opacity properties as a function of the slope of the particle size distribution p and the maximum grain size a_{\max} at $\lambda = 7$ mm ($\nu = 42$ GHz, VLA Band Ka). Top left: absorption coefficient, top right: scattering coefficient, bottom left: extinction coefficient, bottom right: albedo.

Appendix B

Gas and dust timescales

The dynamics of the gas and dust grains is different due to the drag force. In particular, the advection timescale of the dust grains is

$$t_{\text{adv,d}} = \frac{L}{v_\varpi}, \quad (\text{B.1})$$

where L is a characteristic length scale and v_ϖ is the magnitude of the dust velocity relative to the gas (equation 4.24). The diffusion timescale of the gas and the dust grains are

$$t_{\text{diff,g}} = \frac{L^2}{D_g}, \quad (\text{B.2})$$

$$t_{\text{diff,d}} = \frac{L^2}{D_g} (1 + St^2), \quad (\text{B.3})$$

where D_g is the gas diffusion coefficient and St the Stokes number ([Youdin & Lithwick, 2007](#)). Then, the ratio between the diffusion and advection timescales of the dust is given by

$$\frac{t_{\text{diff,d}}}{t_{\text{adv,d}}} = \frac{St}{\alpha} \left| \frac{\varpi}{\Sigma_g} \frac{d\Sigma_g}{d\varpi} \right|, \quad (\text{B.4})$$

If this ratio is much larger than 1, the dust concentrates in pressure maxima. The ratio between the diffusion timescale of the gas and the dust advection timescale is

$$\frac{t_{\text{diff,g}}}{t_{\text{adv,d}}} = \frac{St}{\alpha} \left(\frac{1}{1 + St^2} \right) \left| \frac{\varpi}{\Sigma_g} \frac{d\Sigma_g}{d\varpi} \right|. \quad (\text{B.5})$$

If this ratio is much larger than 1, as the gas evolves, the dust quickly adjusts to the gas density structure and concentrates in gas pressure maxima. In general, the Stokes number for millimeter and centimeter dust grains ($St(1 \text{ mm}) \sim 0.1$, $St(1 \text{ cm}) \sim 1$).

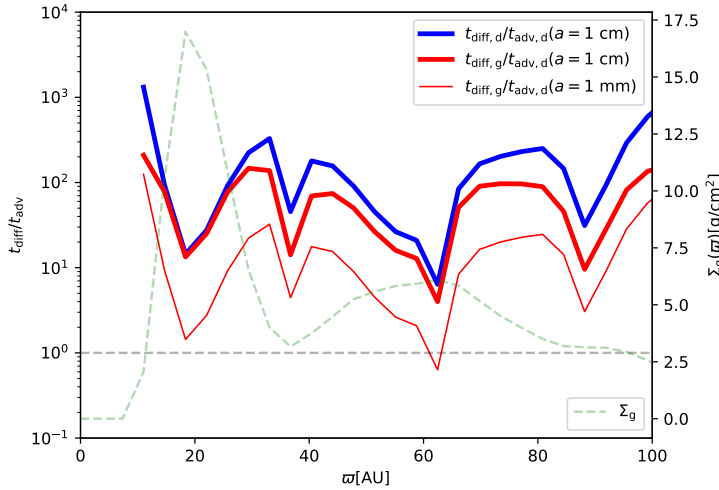


Figure B.1: Ratio of the diffusion and advection timescales as a function of radius for the HD 169142 disk. The thick blue line is the dust diffusion to advection timescales ratio for grains of 1 cm. The thick and thin red lines are the ratio of the gas diffusion to the dust advection timescales for 1 cm and 1 mm, respectively. The gas surface density is shown for reference in the background as a green dotted line.

Also, the logarithmic density gradient in accretion disks $|(\partial \ln \Sigma_g / \partial \ln \varpi)|$ is in general, of the order of 1, but in pressure maxima, it is much larger than 1. For example, consider a gaussian function at a radius ϖ_0 and a total width 2σ , $\Sigma_g \propto \exp(-\frac{1}{2}(\varpi - \varpi_0)^2/\sigma^2)$. Then, the logarithmic gradient is $\varpi |(\varpi - \varpi_0)|/\sigma^2$. For narrow rings such that $\epsilon = 2\sigma/\varpi_0 < 1$, the logarithmic gradient is larger than 1, except in the neighborhood of ϖ_0 where the dust grains are already close to the equilibrium point. Then, because the viscosity coefficient α is much smaller than 1, the advection timescale of the dust grains is smaller than the diffusion timescale of both the gas and dust, allowing a fast concentration of the dust grains in the gas pressure maxima.

Figure (B.1) shows the ratio between the diffusion and advection timescales for the best fit model of the HD 169142 disk . The different lines show these ratios for dust sizes of 1 cm and 1mm. Because the Stokes number for 1mm particles is small, the ratio of the dust diffusion to advection timescales and the ratio of the gas diffusion to the dust advection timescales are the same. Note that the ratios between the timescales are larger than 1 throughout the disk, with local minima at the position of the gas maxima, where the dust grains concentrate. Thus, a fast trapping scenario and the steady state assumption are feasible in the HD 169142 disk.

Bibliography

- Adams, F. C., Lada, C. J., & Shu, F. H. 1987, ApJ, 312, 788
- Akiyama, E., Hashimoto, J., Liu, H. B., et al. 2016, AJ, 152, 222
- ALMA Partnership, Brogan, C. L., Pérez, L. M., et al. 2015, ApJ, 808, L3
- Andre, P., Ward-Thompson, D., & Barsony, M. 1993, ApJ, 406, 122
- Andrews, S. M., Wilner, D. J., Hughes, A. M., et al. 2009, ApJ, 700, 1502
- Andrews, S. M., Wilner, D. J., Zhu, Z., et al. 2016, ApJ, 820, L40
- Andrews, S. M., Huang, J., Pérez, L. M., et al. 2018, ApJ, 869, L41
- Ansdell, M., Williams, J. P., & Cieza, L. A. 2015, ApJ, 806, 221
- Ansdell, M., Williams, J. P., van der Marel, N., et al. 2016, ApJ, 828, 46
- Armitage, P. J. 2007, arXiv e-prints, astro-ph/0701485
- Armitage, P. J. 2010, Astrophysics of Planet Formation, by Philip J. Armitage, pp. 294. ISBN 978-0-521-88745-8 (hardback). Cambridge, UK: Cambridge University Press, 2010., 294
- Bae, J., Zhu, Z., & Hartmann, L. 2017, ApJ, 850, 201
- Bae, J., & Zhu, Z. 2018, ApJ, 859, 118
- Balbus, S. A., & Hawley, J. F. 1991, ApJ, 376, 214
- Barge, P., & Sommeria, J. 1995, A&A, 295, L1
- Barge, P., Richard, S., & Le Dizès, S. 2016, A&A, 592, A136
- Barge, P., Ricci, L., Carilli, C. L., & Previn-Ratnasingam, R. 2017, A&A, 605, A122
- Beckwith, S. V. W., & Sargent, A. I. 1991, The Astrophysical Journal, 381, 250
- Benisty, M., Juhasz, A., Boccaletti, A., et al. 2015, A&A, 578, L6
- Biller, B. A., Males, J., Rodigas, T., et al. 2014, ApJ, 792, L22
- Birnstiel, T., Ormel, C. W., & Dullemond, C. P. 2011, A&A, 525, A11

- Birnstiel, T., Dullemond, C. P., & Pinilla, P. 2013, A&A, 550, L8
- Birnstiel, T., Dullemond, C. P., Zhu, Z., et al. 2018, ApJ, 869, L45
- Blondel, P. F. C., & Djie, H. R. E. T. A. 2006, A&A, 456, 1045
- Blum, J., Wurm, G., Kempf, S., et al. 2000, Phys. Rev. Lett., 85, 2426
- Bohren, C. F., & Huffman, D. R. 1983, New York: Wiley
- Brauer, F., Dullemond, C. P., & Henning, T. 2008, A&A, 480, 859
- Brown, J. M., Blake, G. A., Qi, C., et al. 2009, ApJ, 704, 496
- Burrows, C. J., Stapelfeldt, K. R., Watson, A. M., et al. 1996, ApJ, 473, 437
- Calvet, N., Briceño, C., Hernández, J., et al. 2005, AJ, 129, 935
- Carrasco-González, C., Henning, T., Chandler, C. J., et al. 2016, ApJ, 821, L16
- Carrasco-González, C., Sierra, A., Flock, M., et al. 2019, ApJ, 883, 71
- Casassus, S., van der Plas, G., M, S. P., et al. 2013, Nature, 493, 191
- Casassus, S., Marino, S., Lyra, W., et al. 2019, MNRAS, 483, 3278
- Chiang, E. I., & Goldreich, P. 1997, ApJ, 490, 368
- D'Alessio, P., Cantö, J., Calvet, N., et al. 1998, ApJ, 500, 411
- D'Alessio, P., Calvet, N., & Hartmann, L. 2001, ApJ, 553, 321
- Dickman, R. L. 1978, ApJS, 37, 407
- Dipierro, G., & Laibe, G. 2017, MNRAS, 469, 1932
- Dipierro, G., Ricci, L., Pérez, L., et al. 2018, MNRAS, 475, 5296
- Draine, B. T. 2003, ARA&A, 41, 241
- Draine, B. T. 2006, ApJ, 636, 1114
- Dong, R., Li, S., Chiang, E., et al. 2018, ApJ, 866, 110
- Dubrulle, B., Morfill, G., & Sterzik, M. 1995, Icarus, 114, 237
- Dullemond, C. P., & Dominik, C. 2005, A&A, 434, 971
- Dullemond, C. P., Birnstiel, T., Huang, J., et al. 2018, ApJ, 869, L46.
- Dutrey, A., Guilloteau, S., & Simon, M. 1994, A&A, 286, 149
- Eisner, J. A., Bally, J. M., Ginsburg, A., et al. 2016, ApJ, 826, 16
- Estalella, R., Anglada, G., 1994, ISBN 84-8338-098-6

- Fedele, D., Carney, M., Hogerheijde, M. R., et al. 2017, A&A, 600, A72
- Flock, M., Ruge, J. P., Dzyurkevich, N., et al. 2015, A&A, 574, A68
- Gaia Collaboration, Brown, A. G. A., Vallenari, A., et al. 2016, A&A, 595, A2
- Galli, P. A. B., Loinard, L., Ortiz-Léon, G. N., et al. 2018, ApJ, 859, 33
- Galván-Madrid, R., Liu, H. B., Izquierdo, A. F., et al. 2018, ApJ, 868, 39
- Grady, C. A., Muto, T., Hashimoto, J., et al. 2013, ApJ, 762, 48
- Güttler, C., Blum, J., Zsom, A., et al. 2010, A&A, 513, A56
- Hayashi, C. 1981, Progress of Theoretical Physics Supplement, 70, 35
- Henyey, L. G., & Greenstein, J. L. 1941, The Astrophysical Journal, 93, 70
- Hoang, T., Lan, N.-Q., Vinh, N.-A., et al. 2018, ApJ, 862, 116
- Hughes, A. M., Wilner, D. J., Qi, C., et al. 2008, ApJ, 678, 1119
- Inaba, S., & Barge, P. 2006, ApJ, 649, 415
- Isella, A., Testi, L., Natta, A., et al. 2007, A&A, 469, 213
- Isella, A., Natta, A., Wilner, D., et al. 2010, ApJ, 725, 1735
- Isella, A., Pérez, L. M., Carpenter, J. M., et al. 2013, ApJ, 775, 30
- Isella, A., Guidi, G., Testi, L., et al. 2016, Physical Review Letters, 117, 251101
- Kataoka, A., Tanaka, H., Okuzumi, S., et al. 2013, A&A, 557, L4
- Kataoka, A., Okuzumi, S., Tanaka, H., et al. 2014, A&A, 568, A42
- Kataoka, A., Muto, T., Momose, M., et al. 2015, ApJ, 809, 78
- Koerner, D. W., Sargent, A. I., & Beckwith, S. V. W. 1993, Icarus, 106, 2
- Kruegel, E. 2003, The physics of interstellar dust
- Li, H., Colgate, S. A., & Lovelace, R. V. E. 2000, Bulletin of the American Astronomical Society, 32, 02.15
- Liu, H. B. 2019, ApJ, 877, L22
- Loomis, R. A., Öberg, K. I., Andrews, S. M., et al. 2017, ApJ, 840, 23
- Lynden-Bell, D., & Pringle, J. E. 1974, MNRAS, 168, 603
- Lyra, W., & Lin, M.-K. 2013, ApJ, 775, 17
- Macías, E., Anglada, G., Osorio, M., et al. 2016, ApJ, 829, 1

- Macías, E., Anglada, G., Osorio, M., et al. 2017, *ApJ*, 838, 97
- Macias, E., Espaillat, C., Osorio, M., et al. 2019, arXiv e-prints, arXiv:1907.07277
- Marino, S., Casassus, S., Perez, S., et al. 2015, *ApJ*, 813, 76
- Mathis, J. S., Rumpl, W., & Nordsieck, K. H. 1977, *ApJ*, 217, 425
- Matthews, B. C., Sibthorpe, B., Kennedy, G., et al. 2010, *A&A*, 518, L135
- Miley, J. M., Panić, O., Haworth, T. J., et al. 2019, *MNRAS*, 485, 739
- Miyake, K., & Nakagawa, Y. 1993, *Icarus*, 106, 20
- Mouillet, D., Lagrange, A. M., Augereau, J. C., et al. 2001, *A&A*, 372, L61
- Muto, T., Grady, C. A., Hashimoto, J., et al. 2012, *ApJ*, 748, L22
- Natta, A., & Testi, L. 2004, Star Formation in the Interstellar Medium: In Honor of David Hollenbach, 279
- Natta, A., Testi, L., Calvet, N., et al. 2007, Protostars and Planets V, 767
- Okuzumi, S., Momose, M., Sirono, S.-. iti ., et al. 2016, *ApJ*, 821, 82
- Osorio, M., Anglada, G., Carrasco-González, C., et al. 2014, *ApJ*, 791, L36
- Panić, O., Hogerheijde, M. R., Wilner, D., et al. 2008, *A&A*, 491, 219
- Pérez, L. M., Isella, A., Carpenter, J. M., & Chandler, C. J. 2014, *ApJ*, 783, L13
- Pérez, L. M., Chandler, C. J., Isella, A., et al. 2015, *The Astrophysical Journal*, 813, 41
- Pérez, L. M., Carpenter, J. M., Andrews, S. M., et al. 2016, arXiv:1610.05139
- Piétu, V., Guilloteau, S., & Dutrey, A. 2005, *A&A*, 443, 945
- Pinilla, P., Birnstiel, T., Ricci, L., et al. 2012, *A&A*, 538, A114
- Pinte, C., Dent, W. R. F., Ménard, F., et al. 2016, *ApJ*, 816, 25
- Pohl, A., Benisty, M., Pinilla, P., et al. 2017, *ApJ*, 850, 52
- Pollack, J. B., Hollenbach, D., Beckwith, S., et al. 1994, *ApJ*, 421, 615
- Quanz, S. P., Avenhaus, H., Buenzli, E., et al. 2013, *ApJ*, 766, L2
- Raman, A., Lisanti, M., Wilner, D. J., Qi, C., & Hogerheijde, M. 2006, *AJ*, 131, 2290
- Reggiani, M., Quanz, S. P., Meyer, M. R., et al. 2014, *ApJ*, 792, L23
- Richard, S., Barge, P., & Le Dizès, S. 2013, *A&A*, 559, A30

- Rodmann, J., Henning, T., Chandler, C. J., Mundy, L. G., & Wilner, D. J. 2006, A&A, 446, 211
- Ros, K., & Johansen, A. 2013, A&A, 552, A137
- Ruge, J. P., Flock, M., Wolf, S., et al. 2016, A&A, 590, A17
- Sandell, G., Weintraub, D. A., & Hamidouche, M. 2011, ApJ, 727, 26
- Semenov, D., Henning, T., Helling, C., et al. 2003, A&A, 410, 611
- Shakura, N. I., & Sunyaev, R. A. 1973, A&A, 500, 33
- Sierra, A., Lizano, S., & Barge, P. 2017, ApJ, 850, 115
- Sierra, A., Lizano, S., Macías, E., et al. 2019, ApJ, 876, 7.
- Surville, C., & Barge, P. 2015, A&A, 579, A100
- Surville, C., Mayer, L., & Lin, D. N. C. 2016, ApJ, 831, 82
- Takeuchi, T., & Lin, D. N. C. 2002, ApJ, 581, 1344
- Taki, T., Fujimoto, M., & Ida, S. 2016, A&A, 591, A86
- Tapia, C., Lizano, S., Sierra, A., et al. 2019, arXiv e-prints, arXiv:1911.05108
- Testi, L., Natta, A., Shepherd, D. S., & Wilner, D. J. 2003, A&A, 403, 323
- Testi, L., Birnstiel, T., Ricci, L., et al. 2014, Protostars and Planets VI, 339
- The, P. S., de Winter, D., & Perez, M. R. 1994, A&AS, 104, 315
- Thi, W.-F., Mathews, G., Ménard, F., et al. 2010, A&A, 518, L125
- Toomre, A. 1964, ApJ, 139, 1217
- Ubach, C., Maddison, S. T., Wright, C. M., et al. 2017, MNRAS, 466, 4083
- van der Marel, N., van Dishoeck, E. F., Bruderer, S., et al. 2013, Science, 340, 1199
- van der Marel, N., Dong, R., di Francesco, J., et al. 2019, ApJ, 872, 112
- Varnière, P., & Tagger, M. 2006, A&A, 446, L13
- Voshchinnikov, N. V., Il'in, V. B., & Henning, T. 2005, A&A, 429, 371
- Yang, H., & Li, Z.-Y. 2019, arXiv e-prints, arXiv:1909.08192
- Yen, H.-W., Liu, H. B., Gu, P.-G., et al. 2016, ApJ, 820, L25
- Youdin, A. N., & Lithwick, Y. 2007, Icarus, 192, 588
- Wada, K., Tanaka, H., Suyama, T., et al. 2007, ApJ, 661, 320

- Wada, K., Tanaka, H., Suyama, T., et al. 2008, ApJ, 677, 1296
- Wagner, K., Apai, D., Kasper, M., et al. 2015, ApJ, 813, L2
- Weidenschilling, S. J. 1977, MNRAS, 180, 57
- Whipple, F. L. 1972, From Plasma to Planet, 211
- Williams, J. P., & Cieza, L. A. 2011, Annual Review of Astronomy and Astrophysics, 49, 67
- Wilner, D. J., D'Alessio, P., Calvet, N., Claussen, M. J., & Hartmann, L. 2005, ApJ, 626, L109
- Windmark, F., Birnstiel, T., Güttler, C., et al. 2012, A&A, 540, A73
- Wyatt, M. C. 2008, ARA&A, 46, 339
- Zhang, K., Blake, G., & Bergin, E. 2015, IAU General Assembly 29, 2256118
- Zhu, Z., Zhang, S., Jiang, Y.-F., et al. 2019, arXiv e-prints , arXiv:1904.02127.